

國立交通大學

應用化學所

博士論文

有機-無機黏土與量子點奈米複合材料
物理性質之研究

**The Study of Organic-Inorganic Clay and Quantum
Dots Nanocomposites on Physical Properties**

研究生：傅懷廣

指導教授：張豐志 教授

中華民國九十八年二月

有機-無機黏土與量子點奈米複合材料物理性質之研究

The Study of Organic-Inorganic Clay and Quantum Dots nanocomposites on Physical
Properties

研究生：傅懷廣

Student : Huai-Kuang Fu

指導教授：張豐志

Advisor : Feng-Chih Chang

國立交通大學

應用化學所

博士論文



Submitted to Department of Applied of chemistry
College of Science

National Chiao Tung University

In Partial Fulfillment of the Requirements

For the Degree of

Doctor of Philosophy

In

Applied Chemistry

February 2009

Hsinchu, Taiwan, Republic of China

中華民國九十八年二月

誌謝

時光飛逝，轉眼間又要跟大家道別了，回想起這段求學生涯，學到好多知識與人生的經歷，也遇到很多幫助我的貴人，讓我可以順利完成博士學位。

首先，我要感謝張豐志老師不斷的給予我鼓勵與栽培，並提供良好的研究環境。讓我除了學到實驗上的技巧之外更能學習到自動自發與獨立研究的能力。老師對我的諄諄教誨及期望我會謹記在心。

感謝口試委員：邱顯堂教授、段葉芳教授、林宏洲教授、吳震裕教授與黃介銘教授在學生的論文上提供了寶貴的指導與意見，使得論文可以更加的豐富與完整。

感謝實驗室的學長郭紹偉博士、黃智峯博士給予我論文上的意見及幫助，感謝葉定儒學長傳授實驗上的技巧，讓我的研究可以更順利。也感謝凱琪學姐、春雄、弟弟、婉君、阿堅、倩婷、小朱、仁志、幸儀、宜弘在實驗上的幫忙與協助讓我順利完成論文。另外要感謝寶寶學姐與漢清學長，讓我的研究所生涯充滿歡笑與回憶。感謝每位實驗室成員，感謝你們維持實驗室的運作。另外，要特別感謝中興大學植病系貴儀中心 趙佩琪小姐，感謝你在 TEM 上的協助。感謝文君姐不斷給予鼓勵與意見，讓我獲益良多。感謝大老闆 Steven 與愛搞笑建亨在生活上的幫忙，讓我的生活更精彩。感謝我的好友仁陽、沛原、仲辰、柏惇、育鮮、雅雅、曼琳、冠仁、湘菱，因為你們的存在與幫助，讓我順利完成學業與豐富我精彩的生活。特別感謝 Barbie 這段時間的鼓勵，因為你，讓我的生活更充實。

最後，將此論文獻給我親愛的父母親、姐姐與奶奶，感謝父母親對我的栽培及家人的支持，讓我無後顧之憂的成長並順利完成學業。

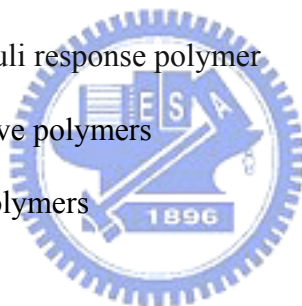
僅以這分論文，獻給在我求學的路上關心與照顧我的各位。

懷廣 2009 年 2 月


Outline of Contents

	Pages
Acknowledgments	
Outline of Contents	I
List of Tables	VI
List of Scheme	VII
List of Figures	VIII
Abstract (in Chinese)	XIII
Abstract (in English)	XVI
Chapter 1 Introduction of Organic-Inorganic Nanocomposites	1
1.1 Introduction polymer/clay nanocomposites	1
1.1.1 Structure of layered silicates	3
1.1.2 Organically modified clays	4
1.1.3 Preparation methods of nanocomposites	6
1.1.3.1 In situ polymerization of click chemistry	6
1.1.3.2 Living polymerization	8
1.1.4 Type of the nanocomposites	10
1.1.5 Properties of the nanocomposites	11
1.1.5.1 Thermal stability and flammability	11
1.1.5.2 Dimensional stability	12
1.1.5.3 Gas barrier properties	14
1.1.5.4 Mechanical propertie	15
1.1.5.4.1 Dynamic mechanical analysis (DMA)	15
1.1.5.4.2 Tensile properties	17

1.2 Introduction of QDs nanocomposites	19
1.2.1 Bulk semiconductor	21
1.2.2 Nanocrystalline semiconductors	23
1.2.3 Introduction of the II-VI ZnS material	26
1.2.4 Properties of nanostructure	28
1.2.4.1 Surface effect	29
1.2.4.2 Small size effect	29
1.2.4.3 Quantum size effect	30
1.2.4.4 Quantum confinement effect	31
1.2.5 Emission theory	32
1.2.5.1 Fluorescence and non-radiative transfer	34
1.3 Introduction of stimuli response polymer	35
1.3.1 Thermo-responsive polymers	36
1.3.2 PH responsive polymers	37
References	39

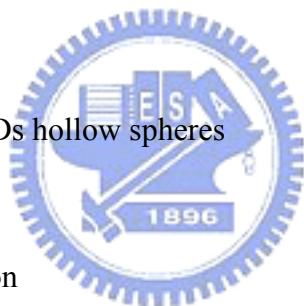


Chapter 2 Studies on Thermal Properties of PS Nanocomposites for the Effect of Intercalated Agent with Side Groups	63
Abstract	63
2.1 Introduction	64
2.2 Experimental	66
2.2.1 Materials	66
2.2.2 Preparation of POSS-Cl compound	66
2.2.3 Preparation of C ₂₀ -4VB intercalated agent	67
2.2.4 Preparation of C ₂₀ -POSS intercalated agent	67

2.2.5 Preparation of C ₂₀ -, C ₂₀ -4VB, and C ₂₀ -POSS modified clays	67
2.2.6 Preparation of polystyrene/clay nanocomposites	68
2.2.7 Instrumentations	68
2.3 Results and discussion	70
2.3.1. Characterizations of C ₂₀ -, C ₂₀ -4VB, and C ₂₀ -POSS modified clays	70
2.3.2. Characterizations of polystyrene/clay nanocomposites	70
2.3.3. Glass transition temperatures	71
2.3.4. Molecular weights of the nanocomposites	71
2.3.5 TGA analyses	71
2.3.6 Coefficient of thermal expansion	72
2.4 Conclusions	74
Acknowledgments	74
References	75
	
Chapter 3 Properties Enhancement of PS Nanocomposites through the POSS surfactants	89
Abstract	89
3.1 Introduction	90
3.2 Experimental	92
3.2.1 Materials	92
3.2.2 Preparation of C ₂₀ -POSS intercalated agent	92
3.2.3 Preparation of POSS-NH ₂ and C ₂₀ -POSS modified clays	93
3.2.4 Preparation of polystyrene/clay nanocomposites	94
3.2.5 Instrumentations	94

3.2.5.1 Measurement the molecular weights characterization	94
3.2.5.2 Structure analysis characterization	95
3.2.5.3 Thermal and mechanical analysis characterization	95
3.3 Results and discussion	97
3.3.1 Morphologies of modified clays and nanocomposites	97
3.3.2 Fourier transfer infrared analyses	98
3.3.3 Thermal properties	98
3.3.4 Molecular weights of the nanocomposites	99
3.3.5 Coefficient of thermal coefficient	100
3.4 Conclusions	101
Acknowledgments	101
References	102
Chapter 4 Effect of the organically modified Nanoclay on Low-Surface- Energy Materials of Polybenzoxazine	116
Abstract	116
4.1 Introduction	117
4.2 Experimental	118
4.2.1 Preparation of CPC-modified clays	118
4.2.2. Preparation of CPC/clay/PP-a nanocomposites by solvent method	118
4.2.3. Characterizations	118
4.2.4 Surface energy determination	119
4.3 Results and discussion	121
4.4 Conclusions	123

References	125
Chapter 5 Preparation of the Stimuli-Responsive ZnS/PNIPAM Hollow Spheres	132
Abstract	132
5.1 Introduction	133
5.2 Experimental	135
5.2.1 Materials	135
5.2.2 Preparation of the prepolymers of poly(ϵ -caprolactone)	135
5.2.3 Synthesis of the capping agent 2-mercaptoethyl methacrylate	136
5.2.4 Preparation of ZnS nanoparticle peripherally with methacrylate	136
5.2.5 Synthesis of QDs hollow spheres	136
5.3 Characterizations	138
5.4 Results and discussion	139
5.5 Conclusions	142
Acknowledgments	142
References	143
Chapter 7 Conclusions	155



List of Tables

	Pages
Table 1-1. Applications of the ZnS-based phosphors doping with different activators.	27
Table 2-1. Basal spacing and organic fraction of the OMMT.	78
Table 2-2. Results of thermal and mechanical properties of Polystyrene and Polystyrene Nanocomposites.	78
Table 2-3. Molecular weights of polystyrene and polystyrene Nanocomposites.	79
Table 3-1. Results of thermal and mechanical properties of polystyrene and polystyrene Nanocomposites.	104
Table 3-2. Molecular weights of polystyrene and polystyrene nanocomposites.	105
Table 4-1. Advancing contact angles, surface free energies, roughness, XPS analysis and thermal properties of polybenzoxazine/clay nanocomposites.	127

List of Schemes

	Pages
Scheme 2-1. Intercalation agents for organic modified clays preparation	80
Scheme 2-2. Synthesis of the POSS -Cl compound	81
Scheme 2-3. Synthesis of the C ₂₀ -4VB and C ₂₀ -POSS intercalated agents	81
Scheme 3-1. Chemical structures of the intercalated agents used to prepare the modified clays	106
Scheme 3-2. Synthesis of the POSS -Cl compound	107
Scheme 3-3. Synthesis of the C ₂₀ -POSS intercalated agent	108
Scheme 4-1. Representation of the intercalated agent was inserted into the silicate layers via ion exchange and preparation of polybenzoxazine nanocomposites by thermal treatment	128
Scheme 5-1. Synthesis of the capping agent of 2-mercaptoethyl methacrylate	146
Scheme 5-2. Representation of the photoluminescence hollow sphere preparation and temperature responsive.	147

List of Figures

	Pages
Figure 1-1. Structure of 2:1 layered silicates	46
Figure 1-2. Scheme of effect of cationic exchange on interlayer spacing	46
Figure 1-3. Chemical structures of the surfactants used to prepare the modified clays	47
Figure 1-4. (a) Chemical structure of organic clay 10A, in which HT is hydrogenated tallow with ~65% C18, ~30% C16, and ~5% C14. (b) Chemical structure of organic clay VB16	47
Figure 1-5. Schematic representation of various methods used to prepare polymer-layered-silicate nanocomposites.	48
Figure 1-6. Preparation of polytetrahydrofuran/montmorillonite clay nanocomposites by in situ cationic ring opening polymerization.	48
Figure 1-7. (a) Azide-functionalized montmorillonite clay and its “Click” reactions with propargyl methacrylate and (b) Alkyne-Functionalized polytetrahydrofuran.	49
Figure 1-8. The synthesis of the photoiniferter progress.	49
Figure 1-9. The concept of in situ living polymerization from the silicate anchored photoiniferter.	50
Figure 1-10. The preparation of block copolymers by sequential addition of monomers.	50
Figure 1-11. Schematically illustration of three different types of thermodynamically achievable polymer/layered silicate nanocomposites.	51

Figure 1-12. TGA curves for polystyrene, PS, and the nanocomposites.	51
Figure 1-13. Peak heat release rates for polystyrene and the three nanocomposites.	52
Figure 1-14. PS and PS/clay nanocomposites after dimension stability test. Clay loading is 5 wt % for all nanocomposites.	52
Figure 1-15. Formation of tortuous path in PLS nanocomposites.	53
Figure 1-16. Relative gas permeability versus clay loading for polymer/clay nanocomposites per the model be Nielsen. The different curves represent aspect ratios of 50, 100, 150, and 200 for series 1–4 respectively.	53
Figure 1-17. Storage modulus of (a) pure PS, (b) PS/MMT-1, (c) PS/MMT-2 and (d) PS/MMT-3.	54
Figure 1-18. $\tan\delta$ values of (a) pure PS, (b) PS/MMT-1, (c) PS/MMT-2 and (d) PS/MMT-3.	54
Figure 1-19. (a) Tensile strengths, (b) Young's modulus and (c) elongations at break of PS/MMT nanocomposites.	55
Figure 1-20. Schematic illustration of formation of hydrogen bonds in N6/MMT nanocomposite.	56
Figure 1-21. Effect of clay content on tensile modulus in case of N6/OMLS nanocomposites prepared via melt extrusion.	56
Figure 1-22. Schematic illustration of the density of states in metal and semiconductor clusters.	57
Figure 1-23. Idealized density of states for one band of a semiconductor structure of 3, 2, 1, and "0" dimensions.	57
Figure 1-24. Structures of the ZnS crystals (a) cubic phase and (b) hexagonal	58

phase.	
Figure 1-25. Quantum confinement effect of the electrons and the photons.	59
Figure 1-26. Configuration coordiance diagrams of the phosphor.	59
Figure 1-27. Energy transformation diagram of the excitation energy.	60
Figure 1-28. Progress of the relaxation.	60
Figure 1-29. Diagram of the Stokes shift.	61
Figure 1-30. Influence of the different coupling effect on width of the emission peaks.	61
Figure 1-31. Potential stimuli and responses of synthetic polymers.	62
Figure 1-32. Schematic of ‘smart’ polymer response with temperature.	62
Figure 1-33. Control of micellar states dependent on pH.	62
Figure 2-1. X-Ray diffraction patterns of pure clay, and intercalated clays.	82
Figure 2-2. XRD spectra of the three surfactant-containing nanocomposites indicating the extent of delamination.	83
Figure 2-3. TEM images of (a) C ₂₀ , (b) C ₂₀ -4VB, (c) C ₂₀ -POSS (low magnification), and (d) C ₂₀ -POSS (high magnification)-treated nanocomposites.	84
Figure 2-4. DSC curves glass transition temperature of (a) PS, (b) the nanocomposites formed used C ₂₀ , (c) the nanocomposites formed used C ₂₀ -4VB, and (d) the nanocomposites formed used C ₂₀ -POSS.	85
Figure 2-5. TGA curves of (a) Pure Clay, (b) C ₂₀ -POSS/Clay, (c) C ₂₀ -4VB/Clay, and (d) C ₂₀ /Clay.	86
Figure 2-6. (A)TGA and (B) DTG curves of the nanocomposites under a nitrogen atmosphere: (a) pure PS, (b) the nanocomposite formed	87

with C₂₀, (c) the nanocomposite formed with C₂₀-4VB, and (d) the nanocomposite formed with C₂₀-POSS.

Figure 2-7. Coefficient of thermal expansion of (a) pure PS, (b) the nanocomposite formed with C ₂₀ , (c) the nanocomposite formed with C ₂₀ -4VB, and (d) the nanocomposite formed with C ₂₀ -POSS.	88
Figure 3-1. X-Ray diffraction patterns of pure clay, and intercalated clay.	109
Figure 3-2. XRD spectra of C ₂₀ -POSS, pure clay, and C ₂₀ -POSS/Clay.	110
Figure 3-3. XRD spectra of the two surfactant-containing nanocomposites indicating the extent of delamination.	111
Figure 3-4. TEM images of (a) POSS-NH ₂ and (b) C ₂₀ -POSS-treated nanocomposites.	112
Figure 3-5. IR spectra of the two intercalated agent, intercalated clay, and pure clay.	113
Figure 3-6. DSC curves glass transition temperature of (a) PS, (b) the nanocomposites formed used POSS-NH ₂ , and (c) the nanocomposites formed used C ₂₀ -POSS.	114
Figure 3-7. TGA curves of (a) pure Clay, (b) POSS-NH ₂ /Clay, (c) C ₂₀ -POSS/Clay, (d) pure PS, (e) the nanocomposite formed with POSS-NH ₂ , and (f) the nanocomposite formed with C ₂₀ -POSS.	115
Figure 4-1. X-ray diffraction patterns of (a) pure clay, and (b) CPC/clay, (c) PP-a/Clay 3 wt%, (d) 5 wt%, (e) 10 wt%.	129
Figure 4-2. TEM micrographs of the polybenzoxazines (PP-a) nanocomposites containing 3 wt % clay: (left) low magnification, and (right) high magnification.	130
Figure 4-3. AFM images of CPC/ Clay 10% /PP-a: (a) Topography image,	131

and (b) Phase image.

Figure 5-1. The ^1H NMR spectrum for 2-mercaptoethyl methacrylate. 148

Figure 5-2. FT-IR spectra of the (a) PCL, (b) ZnS/PCL/PNIPAM spheres, and 149
(c) ZnS/PNIPAM hollow spheres.

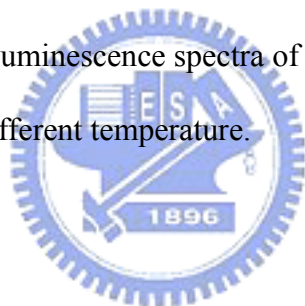
Figure 5-3. X-ray diffraction patterns of the (a) ZnS nanoparticle and (b) 150
ZnS/PNIPAM hollow spheres.

Figure 5-4. TEM image and electron diffraction pattern of the (a) PNIPAM 151
hollow spheres, (b) ZnS/PNIPAM hollow spheres.

Figure 5-5. Variation of average hydrodynamic diameters (D_h) vs. 152
temperature of the ZnS/PNIPAM hollow spheres.

Figure 5-6. PLE and PL spectrum of the 0.3-ZnS and 0.6-ZnS nanoparticles. 153

Figure 5-7. Normalized photoluminescence spectra of the 0.3-ZnS/PNIPAM 154
hollow sphere at different temperature.



有機-無機黏土與量子點奈米複合材料物理性質之研究

學生：傅懷廣

指導教授：張豐志

國立交通大學應用化學研究所 博士班

摘 要



高分子複合材料一般為有機高分子基材與無機添加物的結合且至少存在於一維的奈米尺寸的範圍下。添加物從結構上可以分為一維(例如:奈米碳管與纖維)，二維(片狀的無機材料，如黏土)，與三維(球與量子點)。導入奈米尺寸添加物高分子上，改善了高分子原本的物理性質。在本篇論文可以分成四個部分，探討無機的添加物對於高分子複合材料物理性質的影響。

1. 插層劑側鏈的官能基對於聚苯乙烯/黏土奈米複合材料影響

我們利用三種不同插層劑改質的有機黏土藉由乳化聚合製備聚苯乙烯/黏土奈米複合材料。這些奈米複合材料在黏土含量在 3 wt % 時皆達到脫層的結構。我們所使用的插層劑(C₂₀、C₂₀-4VB、與 C₂₀-POSS)經由離子交換反應後成功進入黏土的層間，使親水黏土與疏水高分子有更好的相容性，進一步的讓改質後的有機黏土均勻分散於高分子基材中並達到脫層的結構。從 X-ray

繞射儀 (XRD)、穿透式電子顯微鏡 (TEM) 與傅立葉紅外線光譜儀 (FT-IR) 的結果指出所使用的插層劑有成功的進入到黏土的層間，並成功製備具有脫層結構的聚苯乙烯/黏土奈米複合材料。在熱性質的測試中 (TGA 與 TMA)，C₂₀-POSS/黏土聚苯乙烯奈米複合材料相對於聚苯乙烯下開始產生裂解的溫度可以提升 25 °C 其熱膨脹係數 (CTE) 最大的降低的量可以達到 40 %。另外，這些經由改質奈米複合材料的玻璃轉化溫度(T_g)都高於聚苯乙烯。

2. 經由 POSS 的插層劑改質使聚苯乙烯奈米複合材料性質提升

我們使用 POSS-NH₂ 與 C₂₀-POSS 為插層劑改質黏土並進一步製備 POSS/黏土聚苯乙烯奈米複合材料。X-ray 繞射儀 (XRD) 的結果指出本研究所使用的插層劑製備的 POSS/黏土奈米複合材料在 X-ray 的圖譜上都沒有繞射峰出現，此結果表示我們所製備的奈米複合材料皆達到脫層的結構。並進一步從穿透式電子顯微鏡 (TEM) 直接觀察複合材料的結構型態，從結果指出黏土均勻分散於聚苯乙烯高分子基材中並達到脫層的結構。對於 C₂₀-POSS/黏土奈米複合材料我們導入這些脫層的黏土於聚苯乙烯中可以有效的提升其玻璃轉化溫度(T_g)、熱裂解溫度 (T_d) 與熱膨脹係數 (CTE) 最大的降低的量可以達到 40 %。

3. 有機奈米黏土在聚氧代氮代苯并環己烷於低表面能材料的影響

我們製備新穎低表面能聚氧代氮代苯并環己烷/有機黏土改質奈米複合材料。我們使用三種液體的方法計算表面能。CPC/黏土 10%/PP-a 奈米複合

材料經過 200 °C/4 小時交聯後反應後具有極低的表面能係數 12.7 mJ/m²，甚至低於我們所熟悉的鐵氟龍材料(22.0 mJ/m²)。我們使用 X-ray 光電子光譜 (XPS)表示我們所製備的奈米複合材料的表面具有較高的矽含量，表示有機黏土在製備的過程中優先的存在於最外層的表面。另外，CPC/黏土 10%/PP-a 奈米複合材料的玻璃轉化溫度(T_g)較 PP-a 高 22.6 °C 與熱裂解溫度 (T_d)也相對於 PP-a 提升 31.5 °C。我們發現這個方法可以製備同時具有低表面能與高熱穩定性的高分子黏土奈米複合材料。

4. 製備具有刺激-應答硫化鋅/聚異丙基丙烯醯氨中空球

新穎的量子點硫化鋅/聚異丙基丙烯醯氨混成中空球是使用局部自由基聚合反應製備，在 PCL 奈米球周圍讓異丙基丙烯醯氨與交聯劑 (MBA) 反應所形成，後進一步的使用酵素 (Lipase PS) 將 PCL 進行生物分解。我們使用穿透式電子顯微鏡 (TEM)與動態光散射儀 (DLS) 分別有系統的探討所形成的硫化鋅/聚異丙基丙烯醯氨中空球結構與熱敏感可逆的性質。硫化鋅/聚異丙基丙烯醯氨中空球具有螢光的性質並在大約 32 °C 有膨脹收縮的特性，符合於螢光光譜上有些微紅位移的現象出現。

The Study of Organic-Inorganic Clay and Quantum Dots nanocomposites on Physical Properties


Student : Huai-Kuang Fu

Advisors : Dr. Feng-Chih Chang

Institute of Applied Chemistry

National Chiao Tung University

ABSTRACT



Polymer nanocomposites are commonly defined as the combination of a polymer matrix and additives that have at least one dimension in nanometer range. The additives can be one-dimensional (example include nanotubes and fibers), two-dimensional (which include layered minerals like clay), or three-dimensional (include spherical particles and quantum dots). Nanoscale-filled polymeric systems offer the prospect of greatly improving many of the properties of the polymer matrix. The dissertation was focused on four major subjects: the study of the inorganic additives of polymer nanocomposites on physical properties.

1. Studies on Thermal Properties of PS Nanocomposites for the Effect of Intercalated Agent with Side Groups

Polystyrene layered silicate nanocomposites were prepared from three new

organically modified clays by emulsion polymerization method. These nanocomposites were exfoliated up to 3 wt % content of pristine clay relative to the amount of polystyrene (PS). The intercalated agents, C₂₀, C₂₀-4VB, and C₂₀-POSS intercalated into the galleries result in improved compatibility between hydrophobic polymer and hydrophilic clay and facilitate the well dispersion of exfoliated clay in the polymer matrix. Results from X-ray diffraction, TEM and Fourier transform infrared spectroscopy indicate that these intercalated agents are indeed intercalated into the clay galleries successfully and these clay platelets are exfoliated in resultant nanocomposites. Thermal analyses of polystyrene-layered silicate nanocomposites compared with virgin PS indicate that the onset degradation temperature ca. 25 °C increased and the maximum reduction in coefficient of thermal expansion (CTE) is ca. 40 % for the C₂₀-POSS/clay nanocomposite. In addition, the glass transition temperatures of all these nanocomposites are higher than the virgin PS.

2. Properties Enhancement of PS Nanocomposites through the POSS surfactants

The polyhedral oligomeric silsesquioxane (POSS)-clay hybrids of polystyrene are prepared by two organically modified clays using POSS-NH₂ and C₂₀-POSS as intercalated agents. X-ray diffraction (XRD) studies show that the formation of these POSS/clay/PS nanocomposites in all cases with the disappearance of the peaks corresponding to the basal spacing of MMT. Transmission electronic spectroscopy

(TEM) was used to investigate the morphology of these nanocomposites and indicates that these nanocomposites are comprised of a random dispersion of exfoliated throughout the PS matrix. Incorporation of these exfoliated clay platelets into the PS matrix led to effectively increase in glass transition temperature (T_g), thermal decomposition temperature (T_d) and the maximum reduction in coefficient of thermal expansion (CTE) is ca. 40 % for the C₂₀-POSS/clay nanocomposite.

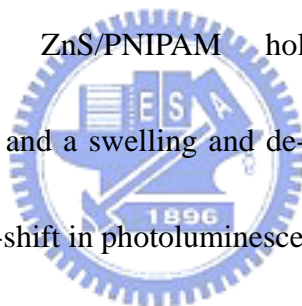
3. Effect of the organically modified Nanoclay on Low-Surface-Energy Materials of Polybenzoxazine

Novel low surface free energy materials of polybenzoxazine/organically modified silicate nanocomposites have been prepared and characterized. The CPC (cetylpyridinium chloride)/clay10%/Poly(3-phenyl-3,4-dihydro-2H-1,3-benzoxazine) (PP-a) possesses an extremely low surface free energy (12.7 mJ/m²) after 4 hrs curing at 200 °C, even lower than that of poly(tetrafluoroethylene) (22.0 mJ/m²) calculated on the basis of the three-liquid geometric method. X-ray photoelectron spectroscopy (XPS) shows higher silicon content on the surface of nanocomposites than average composition, implying that the clay is more preferentially enriched on the outermost layer. In addition, the glass transition temperature (T_g) of the polybenzoxazine (PP-a) in the nanocomposite is 22.6 °C higher and its thermal decomposition temperature is also higher than the pure PP-a. This finding provides a

simple way to prepare lower surface energy and high thermal stability material.

4. Preparation of the Stimuli-Responsive ZnS/PNIPAM Hollow Spheres

Novel quantum dots ZnS/poly(N-isopropylacrylamide) (PNIPAM) hybrid hollow spheres were obtained by localizing free radical polymerization of NIPAM and crosslinker (MBA) at the peripheral of PCL nanoparticles, followed by biodegradation of PCL with an enzyme of the Lipase PS. The formation of ZnS/PNIPAM hollow spherical structures and the thermo-sensitive reversible properties were systematically investigated by transmission electron microscopy (TEM) and dynamic light scattering (DLS), respectively. The ZnS/PNIPAM hollow spheres possess the photoluminescence properties and a swelling and de-swelling at about 32 °C, which agrees well with the slight red-shift in photoluminescence spectra.



Chapter 1

Introduction of the Organic- Inorganic Nanocomposites

Polymer nanocomposites are commonly defined as the combination of a polymer matrix and additives that have at least one dimension in the nanometer range. The additives can be one-dimensional (example include carbon nanotubes and fibres), two-dimensional (which include layered minerals like clay), or three-dimensional (including spherical particles).



1.1 Introduction of polymer/clay nanocomposites

Over the past decade, polymer nanocomposites have attached considerable interests in both academia and industry, owing to their outstanding mechanical properties like elastic stiffness and strength with only a small amount of nanoadditives. The utility of inorganic nanoparticles as additives to enhance polymer performance has been established and now provides additional opportunities for many diverse commercial applications. Low-volume additions (1-10%) of isotropic nanoparticles, such as titania, alumina, and silver, and anisotropic nanoparticles, such as layered silicates (nanoclays) or carbon nanotubes, provide property enhancements with respect to the neat resin that are comparable to that achieved by conventional loadings

(15-40%) of traditional micrometer-scale inorganic fillers. The lower loadings facilitate processing and reduce component weight. Most important though is the unique value-added properties and property combinations that are not normally possible with traditional fillers, such as reduced permeability, optical clarity, self-passivation, and flammability, oxidation, and ablation resistance.

The synthesis and development of polymer/clay nanocomposites have attracted a tremendous amount of interest during the last decade, because these materials exhibit improved properties which are synergistically derived from the two components because of their nanometer-size dispersion, [1–5] as compared to those of the pristine polymer. These improvements include enhanced barrier characteristics, [6] increased (storage and loss) moduli and strengths, [7] high heat distortion temperatures, [8] decreased thermal expansion coefficients, [6 – 9] reduced permeability to gases and liquids, [10] and enhanced ionic conductivity. [11] In the early 1990s, Toyota Central Research Laboratories in Japan reported work on a Nylon-6 nanocomposite, [12] for which a very small amount of nano filler loading resulted in a pronounced improvement of thermal and mechanical properties. We have at our fingertips, however, the ability to change the size, shape, volume fraction, interface, and degree of dispersion or aggregation. Thus, the opportunities may well become limitless when theory and experiment have assembled enough information to guide further

development.

1.1.1 Structure of layered silicates

The commonly clays used for the preparation of polymer/layered silicate nanocomposites belong to the same general family of phyllosilicates. Their crystal structure consists of layers made up of two silica tetrahedral fused to an edge shared octahedral sheet of either aluminum or magnesium hydroxide. The layer thickness is ~1 nm and the lateral dimensions of these layers may vary from 30 nm to several micrometres and even larger depending on the particular layered silicate. Stacking of the layers leads to a regular van der Waals gap between the layers called the interlayer or gallery. Isomorphic substitution within the layers (for example, Al^{+3} replaced by Mg^{+2} or by Fe^{+3} , or Mg^{+2} replaced by Li^{+1}) generates negative charges that are counterbalanced by alkali and alkaline earth cations situated inside the galleries. Details regarding the structure and chemistry for these layered silicates are provided in Figure 1-1.

Montmorillonite is hydrophilic in nature, which hinders the homogeneous dispersion in the organic polymer phase. Ion exchange of the interlayer inorganic cations (Na^+ , Ca^{2+}) with organic cation renders the hydrophilic clay surface organophilic. The reduction in surface energy improves the wetting characteristics of the clay surface

with polymers or monomers. [13,14]

1.1.2 Organically modified clays

To improve compatibility with other polymer matrixes, one must convert the normally hydrophilic silicate surface to organophilic, which makes possible intercalation of many engineering polymers. The ammonium cation may have hydrocarbon tails and other groups attached and is referred to as a “surfactant” owing to its amphiphilic nature. The extent of the negative charge of the clay is characterized by the cation exchange capacity, i.e., CEC. Generally, this can be carried out by ion exchange reactions with cationic surfactants including primary, secondary, tertiary and quaternary alkyl ammonium or alkylphosphonium cations, which increase the original clay interlayer spacing and behave as organophilic surfactants (Figure 1-2). The role of alkylammonium or alkylphosphonium cations in the organosilicates is to lower the surface energy of the inorganic host and improve the wetting characteristics with the polymer matrix, and results in a larger interlayer spacing.

Chang and co-workers [15] reported the preparation of two types of nanocomposites formed from cetylpyridinium chloride (CPC)- and aminopropylisobutyl polyhedral oligomeric silsesquioxane (POSS)-treated clays

(Figure 1-3). The PS/clay nanocomposite formed using the CPC-treated clay exhibited no significant improvement in thermal properties. [16-20] The major advantage of choosing POSS molecules is its thermal stability up to 300 °C, higher than the thermal degradation temperatures of most organic molecules. POSS consists of a rigid cubic silica core with 0.53 nm side length, to which organic functional groups can be attached at the vertices for further reactions. POSS derivatives containing amine functional groups can play the role of surfactants for the treatment of clay and the thermal stability of the resulting nanocomposite is enhanced.

Wang [21] used two different organic modifications of the montmorillonite, one contains a styryl monomer on the ammonium ion while the other contains no double bond. A double bond that may be involved in the polymerization reaction is present in the cation of the clay. Polystyrene-clay nanocomposite has been prepared by bulk, solution, suspension, and emulsion polymerization as well as by melt blending. The organic modification as well as the mode of preparation may determine whether the composite is either exfoliated or intercalated. Exfoliation is more likely to occur if the ammonium ion contains a double bond which can participate in the polymerization reaction. However, the mere presence of this double bond is not sufficient to always produce an exfoliated system. This work focused on two organically modified clays, one of which is labeled as VB16, where the ammonium salt contains one long chain,

two methyl groups, and a styryl unit, while the other is labeled 10A, where the ammonium cation contains a long chain, two methyl groups, and a benzyl group. The structures of the ammonium salts used to prepare the clays are shown in Figure 1-4.

1.1.3 Preparation methods of nanocomposites

Polymerization of vinyl monomers intercalating into the montmorillonite (MMT) clay [22] were first reported in literature as early as 1961. The most recent methods to prepare polymer-layered-silicate nanocomposites have primarily been developed by several other groups. In general these methods (shown in Figure 1-5) are able to achieve molecular-level incorporation of the layered silicate (e.g. montmorillonite clay or synthetic layered silicate) in the polymer matrix by addition of a modified silicate either to a polymerization reaction (in situ method), [23-25] to a solvent-swollen polymer (solution blending), [26] or to a polymer melt (melt blending). [27-28] Recently, a method has been developed to prepare the layered silicate by polymerizing silicate precursors in the presence of a polymer. [29]

1.1.3.1 In situ polymerization of click chemistry

Yagci and co-worker report two effective routes for the synthesis of PTHF/clay nanocomposites, namely, (1) in situ cationic ring opening polymerization (CROP) and

(2) a method involving “click” chemistry. In the first approach, the nanocomposites have been prepared by the CROP of THF that is initiated in the intercalated layers of the clay. In the second approach, CROP of THF has been performed to produce alkyne-functionalized PTHF and the obtained polymers were subsequently anchored to azide-modified clay layers by a “click” reaction. In principle, this approach can be extended to the combination of azide-modified clay with any other alkyne containing polymers.

For the preparation of PTHF/clay nanocomposites by the in situ polymerization method, the hydroxyl functions of the modified intercalated montmorillonite clay (MMT-(CH₂CH₂-OH)₂) are reacted with trifluoromethanesulfonic anhydride (TfO₂), in the presence of 2,6-di-*tert*-butylpyridine (DTBP) as proton trap and dichloromethane as solvent, to produce the corresponding triflate ester that is known to be an initiator for the CROP of THF. Then, a large amount of THF monomer is added. [31] After the prescribed reaction time, the process directly leads to the formation of the PTHF/clay nanocomposites, as shown in Figure 1-6.

Figure 1-7 indicated the introduction of azide functionalities on the surface of the silica nanolayers, methanesulfonyl chloride was used to convert the hydroxyl groups into methanesulfonate groups, which were subsequently reacted with sodium azide to yield the desired clay “click” component. Alkyne-functionalized PTHF, the other

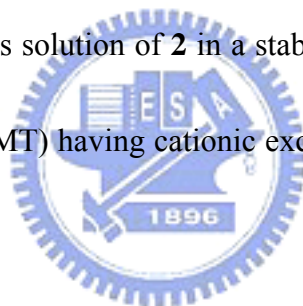
“click” component, was prepared by terminating living PTHF chains with propargyl alcohol (Figure 1-7), based on earlier developed synthetic routes for other end-functionalized PTHF systems. [33]

1.1.3.2 Living polymerization

Sogah and co-worker report our preliminary results on the preparation of exfoliated polymer/silicate nanocomposites by in situ polymerization from a silicate-anchored photoiniferter. The method worked reproducibly and is capable of producing nanocomposites of a broad range of silicate loading and polymer molecular weights. Taking advantage of the living characteristic of the process, we also prepared block copolymer/silicate nanocomposites by sequential monomer addition. One principal finding is that exfoliated nanocomposites with very high silicate contents (above 20 wt %) could readily be prepared. This is significant since it will allow the high silicate containing nanocomposites to be used as masterbatches in preparing all kinds of nanocomposites by simple blending without always having to begin from scratch.

The desired photoiniferter must contain a photoactive initiating moiety (in this case, the benzyl dithiocarbamate) capable of effecting living/controlled free radical polymerization of a variety of monomers. For an anchoring site, we chose the

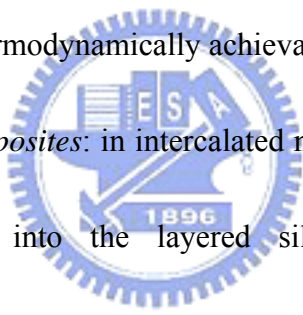
benzyltrimethylammonium moiety because it cannot undergo β -H Hoffman elimination at elevated temperatures unlike most of the current surfactants used in modifying clays. Figure 1-8 shows the synthesis of the photoiniferter from 4-(bromomethyl) benzyltrimethylammonium bromide (**1**). The displacement of the bromide by sodium *N,N*-diethyldithiocarbamate occurred in a straightforward manner to give the desired photoiniferter **2** in almost quantitative (98%) yield. The reaction was so clean that the only purification necessary was washing the precipitate with acetone and drying. The incorporation of **2** into the silicate was achieved by simply mixing and stirring an aqueous solution of **2** in a stable dispersion of a commercially available montmorillonite (MMT) having cationic exchange capacity of 92.6 mequiv/100 g (Figure 1-9). [34-35]



An important advantage offered by the living polymerizations is the capability to prepare nanocomposites containing block copolymers by sequential addition of monomers (Figure 1-10). In the first trial, PS/silicate nanocomposite containing living PS chain ends was employed to initiate living free radical polymerization of MMA to give Sil-PS-*b*-PMMA. In a similar manner, PMMA/silicate nanocomposite was employed to initiate living free radical polymerization of styrene to obtain Sil-PMMA-*b*-PS.

1.1.4 Type of the nanocomposites

In general, layered silicates have layer thickness on the order of 1 nm and very high aspect ratio (e.g. 10~1000). A few weight percent of layered silicates that are properly dispersed throughout the polymer matrix thus create much higher surface area for polymer/filler interaction as compared to conventional composites. Depending on the strength of interfacial interactions between the polymer matrix and layered silicate (modified or not), three different types of polymer/layered silicate (PLS) nanocomposites are thermodynamically achievable, as shown in Figure 1-11.

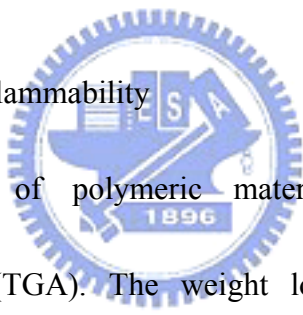
- 
- a. *Intercalated nanocomposites*: in intercalated nanocomposites, the insertion of a polymer matrix into the layered silicate structure occurs in a crystallographically regular fashion, regardless of the clay to polymer ratio. Intercalated nanocomposites are normally interlayer by a few molecular layers of polymer. Properties of the composites typically resemble those of ceramic materials.

- b. *Flocculated nanocomposites*: conceptually this is same as intercalated nanocomposites. However, silicate layers are some times flocculated due to hydroxylated edge-edge interaction of the silicate layers.

c. *Exfoliated nanocomposites*: in an exfoliated nanocomposite, the individual clay layers are separated in a continuous polymer matrix by an average distances that depends on clay loading. Usually, the clay content of an exfoliated nanocomposite is much lower than that of an intercalated nanocomposite.

1.1.5 Properties of nanocomposites

1.1.5.1 Thermal stability and flammability



The thermal stability of polymeric materials is usually studied by thermogravimetric analysis (TGA). The weight loss due to the formation of volatile products after degradation at high temperature is monitored as a function of temperature. When the heating occurs under an inert gas flow, a non-oxidative degradation occurs, while the use of air or oxygen allows oxidative degradation of the samples. Generally, the incorporation of clay into the polymer matrix was found to enhance thermal stability by acting as a superior insulator and mass transport barrier to the volatile products generated during decomposition.

Jin and co-worker investigated thermal property of polymer-clay nanocomposites by TGA and cone calorimetry. [37] The thermal stability of the nanocomposite is enhanced

relative to that of virgin polystyrene and this is shown in Figure 1-12. Typically, the onset temperature of the degradation is about 50 °C higher for the nanocomposites than for virgin polystyrene.

Recently clay nanocomposites were found to impart a substantial level of flame retardancy. The flame retardancy effect appears to originate from the clay's ability to contribute to char formation. This char layer forms an insulative layer to slow down heat transfer and retards movement of gases to feed the flame. One invariably finds that nanocomposites have a much lower peak heat release rate (PHRR) than the virgin polymer. The peak heat release rate for polystyrene and the three nanocomposites are also shown graphically in Figure 1-13. P16-3 means that the nanocomposite was formed using 3 % of P16 clay with polystyrene. The peak heat release rate falls as the amount of clay was increased. The suggested mechanism by which clay nanocomposites function involves the formation of a char that serves as a barrier to both mass and energy transport.

[38] It is reasonable that as the fraction of clay increases, the amount of char that can be formed increases and the rate at which heat is released is decreased. There has been a suggestion that an intercalated material is more effective than is an exfoliated material in fire retardancy. [37]

1.1.5.2. Dimensional stability

Dimensional stability is critical in many applications. For example, if the layers of a microelectronic chip have different thermal or environmental dimensional stabilities, then residual stresses can develop and cause premature failure. Poor dimensional stability can also cause warping or other changes in shape that affect the function of a material. Nanocomposites provide methods for improving both thermal and environmental dimensional stability. The possible mechanism by which nanofillers can affect the coefficient of thermal expansion (CTE) of a polymer has also been observed in traditional fillers.

The dimension stability of nanocomposites was studied by Zeng and Lee. [39] Figure 1-14 shows the shape changes of injection molded PS and PS/clay nanocomposites under the aforementioned thermal cycle (50 °C, 1 h; 75 °C, 1 h; 105 °C, 1 h; and 135 °C, 1h). The original sample shape is shown in the first row. Pure PS and the extruded PS/20A (dimethyl dehydrogenated tallow ammonium montmorillonite, 20A) nanocomposite are shown in the second row for comparison. The third row shows the in-situ polymerized pure PS, PS/20A, and PS/MHABS (2-methacryloyloxyethylhexadecyldimethylammonium bromide, MHABS) nanocomposites. All the nanocomposites contain 5 wt % of clay. In the absence of clay, the sample shrank greatly, and the shape became highly irregular. Dimension stability at elevated temperature was improved significantly when 5 wt % of clay was present in the

in-situ polymerized nanocomposites, as shown in the third row. The exfoliate PS/MHABS exhibited the best dimensional stability. After the heating cycle, although the sample shrank to a certain extent, the original shape and surface smoothness remained. It is noteworthy that the PS/20A nanocomposite prepared by extrusion compounding did not show much improvement in dimension stability at elevated temperature, as compared to the in-situ polymerized PS/20A nanocomposite with the same clay content.

1.1.5.3 Gas barrier properties

In many applications the gas barrier properties of polymers is critical. This is especially true in the food packaging industry. In many food packages the oxygen ingress determines the shelf life of the food in the package. For carbonated drinks the egress of carbon dioxide is the issue. It was recognized early in nanocomposite development that the high aspect ratios of clays could impart barrier to the composite. Clays are believed to increase the barrier properties by creating a maze or “tortuous path” (Figure 1-15) that retards the progress of the gas molecules through the matrix resin.

Nielsen [40] proposed a very simple model for the effect of platy materials on relative barrier performance. This model is commonly referred to as the tortuous path model. Figure 1-16 exhibits the effect of aspect ratio and clay loading on

relative gas permeability of a composite utilizing this model. It can be seen that relatively low clay loadings can change the gas permeability greatly. There are a number of nanocomposites that come close to fitting the predictions of this simple model. Lan et al. [41] observed in polyimide nanocomposites that the relative permeability for O₂, CO₂, and H₂O fit the tortuous path model reasonably well but measurements on ethyl acetate exhibited a very large dependence on relative humidity. The relative permeability of ethyl acetate at 0% RH was 0.19 and at 50% RH it was 0.09. In contrast the pure polyimides more than double its permeability going from 0% to 50% RH. Chaiko and Leyva [42] reported that in a polypropylene wax composite that they observed 62 fold decreases in oxygen permeability at 5% weight loading of clay.



1.1.5.4 Mechanical properties

1.1.5.4.1 Dynamic mechanical analysis (DMA)

Dynamic mechanical analysis (DMA) measures the response of a given material to an oscillatory deformation (here in tension–torsion mode) as a function of temperature. DMA results are composed of three parameters: (a) the storage modulus (G'); (b) the loss modulus (G''); and (c) $\tan \delta$; the ratio (G''/G'); useful for determining the occurrence of molecular mobility transitions, such as the glass

transition temperature (T_g). [43]

The cyclic deformation of PS/MMT nanocomposites as a function of temperature was measured by DMA. The temperature dependence of storage modulus and $\tan\delta$ were shown in Figure 1-17 and 18, respectively. The storage modulus of PS/MMT nanocomposites were greater than that of pure PS and monotonically increased with the clay content in both the glassy and rubbery regions. However, the improvements in the rubbery region were much greater than those in the glassy region. This behavior indicates that the restricted segmental motions at the organic-inorganic interface are due to large aspect ratios of the clay platelets, and the polymer chains were also well confined inside the clay galleries at the nanoscale level. [44,45] The storage modulus of PS/MMT-3 was 1.2 times higher than that of pure PS, which is comparable to the earlier reported data (1.4 times improvement). [44] The T_g of the nanocomposites were estimated from the peak values of $\tan\delta$, which were shifted towards higher temperature with increasing the clay content. These results indicate that nanoscale clay platelets strongly restrict the polymer segmental motions, resulting in the significant increase in T_g . This improvement in T_g is higher than those of other researchers even though the smaller clay content was used in this experiment. [46,47]

The effects of clay loadings on tensile properties of the PS/MMT nanocomposites are shown in Figure 1-19. The tensile strength and Young's modulus

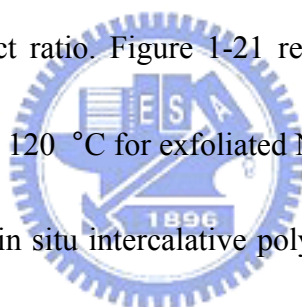
were significantly enhanced in the presence of the small contents of clay, while the elongation at break was reduced with increasing the clay content. The increase in tensile strength was attributed to the stronger interfacial adhesion between PS and the clay platelets. However, the enhancement of modulus was reasonably ascribed to the high resistance exerted by the clay platelets against the plastic deformation and the stretching resistance of the oriented polymer backbones in the galleries. The improvement of tensile strength in PS/MMT-3 compared to pure PS was ~47 %, which is greater than the earlier reported value in the literature (~21 %) for PS/MMT nanocomposite with 3 wt% MMT prepared by melt blending. [45] Similarly, the enhancement of Young's modulus in PS/MMT-3 compared to pure PS was ~25 %, which is much greater than the reported value (7.4 % improvement for PS/MMT nanocomposite with 5 wt% clay prepared by emulsion polymerization). [48] However, the elongations at break were reduced with increasing the clay content. Similar results were earlier reported. For example, the reduction of elongation at break in PS/MMT nanocomposite with 4.4 wt% MMT prepared by melt blending was reported to ~26 %.

[44]

1.1.5.4.2 Tensile properties

The tensile modulus of a polymeric material has been shown to be remarkably

improved when nanocomposites are formed with layered silicates. N6 nanocomposites prepared through the in situ intercalative ring opening polymerization of 1-caprolactam, leading to the formation of exfoliated nanocomposites, exhibit a drastic increase in the tensile properties at rather low filler content. The main reason for the drastic improvement in tensile modulus in N6 nanocomposites is the strong interaction between matrix and silicate layers via formation of hydrogen bonds, as shown in Figure 1-20. In the case of nanocomposites, the extent of the improvement of the modulus depends directly upon the average length of the dispersed clay particles, and hence the aspect ratio. Figure 1-21 represents the dependence of the tensile modulus E measured at 120 °C for exfoliated N6 nanocomposites with various clay content, obtained by the in situ intercalative polymerization of 1-caprolactam in the presence of protonated aminododecanoic acid-modified MMT and saponite. Moreover, the difference in the extent of exfoliation, as observed for N6-based nanocomposites synthesized by the in situ intercalative polymerization of 1-caprolactam using Nat-MMT and various acids, strongly influenced the final modulus of the nanocomposites.

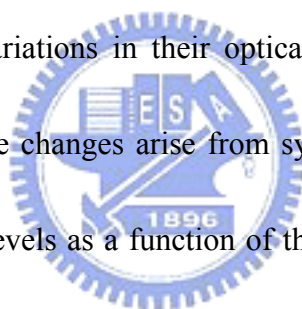


1.2 Introduction QDs nanocomposite

Nanoscience, nanotechnology, and nanobiotechnology (the Nanoworld) would not be as exciting as it is today if semiconductor quantum dots (QDs) and metal nanoparticles (NPs) did not show size-tunable optical properties. Coherent advancements in the synthesis and experimental and theoretical understanding of the structural, optical, electronic, and magnetic properties of semiconductor QDs and metal NPs created and strengthened the platform of the Nanoworld. Chemists, physicists, biologists, and technologists then interfaced semiconductor QDs, metal NPs, and their properties with organic, inorganic, and biomolecules/materials. This interfacing emerged into an exciting field of hybrid nanomaterials with potential applications in almost all the branches of science and technology today. The dimension of matter that is important to nanoscience and nanotechnology is typically on the 0.2- to 100-nm scale (nanoscale).

However, from the end of the 20th century through now on, the merge between the “top-down” (physics) and “bottom-up” processes toward the nano-scale territory has become obvious, and the relevant research has attracted much attention in the fields of chemistry, physics, material science and even molecular biology. Nowadays, “nanoscience” is believed to be the most popular terminology worldwide, and its mission may not be fulfilled without an interdisciplinary team work.

In these nanoscale regimes, particle sizes are between atoms and bulk materials, in which particle was close to molecules level. Two major effects are responsible for these size variations in nanocrystal properties. On one hand, in nanocrystals, the number of surface atoms is in a large fraction of the total, namely the surface-to-volume ratio is drastically increased as the size is decreased. On the other hand, intrinsic properties of the interior of nanocrystals are transformed from classical regime to the quantum size effects. Independent of the large number of surface atoms, semiconductor nanocrystals with the same interior bonding geometry as a known bulk phase often exhibit strong variations in their optical and electrical properties with respect to size. [51, 52] These changes arise from systematic transformations in the density of electronic energy levels as a function of the size of the interior, known as quantum size effects. As depicted in Figure 1-21, nanocrystals lie in between the atomic and molecular limit of discrete density of electronic states and the extended crystalline limit of continuous bands. [53, 54] During the past two decades, the ability to control the surfaces of semiconductors with near atomic precision has led to gain detailed insights into the semiconductor structures: quantum wells, wires, and dots. Neglecting for a moment the atomic level structure of the material, it is possible to imagine simple geometric objects of differing dimensionality in a degree of freedom of two, one, and zero, each case being made out of homogeneous semiconductor



material and with perfect surface termination.

Such structures should exhibit idealized variations in density of electronic states predicted by simple “particle in a box” type models of elementary quantum mechanics, with the continuous levels of the 3D case evolving into a discrete state of the zero-dimensional case (Figure 1-23). Recently, substantial progresses have been made in the preparation and characterization of materials consisting zero-dimensional quantum dots, particles with dimensions in the order of a few nanometers called “nanocrystalline materials”.[53-64] Tunable size and shape determining their physical properties like optical and transport properties open exciting possibilities for the creation of new functional materials used in unlimited applications.



1.2.1 Bulk semiconductors

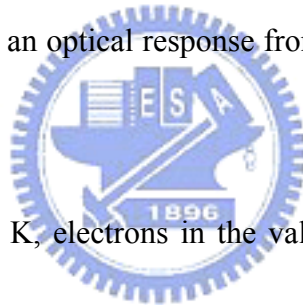
Macrocrystalline semiconductors, if they are free of defects, consist of three-dimensional networks of ordered atoms. The translational periodicity of the crystal imposes a special form on the electronic wave functions. An electron in the periodic potential field of a crystal can be described using a Bloch type wave function (eq. 1-1), where $u(r)$ represents a Bloch function modulating the plane wave $\phi(kr)$ of wave vector \mathbf{k} .

$$\psi(r) = \phi(kr)u(r) \quad (1-1)$$

$$u(r + n) = u(r) \quad n \text{ integer} \quad (1-2)$$

In a bulk semiconductor, the large number of atoms leads to the generation of sets of molecular orbitals with very similar energies, which effectively form a continuum. At 0 K the lower energy levels, or valence band, are filled with electrons, while the conduction band consisting of the higher energy levels is unoccupied. These two bands are separated by an energy gap (E_g), the magnitude of which is a characteristic property of the bulk macrocrystalline material at a specific temperature.

Materials normally considered as semiconductors typically exhibit band gaps in the range of 0.3–3.8 eV, covering an optical response from UV-Vis to higher energy side of the infrared region.



At temperatures above 0 K, electrons in the valence band may receive enough thermal energy to be excited across the band gap into the conduction band. An excited electron in the conduction band, together with the resulting hole in the valence band, forms an “electron-hole pair”. The conductivity (σ) of the semiconductor is governed by the number of electron-hole pairs, the charge carrier concentration (n , normally expressed in terms of the number of particles per cubic centimeter), and their mobility (μ). Thus conductivity can be expressed as the sum of the electrical conductivities of electrons and holes expressed in eq. 1-3, in which q denotes the charge of carrier. In conventional semiconductors, electrons and holes are the charge carriers. At ambient

temperature, they exist in small numbers as compared to those of the conductors.

However, it should be noted that the carrier mobilities in semiconductors are substantially larger than that in many conductors.

$$\sigma = qn_e\mu_e + qn_h\mu_h \quad (1-3)$$

The charge carriers in a semiconductor can form a bound state when they approach each other in space. This bound electron-hole pair, known as a Wannier exciton, is delocalized within the crystal lattice and experiences a screened Coulombic interaction. The Bohr radius of the bulk exciton is given in eq. 1-4 expressed as

$$a_B = \frac{\hbar^2 \epsilon}{e^2} \left[\frac{1}{m_e^*} + \frac{1}{m_h^*} \right] \quad (1-4)$$

where ϵ represents the bulk optical dielectric coefficient, e the elementary charge, and m_e^* and m_h^* the effective mass of the electron and hole, respectively.

1.2.2 Nanocrystalline semiconductors

Two fundamental factors, both related to the size of the individual nanocrystal, distinguish their behavior from the corresponding macrocrystalline material. The first is the high dispersity (large surface/volume ratio, vide supra) associated with the particles, with both the physical and chemical properties of the semiconductor being particularly sensitive to the surface structure. The second factor is the actual size of the particle, which can determine the electronic and physical properties of the material.

The absorption and scattering of incident light in larger colloidal particles can be described by Mie's theory. However the optical spectra of nanocrystalline compound semiconductors [53-62] which show blue shifts in their absorption edge as the size of the particle decreases cannot be explained by classical theory.[66-70] Such size dependent optical properties are examples of the size quantization effect which occurs [65] when the size of the nanoparticle is smaller than the bulk-exciton Bohr radius, a_B (see eq. 1-4), of the semiconductor. Equation 1-5 defines, for a spherical crystallite of radius R , the region of intermediate character between that of a "molecule" and that of the bulk material (l is the lattice spacing)

$$l \ll R \leq a_B \quad (1-5)$$

Charge carriers in semiconductor nanocrystallites are confined within three dimensions by the crystallite. In the case of ideal quantum confinement the wave function in eq. 1-1 has to satisfy the boundary conditions of

$$\psi(r \geq R) = 0 \quad (1-6)$$

For nanoparticles the electron and hole are closer together than in the macrocrystalline material, and as such the Coulombic interaction between electron and hole cannot be neglected; they have higher kinetic energy than in the macrocrystalline material. On the basis of the effective mass approximation, Brus showed [57,68,69] for CdS or CdSe nanocrystallites that the size dependence on the

energy of the first electronic transition of the exciton (or the band gap shift with respect to the typical bulk value) can be approximately calculated using

$$\Delta E \cong \frac{\hbar^2 \pi^2}{2R^2} \left[\frac{1}{m_e^*} - \frac{1}{m_h^*} \right] - \frac{1.8e^2}{\epsilon R} \quad (1-7)$$

Equation 1-7 is an analytical approximation for the first electronic transition of an exciton, which can be further described by a hydrogenic Hamiltonian,

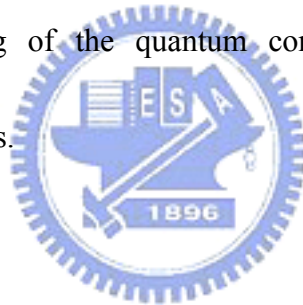
$$\hat{H} = \frac{-\hbar^2}{2m_e^*} \nabla_e^2 - \frac{-\hbar^2}{2m_h^*} \nabla_h^2 - \frac{e^2}{\epsilon |re - rh|} \quad (1-8)$$

In eq. 1-7 the Coulomb term shifts the first excited electronic state to lower energy, R^{-1} , while the quantum localization terms shift the state to higher energy, R^{-2} . Consequently, the first excitonic transition (or band gap) increases in energy with decreasing particle diameter. This prediction has been confirmed experimentally for a wide range of semiconductor nanocrystallites, [53-62] with a blue shift in the onset of the absorption of light being observed with decreasing particle diameter. Moreover, the *valence* and *conduction bands* in nanocrystalline materials consist of discrete sets of electronic levels and can be viewed as a state of matter between that of molecular and the bulk material.

Equation 1-7 does not account for a number of other important effects observed in real nanocrystallites, [70] such as the coupling of electronic states and effects attributable to surface structure. Especially, the constants used in the model (the

effective masses and the dielectric constants) are those for macrocrystalline solids.

The model is not quantitatively accurate and the corresponding calculations deviate from experimental values, especially for nanocrystallites with a very small size. In such particles the first electronic transition is located in a region of the energy band, in which the normal effective mass approximation is not valid. Although eq. 1-7 is not valid for all types of semiconductors, from a practical point of view, this model is particularly useful and the size-dependent energy shift for a number of nanocrystalline semiconductors can be qualitatively estimated. Furthermore, the model also provides a fundamental understanding of the quantum confinement effects observed in semiconductor nanocrystallites.

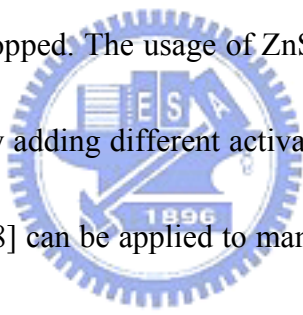


1.2.3 Introduction of the II-VI ZnS material

Zinc sulfide (ZnS) with an appearance of yellow-white powders has been utilized extensively as the phosphors. Two structures exist in ZnS materials, one is zinc blend or sphalerite (β -ZnS), the atomic arrangement is cubic structure as shown in Figure 1-24(a), and another is wurtzite (α -ZnS), the atomic arrangement is hexagonal structure as shown in Figure 1-24 (b). In nature, ZnS usually exists in the type of zinc blend, and if the environment temperature is higher than 1020°C it will convert into wurtzite phase. No matter what type it is, the luminescence phenomena are all

observed [71].

The research of ZnS had been begun from 1866 in France. In 1920's, several reports of influences on the activator (like Cu, Ag) and self-activated luminescence have been discussed. Since 1940, the investigations of the II-VI ZnS-based phosphors are active and abundant. In 1966, an article "100 anniversary of color ZnS" was published to show the importance of ZnS in an international conference. In 1990's, Bhargava *et al.* [72] reported the properties of Mn^{2+} doped ZnS phosphors, and it has been attracted a lot of attention [73-77]. Till now, the researches of ZnS-based phosphors have been never stopped. The usage of ZnS phosphors in the past time are used as the luminous paint. By adding different activators, ZnS-based phosphors with different emission energies [78] can be applied to many usages as shown in table 5-1. Now, due to the special photoelectric properties, the ZnS-based phosphors are widely used in photoelectric industry like photocatalyst, light emitting diode and high-density optical storage media.



Phosphor	Emission Color	Applications
ZnS : Ag	Blue	Monochrome and color TV
(Zn, Cd)S : Ag	Yellow-Green	Oscilloscope
ZnS : Cu, Al	Yellow-Green	Monochrome and color TV
(Zn, Cd)S : Cu, Al	Yellow-Green	Monochrome and color TV
ZnS : Cu, Pm	Green	Luminous Paint

Table 1-1 Applications of the ZnS-based phosphors doping with different activators.

1.2.4 Properties of nanostructure [79-82]

All materials are composed of proper chemical bonds with atoms, including metallic bond, ionic bond, covalent bond, Van der waal's bond and hydrogen bond. The bonding length is the distance between two atoms as the net interaction force is zero. And the curve integrated by the net interaction force to the atom interval can obtain the lowest potential at this length of bonding. These bonding properties not only correspond to the mechanical properties of the materials but also the thermal properties. Solid status material is not just the agglomeration of atoms; the energy levels of each electron form the bonding orbits and anti-bonding orbits, and the number of orbit increases with the number of chemical bonding. As the number of orbit increases, the difference between the energy levels decreases and results in the continuous energy states. The distribution and value of the solid state energy level are highly related to the species and number of the bonding atoms, and influence the physics or chemical properties such as electric property, optical property, magnetic property and photoelectric properties. Nanostructure is the one-dimensional material with volume lies in 1 to 100 nm, including nanoparticles and quantum dots. In these nanomaterials, the number and distribution of the atoms change rapidly with the decrease in material size. Thus the bonding properties and the energy level properties is quite different from the bluk matrials. There are four effects such as surface effect,

small size effect, quantum size effect and quantum confinement effect listed below.

1.2.4.1 Surface effect

With the scale becomes small, the number of atoms on the particle surface increases. Because of these surface atoms are not completely coordinated, it is unstable and possesses high surface potential, thus, it possesses high chemical activity and easily bonds with other atoms. The activity effect of surface atoms is the major factor to produce the activity of the inert-noble metal catalyst. The number of near atoms on the particle surface is smaller than that inside the particle. With large ratio of the surface area, it will result in the reduction of the bonding length and the variation of the lattice arrangement. Because of the reduction in bonding length, the Curie temperature (T_c) therefore decreases with the smaller particle size. Besides, in tiny metal particles, because the surface energy increases due to the particle shrinkage, the necessary heat to diffuse atoms is much smaller than the bulk materials. It is the reason why that the melting point of the metal nanoparticles decreases so fast.

1.2.4.2 Small size effect

In order to prevent the motion of dislocations, the decrease in particle size is applied. This method is applied to increase the mechanical intensity of the polycrystal.

In many materials, the σ_y (or hardness H) increases with the particle size decreased and can be expressed by the Hall-Petch equation :

$$\sigma_y = \sigma_0 + Kd^{-1/2} \quad (1-8)$$

$$H = H_0 + Kd^{-1/2} \quad (1-9)$$

Where, σ_0 , H_0 and K are the constants and d is the average particle diameter. In general, the value of K is positive, and σ_y or H is linearly proportional to the value of $d^{-1/2}$. In the nanocrystals, however, the scale is close to the intervals of the near dislocations, so the relation of the hardness and the particle size can not be explained by the above formula. It has the complex relations of positive K value, negative K value and mixed positive-negative K value. Due to the grain boundaries with great volume ratio in the nanocrystal, the plasticity, strike toughness and break toughness are improved. The high mechanical intensity and the super plasticity precise-ceramics could be obtained by controlling the crystal size at the critical range.

1.2.4.3 Quantum size effect

In the theorem of energy band, the energy levels of metal near the Fermi energy level is a continuous distribution. As the particle size decreases, it becomes to the discrete energy level. Furthermore, the Kubo theorem describes the relation between the interval of electron energy level δ and the diameter (d) of the metal nanoparticle:

$$\delta = \frac{4E_F}{3N} - \frac{1}{d^3} \quad (1-10)$$

Where, N is the total number of the conduction electrons, E_F is the Fermi level. It could be seen that the decrease in the particle diameter increases the energy of band gap. This quantum size effect results in the broadening of the energy band gap in the nanoscale semiconductors and the discontinuous energy level of the valence band and the conduction band. With a decrease in the size of the nanoscale semiconductor particle, the blue shift in the absorption spectrum is observed due to the enlargement of the energy band gap. The emission wavelength resulted from the energy band gap in the nanoscale semiconductor shifts to the short wavelength because of the broadening in the energy gap. In other words, the different emission color can be obtained by controlling the size of the particles.

1.2.4.4 Quantum confinement effect

According to the Heisenberg uncertainty principle, the actual position and the momentum of an electron or a photon cannot be obtained at the same time. If the electron is restricted in a small nanoscale space, the momentum range is wide. And if the momentum range is wide, the average energy of the electrons is high. Thus on the boundaries of this range, there exists the phenomenon of quantization jumping, as shown in Figure 1-25. If the particle radius (r) of the nanoscale semiconductor is

smaller than the Bohr radius (a_B) of the exciton, the average mean free path of electron is restricted in a small space, then the electron and hole are easy to be combined to a excitation. The absorption energy band of the excitation resulted from the overlapping of the electron and hole's wave functions not only has strong excitonic energy-band-gap absorption coefficient but also has great light emission phenomenon as being excited by light.

1.2.5 Emission theory

Luminescence is defined as a material absorbs the excitation energy, and then electrons transfer from the ground state to the excited state. As electrons return to the ground state and release energy in light, this phenomenon is called luminescence and can be explained by the configuration coordinate diagrams, as shown in Figure 1-26. [83].

When phosphors are excited by the ultraviolet light, part of the ultraviolet light will be reflected by the surface and the other part will be absorbed by the phosphor and transfer into luminescence radiation or the vibration of the lattice, as shown in Fig. 1-27.

The process which an electron absorbs energy, and then transfers from the ground state to the excited state is called excitation. The electron in the excited state

possesses higher energy so it is usually unstable and drives the electron to return to the ground state and release energy. The progress of this energy release is called “Relaxation”. There are two kinds of relaxation, one is radiative relaxation and another is nonradiative relaxation. The energy released in the progress of radiative relaxation is in the form of electromagnative radiation, in a word, it radiates electromagnative wave. When the wavelength of electromagnative wave is located in the range of visible light, we can observe the emission light lucid. And in the nonradiative relaxation, the energy is released in the form of “heat”. This type of relaxation will not emit light. The relaxation progress is shown in Figure 1-28. The relaxation progress can be described simply:



◆ Radiative Relaxation: The excited electron returns to the ground state and emits visible light.

◆ Nonradiative Relaxation: The excited electron returns to ground state and produces heat without emitting light.

According to the theorem of Franck-Condon, the speed of electron transfer is much fast so the distance R in nucleus almost unchanged. If the difference between the balance distance R_0 in the ground and the balance distance R'_0 in the excited state is $\Delta R = (R'_0) - (R_0)$ as shown in Figure 5-5.

(1-11)

The existence of ΔR is due to the vibration-coupling resulted from the mutual interaction between the matrix lattice and the activated center. When the $R > R_0$ or $R < R_0$, due to the mutual interaction between the matrix lattice and the activated center, it will produce vibration coupling because of the phonon wave propagation. If the $\Delta R > > 0$, it is called strong coupling and broadens absorption peak of the emission spectrum. If $\Delta R = 0$, is called zero-transition or non-phonon transition, the interaction is weak so the absorption peak of the emission spectrum is narrow.

1.2.5.1 Fluorescence and non-radiative transfer

The existence of radiation field is necessary for the light absorption. When the activate centers absorb energy, the electron will transfer into the lowest vibration energy level of the excited state, and then gives the energy to surrounding lattice for relaxation. And the absorption band will move to the lower energy level, this shift is called Stokes shift as in Figurer 1-29. [83]

Stokes shift is defined to be the energy loss in relaxation, it can be presented by the below formula.

$$\text{Stokes shift} = 2Sh\nu \quad (1-12)$$

Where, S is the Huang-Rhys coefficient, the integral factor of the electron-lattice coupling. And $h\nu$ is the energy interval between two vibration energy levels.

When $S < 1$, it is weak coupling.

$1 < S < 5$, it is intermediate coupling.

$S > 5$, it is strong coupling, as shown in Figure 1-30. [83]

The Stokes shift is directly proportional to $(\Delta R)^2$, so the larger value of ΔR results in the larger Stokes shift and broadens the emission peak in the spectrum. Absorption of the materials may release energy in non-radiative ways. In order to ensure the emission efficiency, less non-radiative relaxation in the phosphor is required. In general, the efficiency of light emission relates to the ion radius. In phosphors, the larger ion radius results in a larger ΔR . It could be said that the environment is softer so the ΔR is larger and the crystal property is worse as well. In order to obtain good emission efficiency, a stiff lattice is required.

1.3 Introduction of stimuli response polymer

Stimuli responsive polymers can provide a variety of applications for the biomedical fields. The interest in these polymers has exponentially increased due to their promising potential. Among them, temperature and pH responsive mechanisms have been considerably investigated because they are relatively convenient and effective stimuli in many applications.

In all these cases the key parameter defining the responsive or 'smart' behaviour

of the polymers is a non-linear response to an external signal. The responses can also be manifold: dissolution/precipitation, degradation, drug release, change in hydration state, swelling/collapsing, hydrophilic/hydrophobic surface, change in shape, conformational change and micellisation (Figure 1-31). The most important stimuli are pH, temperature, ionic strength, light and redox potential [84,85].

1.3.1 Thermo-responsive polymers

Temperature-responsive polymers and hydrogels exhibit a volume phase transition at a certain temperature, which causes a sudden change in the solvation state. Polymers, which become insoluble upon heating, have a so-called lower critical solution temperature (LCST), as showing in Figure 1-32. Systems, which become soluble upon heating, have an upper critical solution temperature (UCST). LCST and UCST systems are not restricted to an aqueous solvent environment, but only the aqueous systems are of interest for biomedical applications. The change in the hydration state, which causes the volume phase transition, reflects competing hydrogen bonding properties, where intra- and intermolecular hydrogen bonding of the polymer molecules are favoured compared to a solubilisation by water. Thermodynamics can explain this with a balance between entropic effects due to the dissolution process itself and due to the ordered state of water molecules in the

vicinity of the polymer. Enthalpic effects are due to the balance between intra- and intermolecular forces and due to solvation, e.g. hydrogen bonding and hydrophobic interaction. The transition is then accompanied by coil-to-globule transition.

For example, poly(Nisopropylacrylamide) (PNIPAAm) has a LCST, at which it undergoes a reversible volume phase transition caused by the coil-to-globule transition [86]. Intramolecular collapse occurs before intermolecular aggregation through LCST and the collapse of individual polymer chains increases the scattering of light in solution (cloud point). Phase separation between the collapsed polymer molecules and the expelled water follows this cloud point [87].



1.3.2 PH responsive polymers

A pH-responsive conformation with solubility changes is common behavior in biopolymers. The pH-responsive polymers consist of ionizable pendants that can accept and donate protons in response to the environmental change in pH. As the environmental pH changes, the degree of ionization in a polymer bearing weakly ionizable groups is dramatically altered at a specific pH that is called pKa. This rapid change in net charge of pendant groups causes an alternation of the hydrodynamic volume of the polymer chains. The transition from collapsed state to expanded state is

explained by the osmotic pressure exerted by mobile counterions neutralizing the network charges [88]. The polymers containing ionizable groups in their backbone form polyelectrolytes in the aqueous system. There are two types of pH-responsive polyelectrolytes; weak polyacids and weak polybases. The representative acidic pendant group of weak polyacids is the carboxylic group. Weak polyacids such as poly(acrylic acid) (PAAc) accept protons at low pH and release protons at neutral and high pH. [89]

The same group also prepared diblock copolymers that formed two types of micelles in aqueous solution depending on pH.[90–92] These resulting states were described as ‘schizophrenic’ since by changing external pH, temperature or ionic strength the more hydrophilic block could be transformed to a hydrophobic state in order to form the core of a micelle. By altering pH again, the second block became hydrophobic, effectively switching the micelle. The key to this behaviour was in choosing the correct polymer block components (Figure 1-33): the use of poly(4-vinylbenzoic acid) ($pK_a = 7.1$) as one block and poly(2-N-(morpholino)ethylmethacrylate) (pK_a of the conjugate acid = 4.9) ensured that precipitation did not occur during pH variation across the isoelectric point.

Reference

- [1] Tanoue, S.; Utracki, L.A.; Garcia-Rejon, A.; Sammut, P.; Ton-That, M.T.; Pesneau, I.; Kamal, M.R.; Lyngaae-Jorgensen, J. *Polym. Eng. Sci.* **2004**, 44, 1061.
- [2] Yoshimoto, S.; Ohashi, F.; Kameyama, T. *Macromol. Rapid Commun.* **2005**, 26, 461.
- [3] Kairn, T.; Daivis, P.J.; Ivanov, I.; Bhattacharya, S.N. *J. Chem. Phys.* **2005**, 123, 194905.
- [4] Abranyi, A.; Szazdi, L.; Pukanszky, B.; Vancso, G.J.; Pukanszky, B. *Macromol. Rapid Commun.* **2006**, 27, 132.
- [5] Wegner, G.; Meisel, I.; Nohl, R. *Macromol. Rapid Commun.* **2005**, 26, 9.
- [6] Park, J.H.; Kim, W.N.; Kye, H.S.; Lee, S.S.; Park, M.; Kim, J.; Lim, S. *Macromol. Res.* **2005**, 13, 367.
- [7] Alexandre, M.; Beyer, G.; Henrist, C.; Cloots, R.; Rulmont, A.; Jerome, R.; Dubois, P. *Macromol. Rapid Commun.* **2001**, 22, 643.
- [8] Gilman, J.W.; Jackson, C.L.; Morgan, A.B.; Harris, R. *Chem. Mater.* **2000**, 12, 1866.
- [9] Yong, Y.; Zhn, Z.; Yin, J.; Wang, X.; Qi, Z. *Polymer* **1999**, 40, 4407.
- [10] Sinha Ray, S.; Okamoto, M. *Macromol. Rapid Commun.* **2003**, 24, 815.
- [11] Burnside, S.D.; Giannelis, E.P. *Chem. Mater.* **1995**, 7, 1597.

- [12] Usuki, A.; Kojima, Y.; Okada, A.; Fukushima, Y.; Kurauchi, T.; Kamigaito, O. *J. Mater. Res.* **1993**, 8, 1174.
- [13] Giannelis, E. P. *Adv. Mater.* **1996**, 8, 29.
- [14] Krishnamoorti, R.; Vaia, R. A.; Giannelis, E. P. *Chem. Mater.* **1996**, 8, 1728.
- [15] Yei, D. R.; Kuo, S. W.; Su, Y. C.; Chang, F. C. *Polymer* **2004**, 45, 2633.
- [16] Tseng, C. R.; Wu, J. Y.; Lee, H. Y.; Chang, F. C. *Polymer* **2001**, 42, 10063.
- [17] Tseng, C. R.; Lee, H. Y.; Chang, F. C. *J. Polym. Sci. Part B: Polym. Phys.* **2001**, 39, 2097.
- [18] Chen, H. W.; Chiu, C. Y.; Chang, F. C. *J. Polym. Sci. Part B: Polym. Phys.* **2002**, 40, 1342.
- [19] Tseng, C. R.; Wu, J. Y.; Lee, H. Y.; Chang, F. C. *J. Appl. Polym. Sci.* **2002**, 85, 1370.
- [20] Tseng, C. R.; Wu, H. D.; Wu, J. Y.; Chang, F. C. *J. Appl. Polym. Sci.* **2002**, 86, 2492.
- [21] Dongyan, W.; Jin, Z.; Qiang, Y.; Charles, A. W. *Chem. Mater.* **2002**, 14, 3837.
- [22] Okada, A.; Kawasumi, M.; Usuki, A.; Kojima, Y.; Kurauchi, T.; Kamigaito, O. *Mater. Res. Soc. Symp. Proc.* **1990**, 171, 45.
- [23] Okada, A.; Kawasumi, M.; Kurauchi, T.; Kamigaito, O. *Polym. Prepr.* **1987**, 28, 447.

- [24] Kojima, Y.; Usuki, A.; Kawasumi, M.; Okada, A.; Kurauchi, T.; Kamigaito, O. J. Polym. Sci. Part A: Polym. Chem. **1993**, 31, 983.
- [25] Usuki, A.; Kojima, Y.; Kawasumi, M.; Okada, A.; Fukushima, T.; Kurauchi, T.; Kamigaito, O. J. Mater. Res. **1993**, 8, 1179.
- [26] Yano, K.; Usuki, A.; Okada, A.; Kurauchi, T.; Kamigaito, O. J. Polym. Sci. Part A: Polym. Chem. **1993**, 31, 2493.
- [27] Okada, A.; Usuki, A. Mater. Sci. Eng. **1995**, 3, 109.
- [28] Lan, T.; Pinnavaia, T. J. Chem. Mater. **1994**, 6, 2216.
- [29] Lan, T.; Pinnavaia, T. J. Chem. Mater. **1994**, 6, 573.
- [30] Kojima, Y.; Usuki, A.; Kawasumi, M.; Okada, A.; Kurauchi, T.; Kamigaito, O. J. Polym. Sci., Part A: Polym. Chem. **1993**, 31, 983.
- [31] Dubreuil, M. F.; Goethals, E. J. Macromol. Chem. Phys. **1997**, 10, 3077.
- [32] Tasdelen, M. A.; Van Camp, W.; Goethals, E.; Dubois, P.; Du Prez, F.; Yagci, Y. Macromolecules **2008**, 16, 6035.
- [33] Tong, J. D.; Du Prez, F. E.; Goethals, E. J. Macromolecules **2001**, 4, 761.
- [34] Ginzburg, V. V.; Balazs, A. C. Adv. Mater. **2000**, 12, 1805.
- [35] Kuznetsov, D. V.; Balazs, A. C. J. Chem. Phys. **2000**, 112, 4365.
- [36] Di, J.; Sogah, D. Y. Macromolecules **2006**, 3, 1020.

- [37] Zhu, J.; Alexander, B. M.; Frank, J. L.; Charles, A. W. Chem. Mater. **2001**, 13, 3774.
- [38] Gilman, J. W.; Jackson, C. L.; Morgan, A. B.; Harris, R.; Giannelis, E. P.; Phillips, S. H. Chem. Mater. **2000**, 12, 1866.
- [39] Zeng, C.; Lee, L. J. Macromolecules **2001**, 34, 4098.
- [40] Nielsen, L. E. J. Macromol. Sci. **1967**, A1, 929.
- [41] Lan, T.; Kaviratna, P. D.; Pinnavaia, T.J. Chem. Mater. **1994**, 6, 573.
- [42] Chaiko, D. J.; Leyva, A. A. Chem. Mater. **2005**, 17, 13.
- [43] Sinha Ray, S.; Okamoto, K.; Okamoto, M. Macromolecules **2003**, 36, 2355.
- [44] Hasegawa, N.; Okamoto, H.; Kawasumi, M.; Usuki, A. J. Appl. Polym. Sci. 1999, 74, 3359.
- [45] Park, C. I.; Choi, W. M.; Kim, M. K.; Park, O. O. J. Polym. Sci. Part B: Polym. Phys. **2004**, 42, 1685.
- [46] Fu, X.; Qutubuddin, S. Mater. Lett. **2000**, 42, 12.
- [47] Kim, Y. K.; Choi, Y. S.; Wang, K. H.; Chung, I. J. Chem. Mater. **2002**, 14, 4990.
- [48] Noh, M. W.; Lee, D. C. Polym. Bull. **1999**, 42, 619.
- [49] Uthirakumar, P.; Song, M.K.; Nah, C.; Lee, Y.S. Euro. Polym. J. **2005**, 41, 211.
- [50] Kojima, Y.; Usuki, A.; Kawasumi, M.; Okada, A.; Fukushima, Y.; Kurauchi, T.; Kamigaito, O. J. Mater. Res. **1993**, 8, 1185.

- [51] Ekimov, A. I.; Onuschenko, A. A. *Sov. Phys. Semicond.* **1982**, 16, 775.
- [52] Rossetti, R.; Nakahara, S.; Brus, L. E. *J. Chem. Phys.* **1983**, 79, 1086.
- [53] Alivisatos, A. P. *Science* **1996**, 271, 933.
- [54] Alivisatos, A. P. *J. Phys. Chem.* **1996**, 100, 13226.
- [55] Henglein, A. *Chem. Rev.* **1989**, 89, 1861.
- [56] Wang, Z. L.; Ahmad, T. S.; El-Sayed, M. A. *Surf. Sci.*, **1997**, 380, 302.
- [57] Steigerwald, M. L.; Brus, L. E. *Acc. Chem. Res.* **1990**, 23, 183.
- [58] Bawendi, M. G.; Steigerwald, M. L.; Brus, L. E. *Annu. Rev. Phys. Chem.* **1990**, 41, 477.
- [59] Weller, H. *Angew. Chem., Int. Ed. Engl.* **1993**, 32, 41.
- [60] Weller, H. *Adv. Mater.* **1993**, 5, 88.
- [61] Hagfeldt, A.; Grätzel, M. *Chem. Rev.* **1995**, 95, 49.
- [62] Fendler, J. H.; Meldrum, F. C. *Adv. Mater.* **1995**, 7, 607.
- [63] Stroscio, J. A.; Eigler, D. M. *Science* **1991**, 254, 1319.
- [64] Lieber, C. M.; Liu, J.; Sheehan, P. *Angew. Chem., Int. Ed. Engl.* **1996**, 35, 687.
- [65] Trindade, T.; O'Brien, P.; Pickett, N. L. *Chem. Mater.* **2001**, 13, 3843.
- [66] Haug, H.; Koch, S. W. *Quantum theory of the optical and electronic properties of semiconductors*; World Scientific Publishing Co. Pte. Ltd.: London, **1990**, p. 333.

- [67] Éfros, Al. L.; Éfros, A. L. Sov. Phys. Semicond. **1982**, 16, 772.
- [68] Brus, L. E. J. Chem. Phys. **1983**, 79, 5566.
- [69] Brus, L. E. J. Chem. Phys. **1984**, 80, 4403.
- [70] Brus, L. J. Phys. Chem. **1986**, 90, 2555.
- [71] Leverenz, H. W. "Luminescence of Solids", John Wiley & Sons, Inc., New York, **1950**.
- [72] Bhargave, R. N.; Gallagher, D.; Hong, X.; Nurmikko, A. Phys. Rev. Lett. **1994**, 72, 416.
- [73] Yang, H.; Wang, Z.; Song, L.; Zhao, M.; Chen, Y.; Dou, K.; Yu, J.; Wang, L. Materials Chemistry and Physics **1997**, **47**, 249.
- [74] Gan, L. M.; Liu, B.; Chua, S. J.; Loy, G. L.; Xu, G. Q. Langmuir **1997**, 13, 6427.
- [75] Ihara, M.; Igarashi, T.; Kusunoki, T.; Ohno, K. J. Electrochem. Soc. **2000**, 6, 2355.
- [76] Li, Y.; Ding, Y.; Zhang, Y.; Qian, Y. J. Physics and Chemistry of Solids **1999**, 60, 13.
- [77] Sooklal, K.; Cullum, B. S.; Angel, S. M.; Murphy, C. J. J. Phys. Chem. **1996**, 100, 4551.
- [78] 熊怡之, 碩士論文, 清華大學化學工程研究所, **1989** 年.

- [79] Yoffe, A. D. *Adv. Phys.* **2002**, 51, 799.
- [80] Weisbuch, C.; Benisty, H.; R. Houdré, J. *Lumin.* **2000**, 85, 271.
- [81] Kamat, P. V. *J. Phys. Chem. B* **2002**, 106 7729.
- [82] Xia, Y. *Adv. Mater.* **2000**, 12, 693.
- [83] Blasse, G.; Grabmaier, B.C. “*Luminescent Materials*”, Springer Verlag, Berlin Heidelberg, Germany (**1994**).
- [84] Hoffman, A.S. *Polym. Gels* **1991**, 268, 82.
- [85] Delas Heras Alarcon, C.; Pennadam, S.; Alexander, C. *Chem. Soc. Rev.* **2005**, 34, 276.
- [86] Dautzenberg, H.; Gao, Y.; Hahn, M. *Langmuir* **2000**, 16, 9070.
- [87] Schild, H. G. *Prog. Polym. Sci.* **1992**, 17, 163.
- [88] Tonge, S. R.; Tighe, B.J. *Adv. Drug Deliv. Rev.* **2001**, 53, 109.
- [89] Philippova, O. E.; Hourdet, D.; Audebert, R.; Khokhlov, A. R. *Macromolecules* **1997**, 30, 8278.
- [90] Liu, S. Y.; Armes, S. P. *Langmuir* **2003**, 19, 4432.
- [91] Liu, S. Y.; Armes, S. P. *Angew. Chem., Int. Ed.* **2002**, 41, 1413.
- [92] Weaver, J. V. M.; Armes, S. P.; Butun, V. *Chem. Commun.* **2002**, 18, 2122.

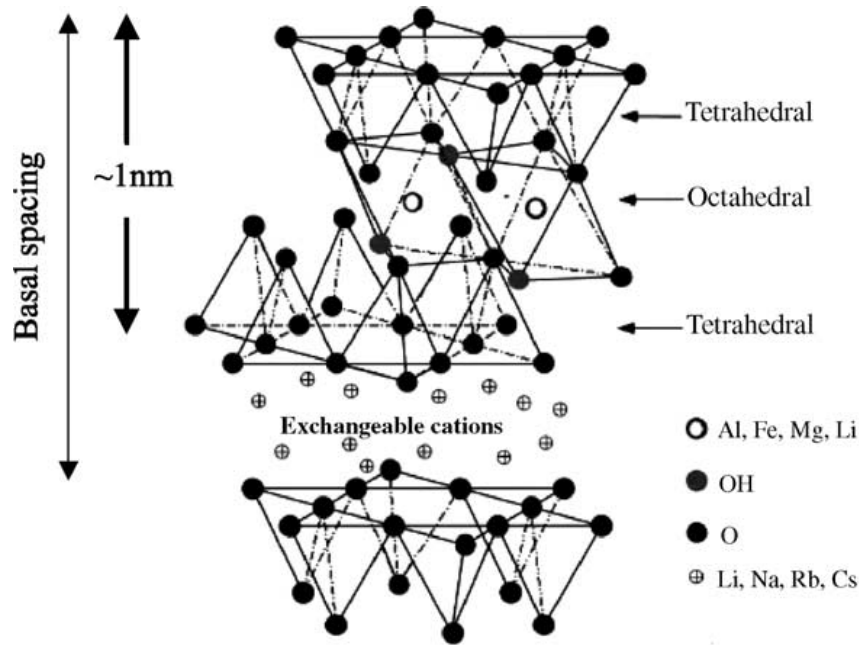


Figure 1-1. Structure of 2:1 layered silicates.

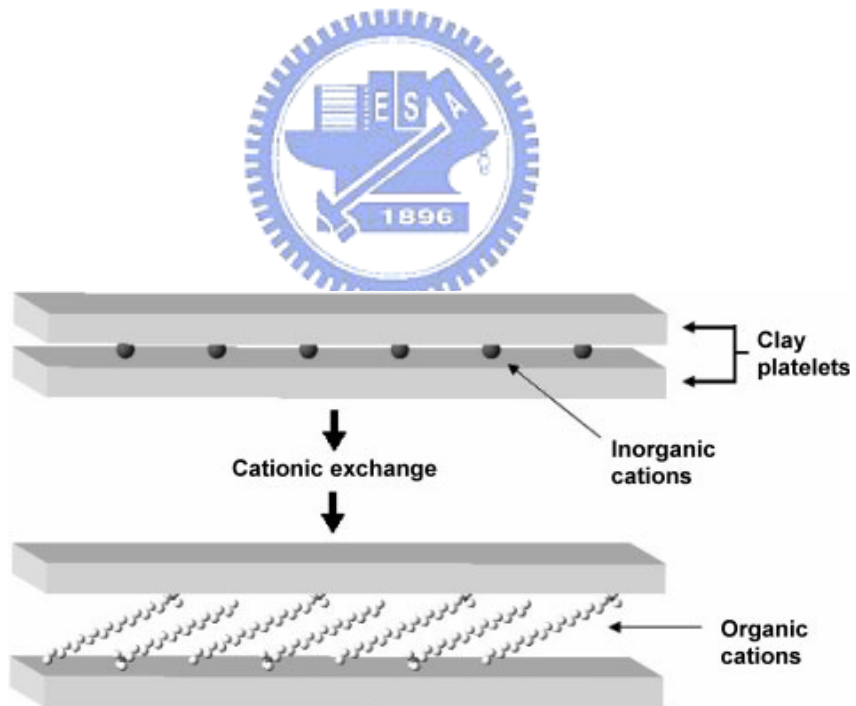


Figure 1-2. Scheme of effect of cationic exchange on interlayer spacing.

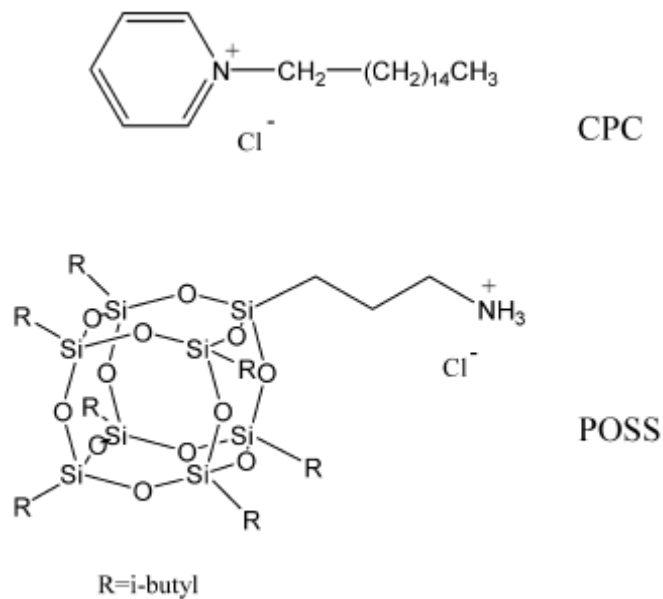


Figure 1-3. Chemical structures of the surfactants used to prepare the modified clays. [15]

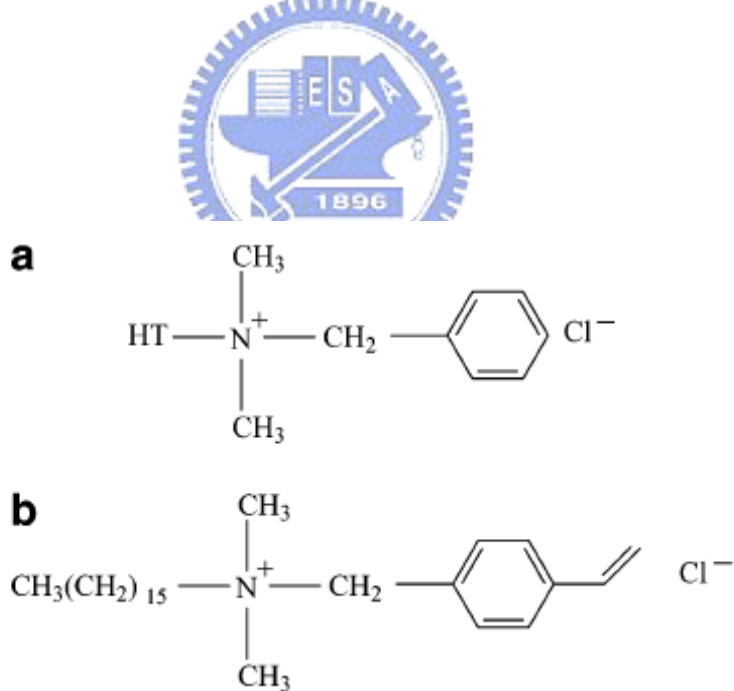


Figure 1-4. (a) Chemical structure of organic clay 10A, in which HT is hydrogenated tallow with ~65% C18, ~30% C16, and ~5% C14. (b) Chemical structure of organic clay VB16. [21]

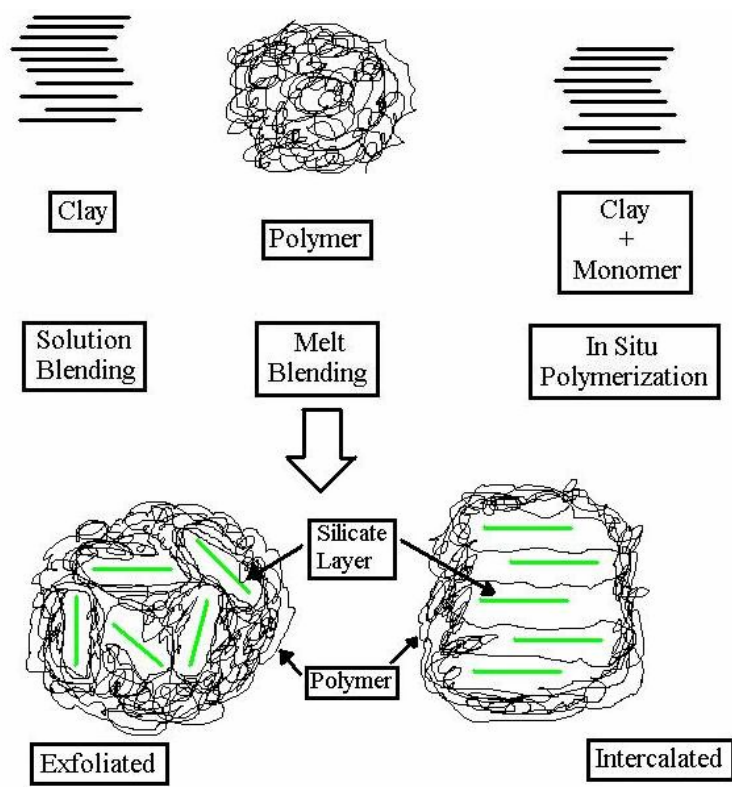


Figure 1-5. Schematic representation of various methods used to prepare polymer-layered-silicate nanocomposites. [30]

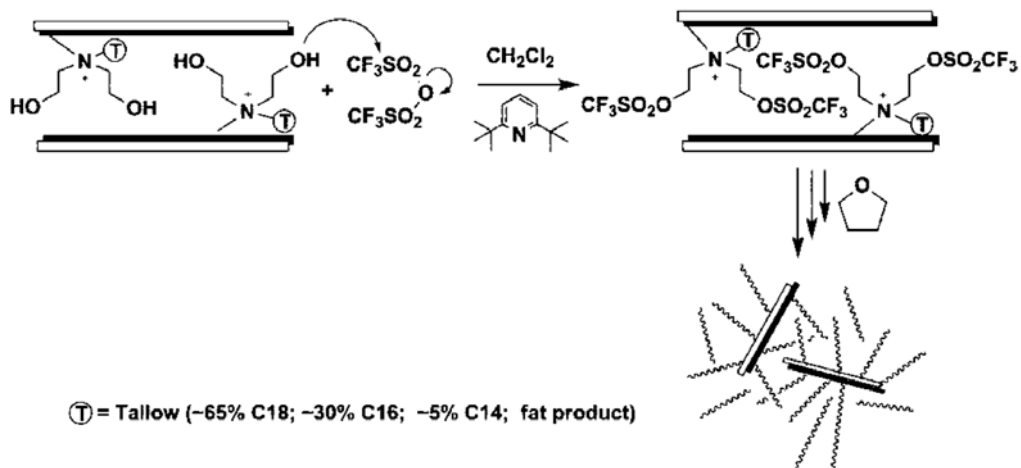


Figure 1-6. Preparation of polytetrahydrofuran/montmorillonite clay nanocomposites by in situ cationic ring opening polymerization. [32]

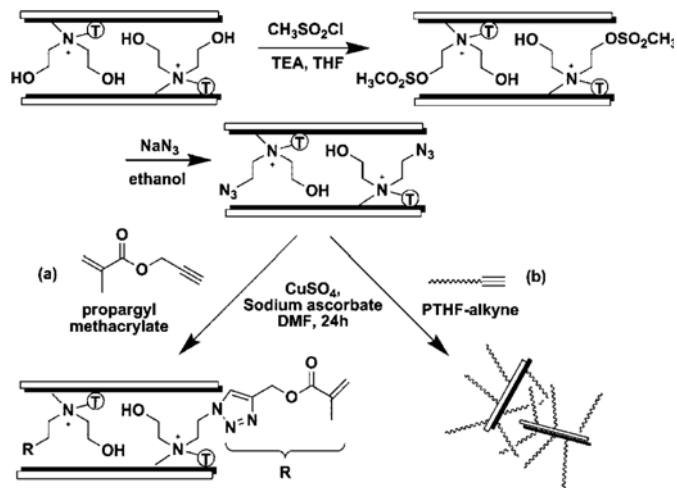


Figure 1-7. (a) Azide-functionalized montmorillonite clay and its “Click” reactions with propargyl methacrylate and (b) Alkyne-functionalized polytetrahydrofuran. [32]

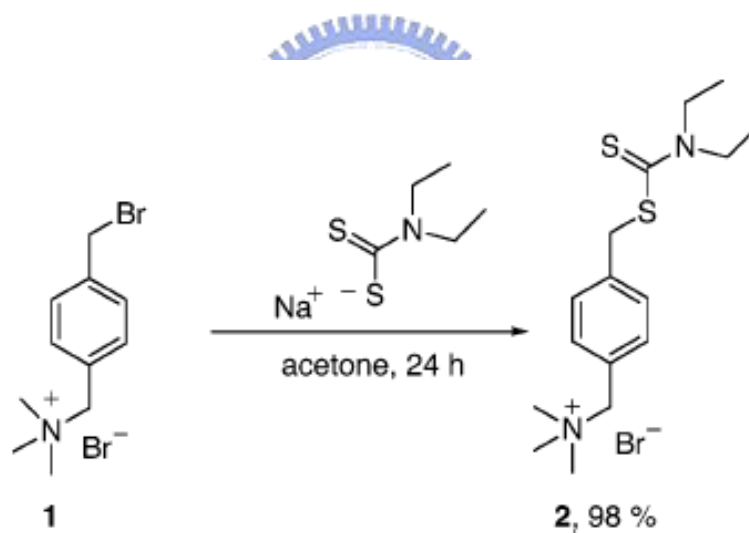


Figure 1-8. The synthesis of the photoiniferter progress. [36]

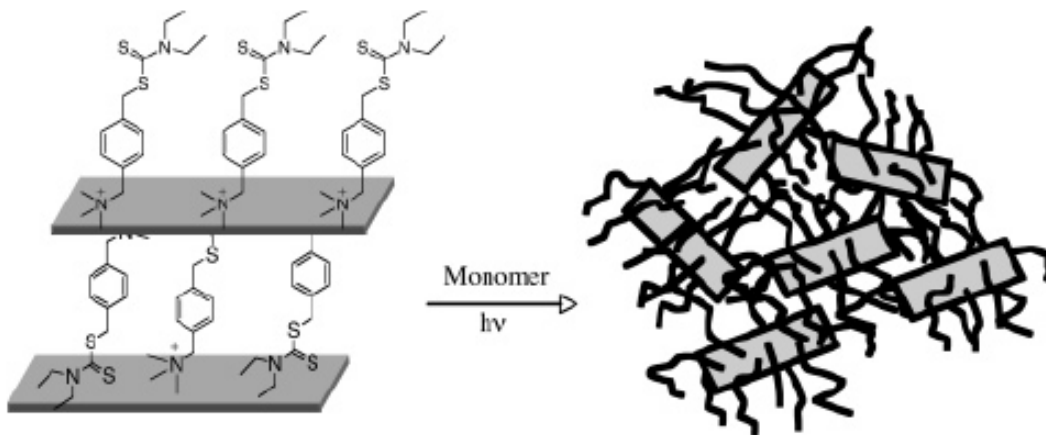


Figure 1-9. The concept of in situ living polymerization from the silicate-anchored

photoinitiator. [36]

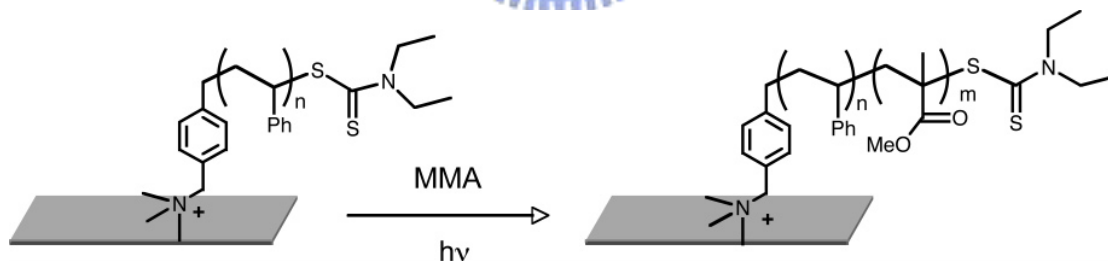


Figure 1-10. The preparation of block copolymers by sequential addition of

monomers. [36]

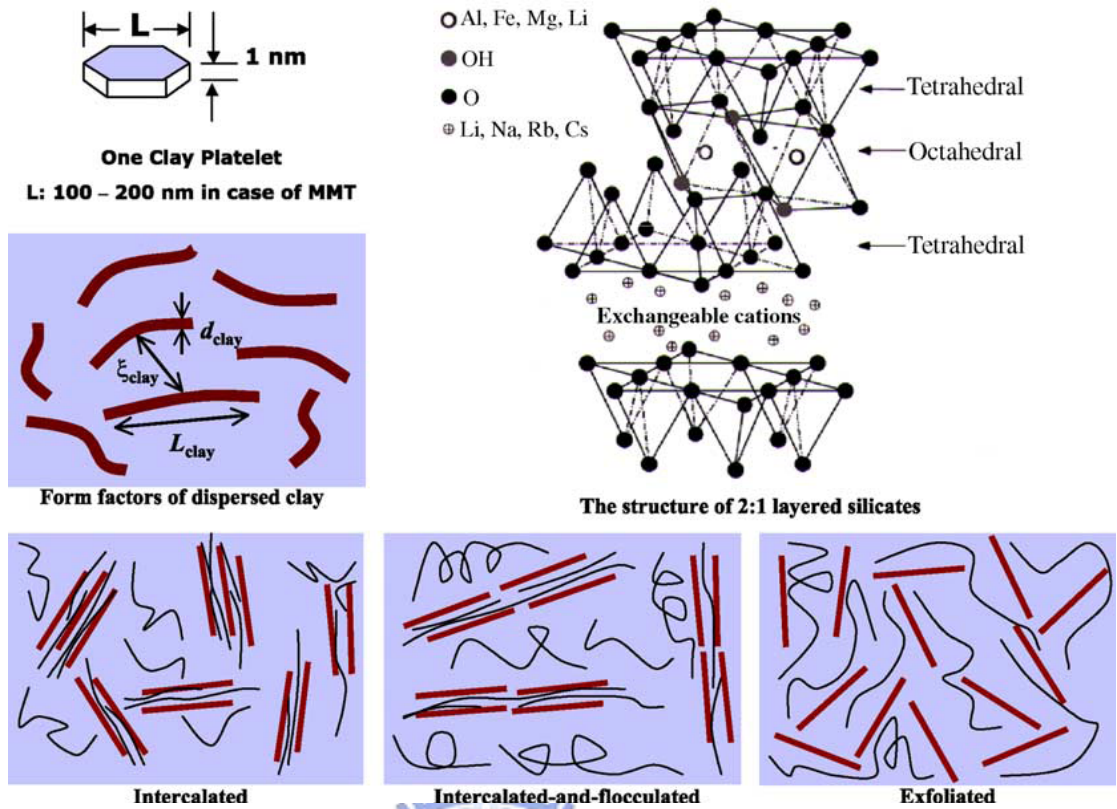


Figure 1-11. Schematically illustration of three different types of thermodynamically achievable polymer/layered silicate nanocomposites.

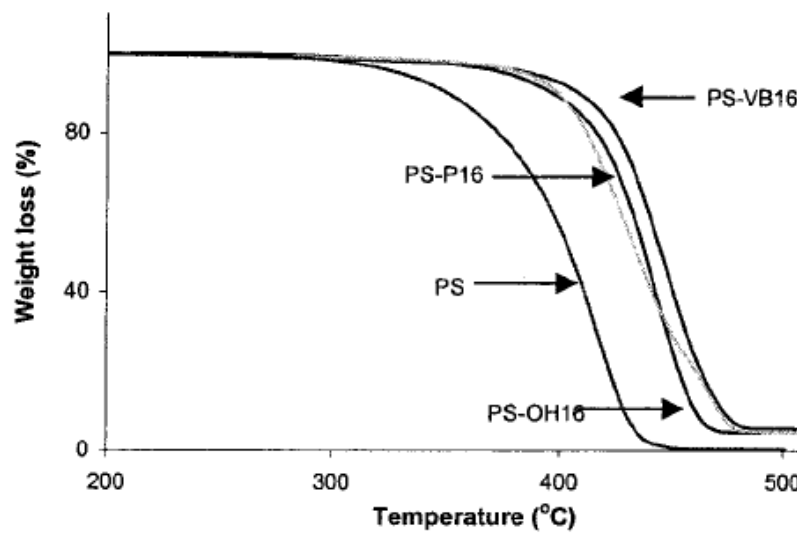


Figure 1-12. TGA curves for polystyrene, PS, and the nanocomposites. [37]

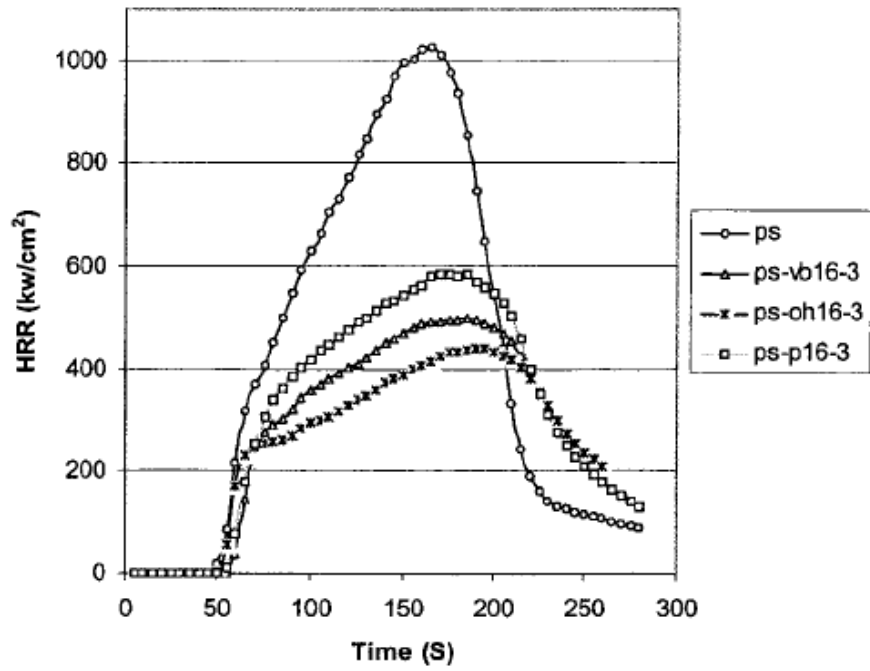


Figure 1-13. Peak heat release rates for polystyrene and the three nanocomposites.

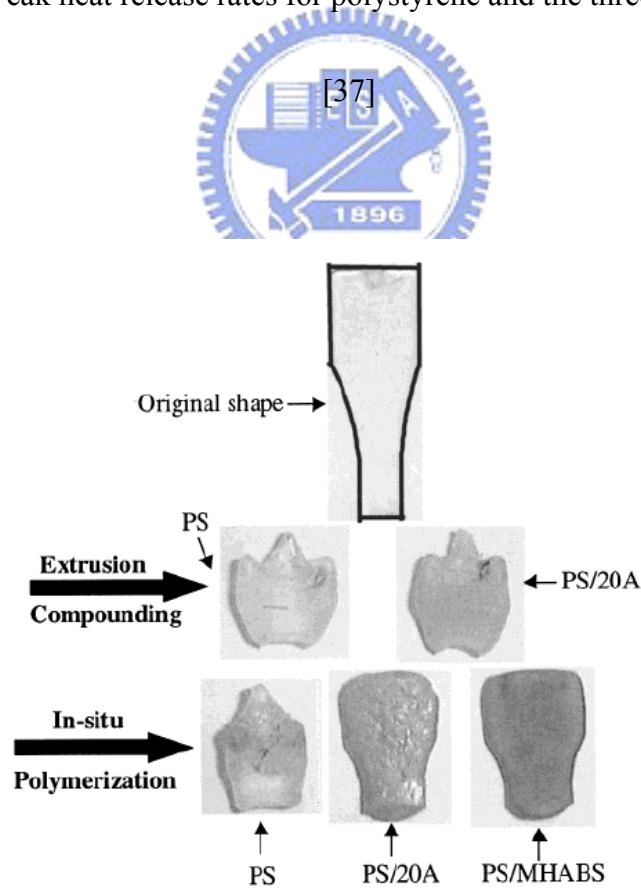


Figure 1-14. PS and PS/clay nanocomposites after dimension stability test. Clay loading

is 5 wt % for all nanocomposites. [38]

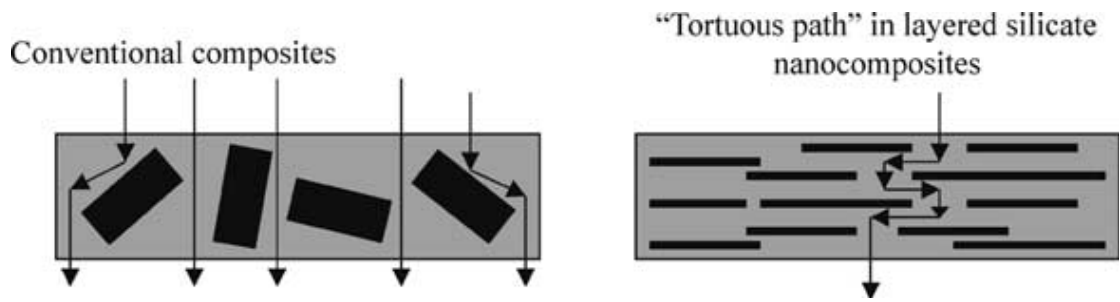


Figure 1-15. Formation of tortuous path in PLS nanocomposites.

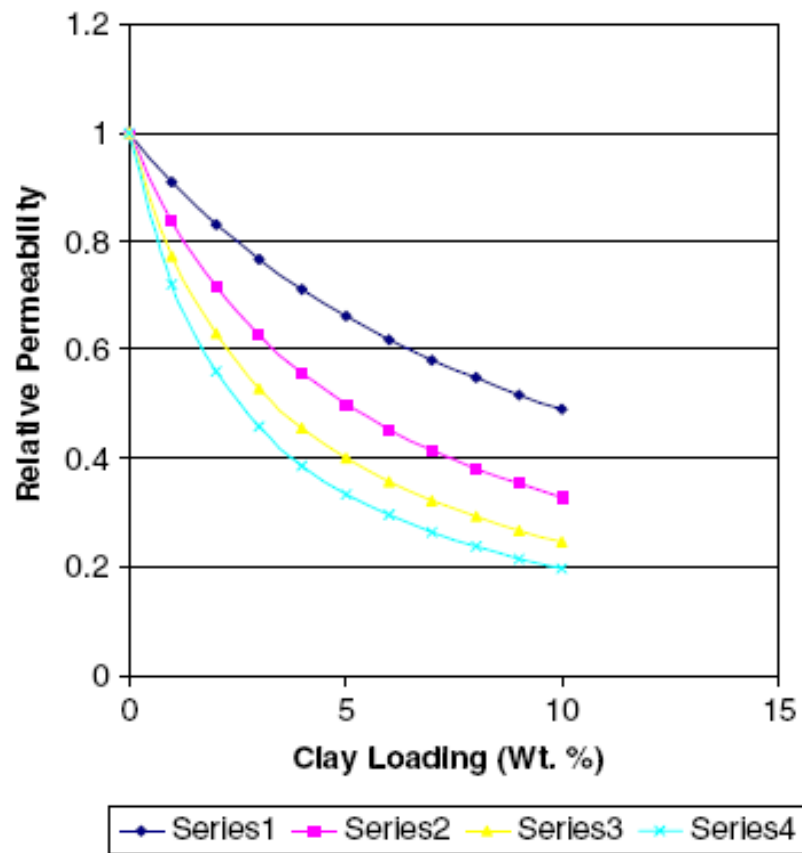


Figure 1-16. Relative gas permeability versus clay loading for polymer/clay nanocomposites per the model by Nielsen. The different curves represent aspect ratios of 50, 100, 150, and 200 for series 1–4 respectively.

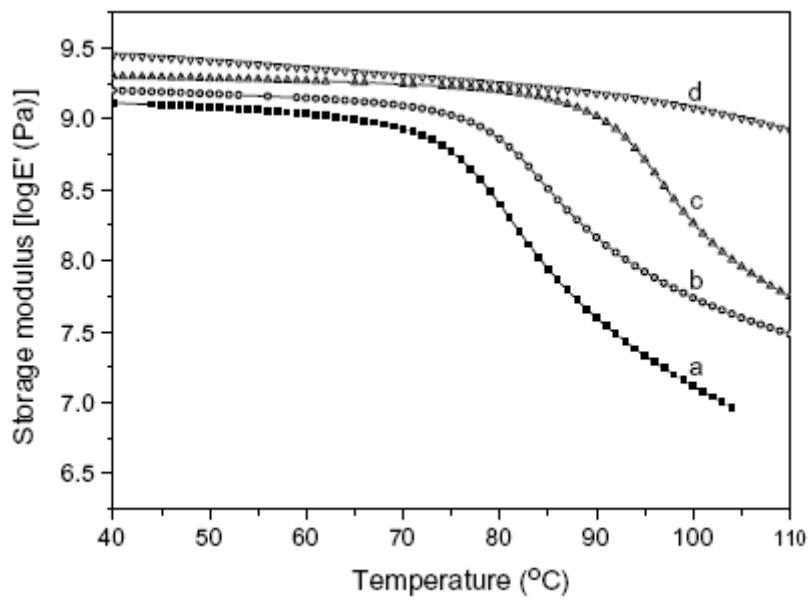


Figure 1-17. Storage modulus of (a) pure PS, (b) PS/MMT-1, (c) PS/MMT-2 and (d)

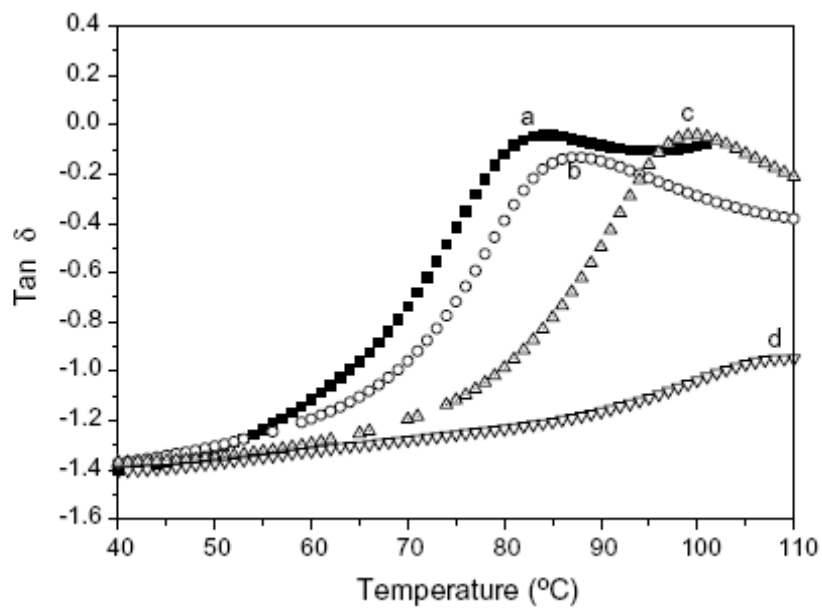


Figure 1-18. $\tan \delta$ values of (a) pure PS, (b) PS/MMT-1, (c) PS/MMT-2 and (d)

PS/MMT-3.

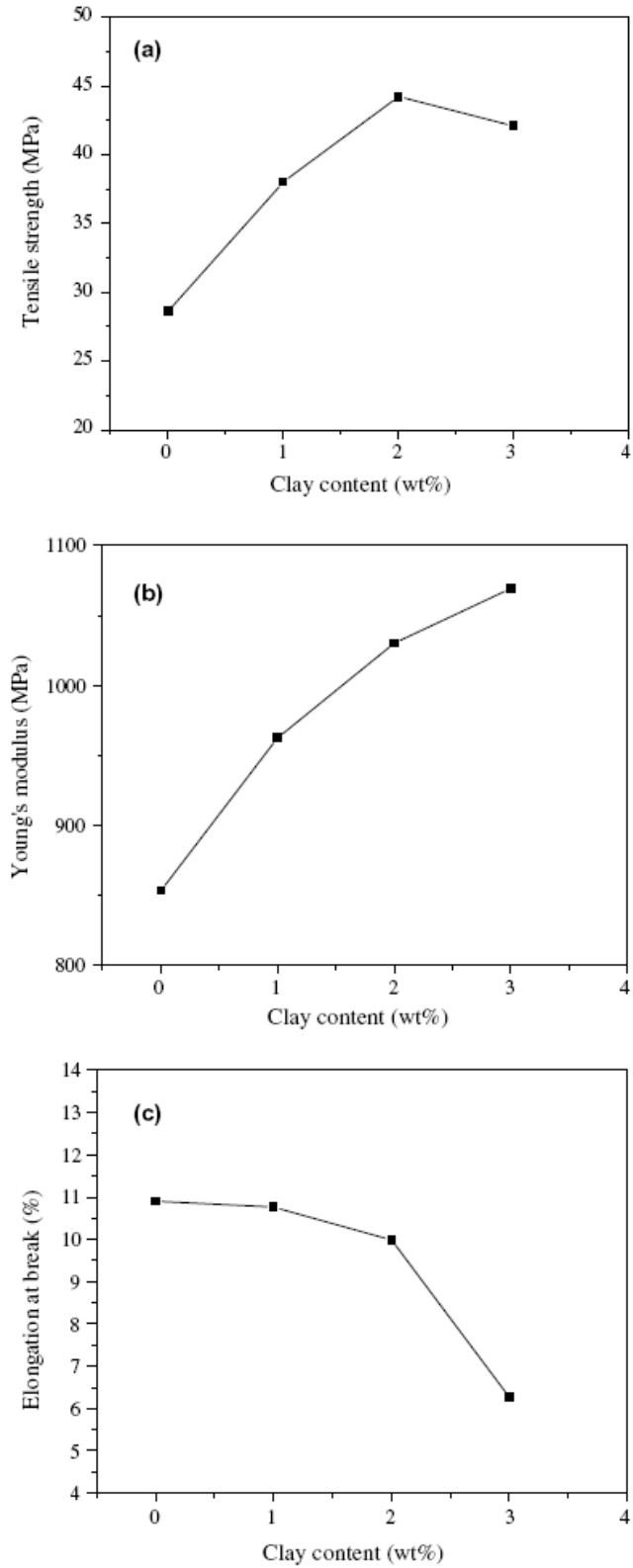


Figure 1-19. (a) Tensile strengths, (b) Young's modulus and (c) elongations at break of

PS/MMT nanocomposites. [49]

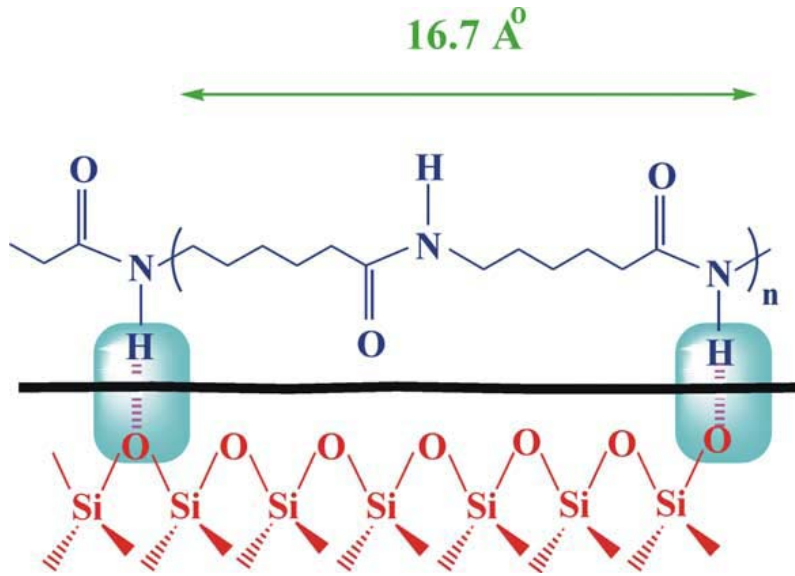


Figure 1-20. Schematic illustration of formation of hydrogen bonds in N6/MMT nanocomposite.

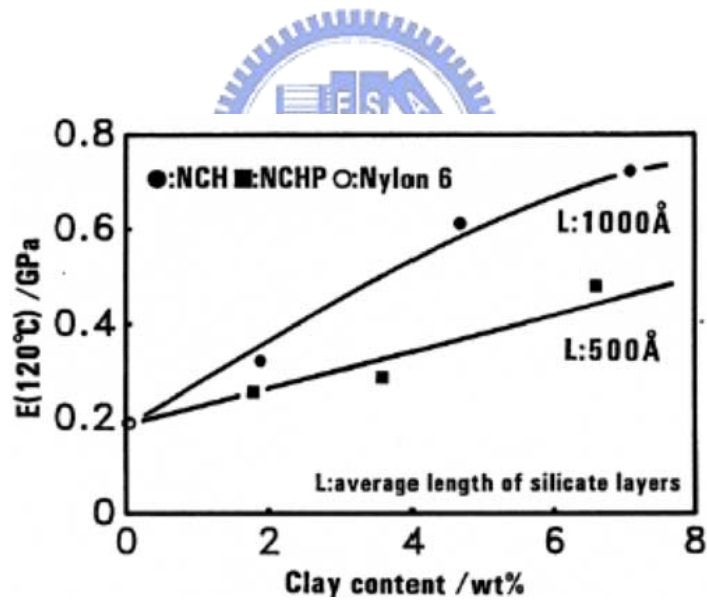


Figure 1-21. Effect of clay content on tensile modulus in case of N6/OMLS nanocomposites prepared via melt extrusion. [50]

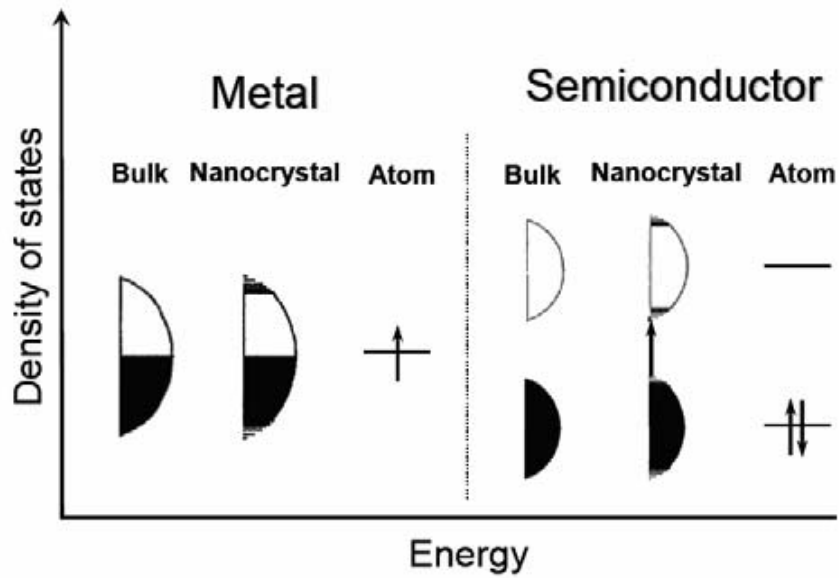


Figure 1-22. Schematic illustration of the density of states in metal and semiconductor clusters. [53]

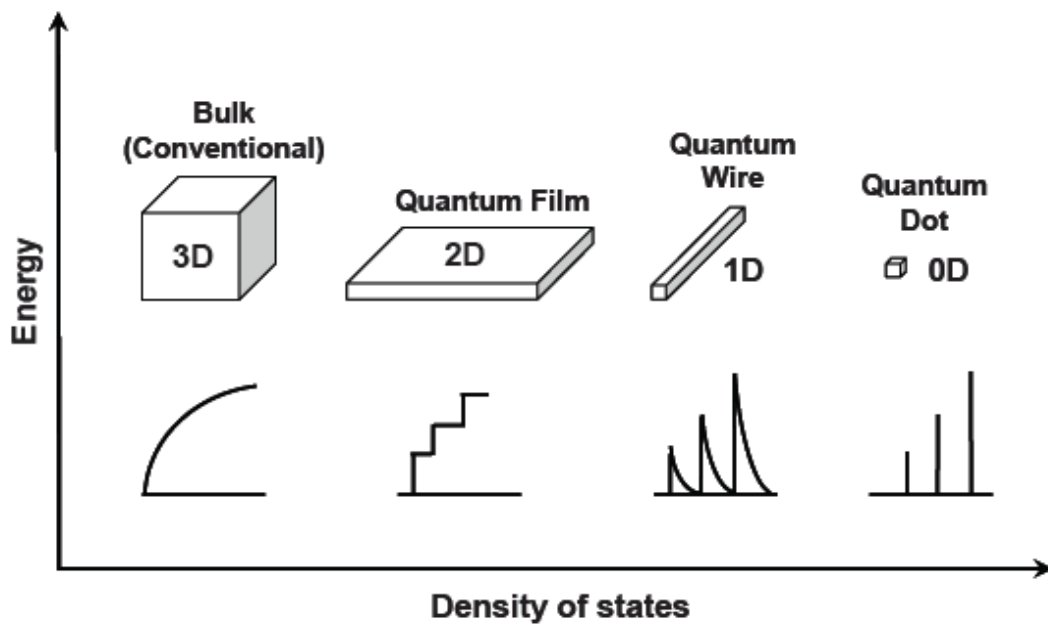
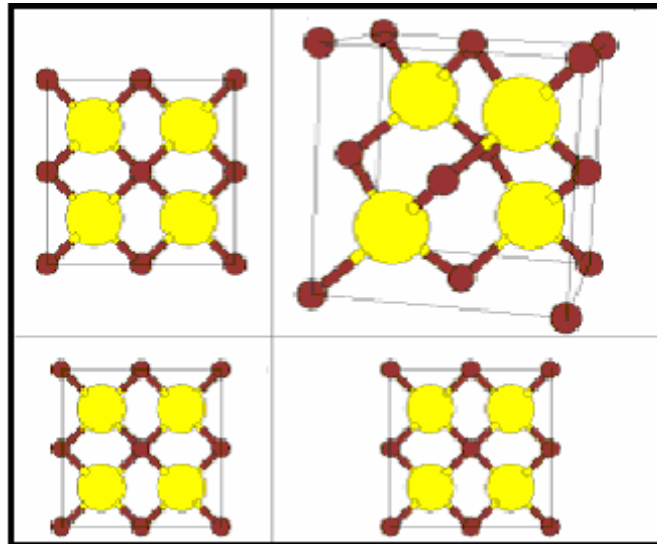
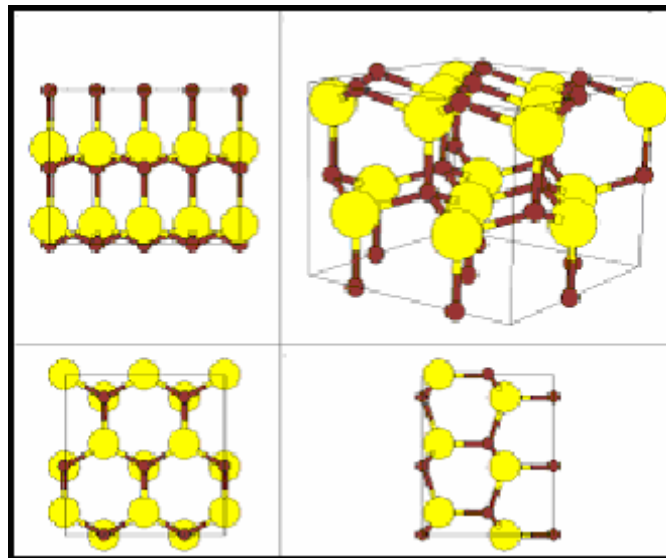


Figure 1-23. Idealized density of states for one band of a semiconductor structure of 3, 2, 1, and “0” dimensions. (In the 3d case the energy levels are continuous, while in the “0d” or molecular limit the levels are discrete) [56]



(a) The Zinc-blend Structure (Cubic ZnS or β -ZnS)



(b) The Wurtzite Structure (Hexagonal ZnS or α -ZnS)

Figure 1-24. Structures of the ZnS crystals (a) cubic phase and (b) hexagonal phase.

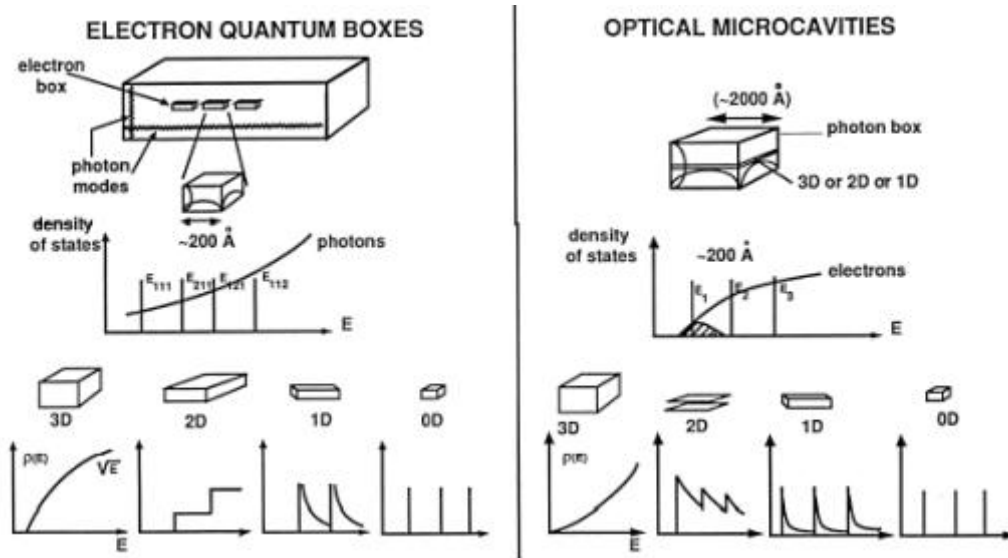


Figure 1-25. Quantum confinement effect of the electrons and the photons.

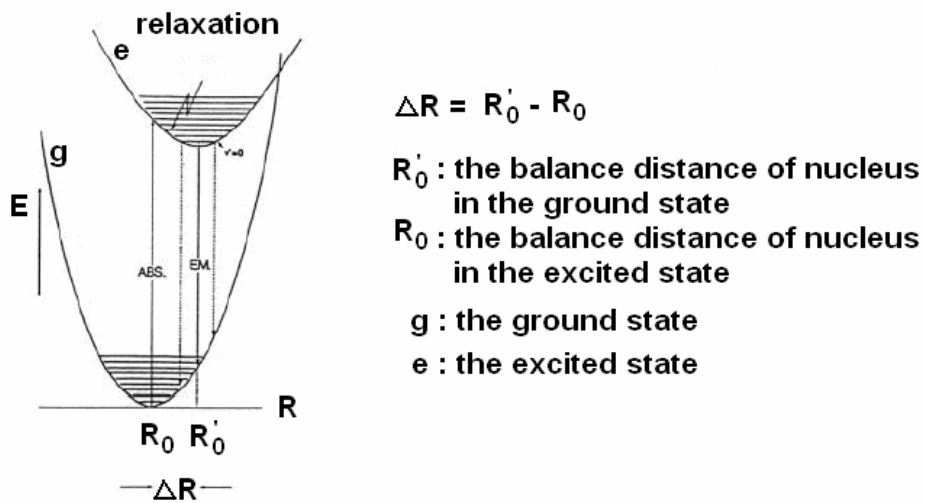


Figure 1-26. Configuration coordinate diagrams of the phosphor.

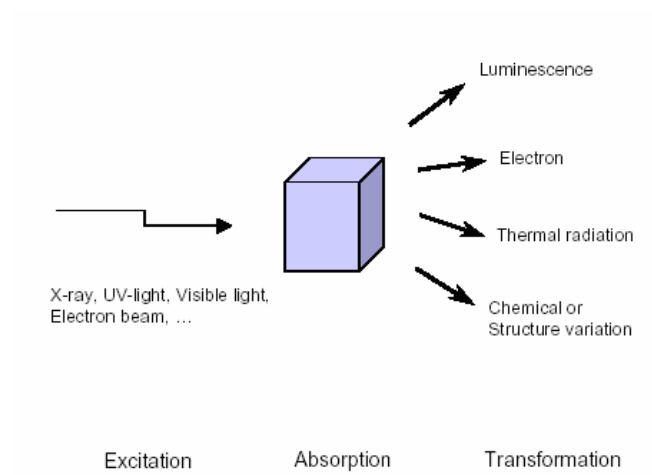


Figure 1-27. Energy transformation diagram of the excitation energy.



Excited State

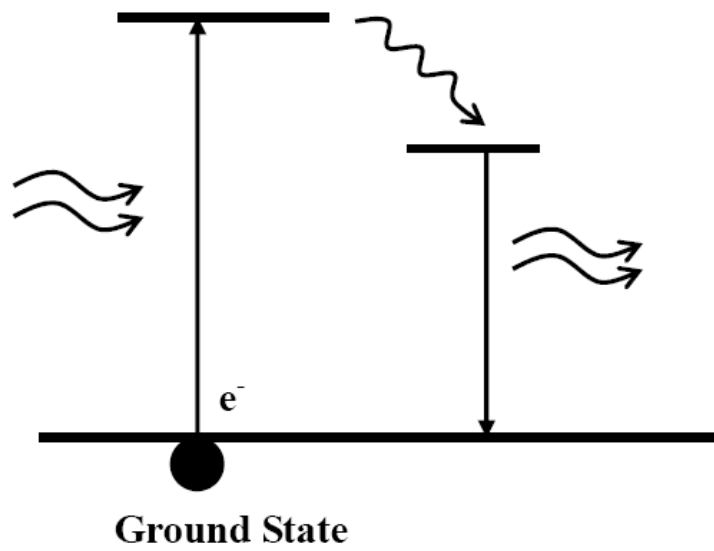


Figure 1-28. Progress of the relaxation.

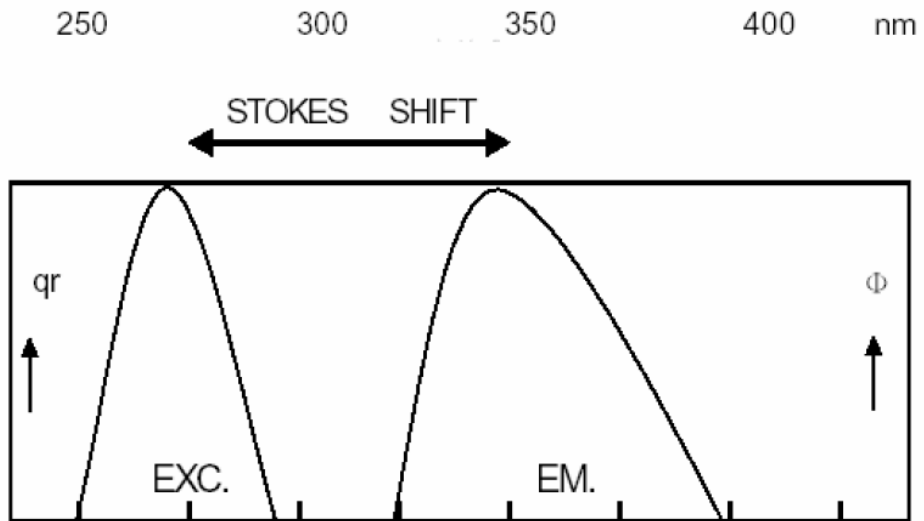


Figure 1-29. Diagram of the Stokes shift.

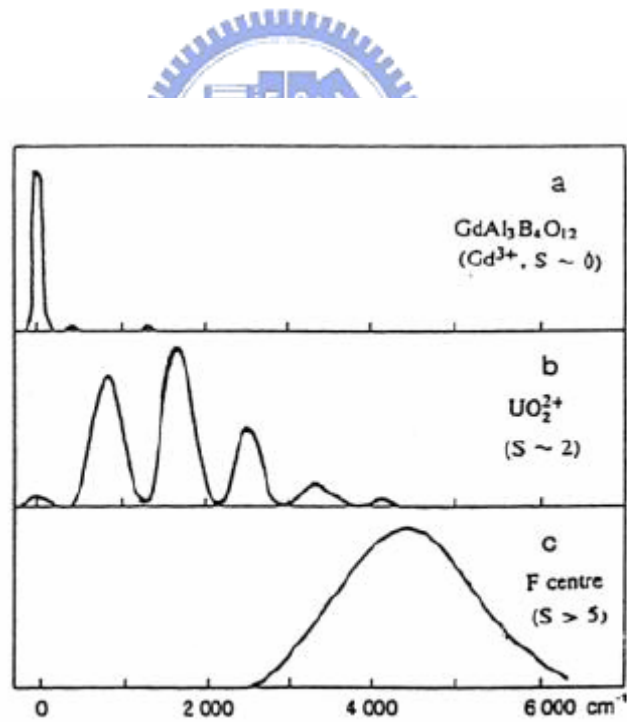


Figure 1-30. Influence of the different coupling effect on width of the emission peaks.

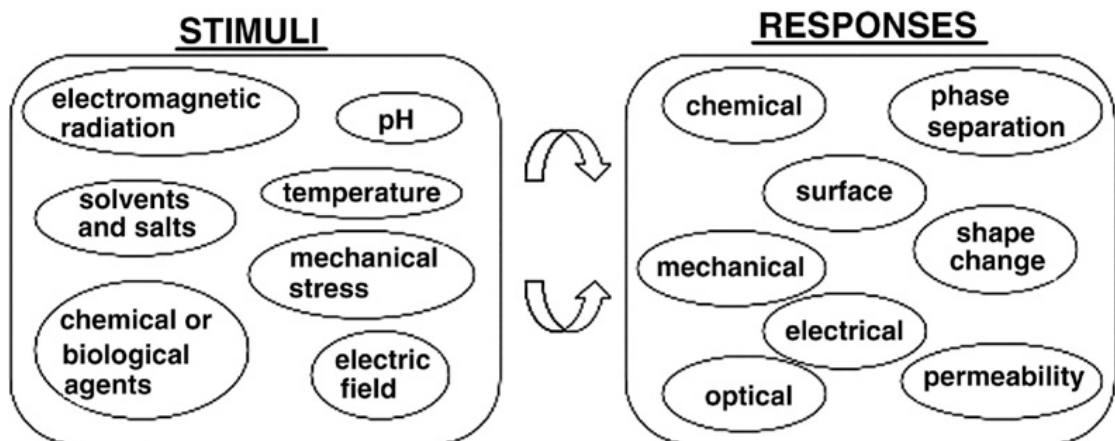


Figure 1-31. Potential stimuli and responses of synthetic polymers.

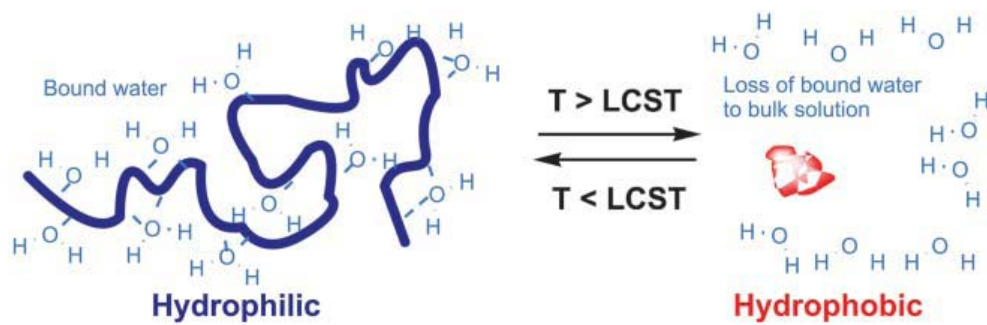


Figure 1-32. Schematic of 'smart' polymer response with temperature.

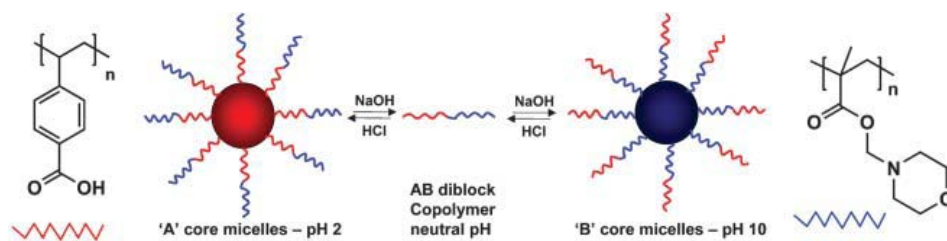


Figure 1-33. Control of micellar states dependent on pH.

Chapter 2

Studies on Thermal Properties of PS Nanocomposites for the Effect of Intercalated Agent with Side Groups

Abstract

Polystyrene layered silicate nanocomposites were prepared from three new organically modified clays by emulsion polymerization method. These nanocomposites were exfoliated up to 3 wt % content of pristine clay relative to the amount of polystyrene (PS). The intercalated agents, C₂₀, C₂₀-4VB, and C₂₀-POSS intercalated into the galleries result in improved compatibility between hydrophobic polymer and hydrophilic clay and facilitate the well dispersion of exfoliated clay in the polymer matrix. Results from X-ray diffraction, TEM and Fourier transform infrared spectroscopy indicate that these intercalated agents are indeed intercalated into the clay galleries successfully and these clay platelets are exfoliated in resultant nanocomposites. Thermal analyses of polystyrene-layered silicate nanocomposites compared with virgin PS indicate that the onset degradation temperature ca. 25 °C increased and the maximum reduction in coefficient of thermal expansion (CTE) is ca. 40 % for the C₂₀-POSS/clay nanocomposite. In addition, the glass transition temperatures of all these nanocomposites are higher than the virgin PS.

2.1 Introduction

Polystyrene (PS) is one of the most mass-productive and commercialized polymers. Recently, polystyrene (PS)/clay nanocomposites have been reported by several researchers [1-6]. Over the last decade, the use of organically modified montmorillonite as an additive has been intensively studied because of its improved thermal [7-10] and mechanical properties [11-16]. The most promising composite systems would be hybrids based on organic polymers and inorganic clay minerals consisting of silicate layers [15,17–29]. Polymer–clay nanocomposites were first synthesized by a Toyota research group [18–19]. They reported that individual layers (about one nm thickness) of clay particles are completely exfoliated in a continuous polymer matrix as revealed by X-ray diffraction (XRD) and transmission electron microscopy (TEM). The incorporation of organophilic clays, commonly montmorillonites (MMT), into polymers dramatically enhances its barrier, thermal and mechanical properties, since such nanofillers display a large surface for interactions with polymer matrix. During the past few years, great attention has been paid on silsesquioxane base nanocomposite. The POSS moiety is expected to act as a nano-scale filler to modify polymer matrix and results in nanocomposites with improved mechanical and thermal properties [30-32].

The chemical structure of montmorillonite consists of two fused silica tetrahedral sheets sandwiching an edge-shared octahedral sheet of either magnesium or aluminum hydroxide. The clay can be functionalized by various organic cations through ion exchange where the metal ions are replaced by organic cations intercalated the silicate layers. Its hydrophilic nature and ionic exchange capacity allow the silicate mineral to be intercalated by organic cations such as alkylammonium, to make the clay organophilic and compatible with polymers [33-34].

High homogeneity for the dispersion of clays in the matrix usually requires the intercalated agents to be highly compatible with silicate clay and polymer matrix.

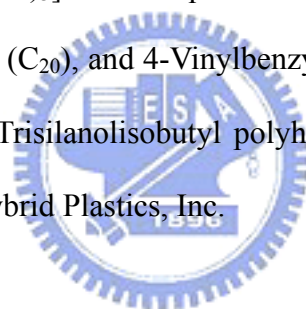
Several ways to make polymer-layered silicate nanocomposites have been demonstrated, including solution mixing, melt blending, and in situ polymerization [35-37]. In general, polymer-layered silicate nanocomposites can be divided into two categories. The intercalated polymer-layered silicate nanocomposites have layered clay dispersed in a polymer matrix with polymer chains inserted into clays layers but retain their lateral order. The exfoliated ones consist of fully delaminated clay platelets dispersed individually in polymer matrix. In general, the exfoliated structure is more effective in improving the properties of the polymer.

In this study, three PS nanocomposites were prepared by emulsion polymerization using C₂₀, C₂₀-4VB, and C₂₀-POSS-treated clays as shown in Scheme 2-1. The type of the nanocomposites produced was elucidated using X-ray diffraction and transmission electron microscopy. IR spectroscopic analysis confirmed the existence of the intercalated agents in the clay galleries. Properties of these polymer-clay nanocomposites were characterized by thermogravimetric analysis, differential scanning calorimeter, gel permeation chromatography, coefficient of thermal expansion, and mechanical properties.

2.2 Experimental

2.2.1. Materials

Sodium montmorillonite (Na^+ -MMT) with 1.45 mequiv/g cationic exchange capacity (CEC) was purchased from Nanocor Co. Most chemicals used in this study, including monomeric styrene, chemically pure acetone, methanol, tetrahydrofuran, acetonitrile, potassium hydroxide (KOH), triethylamine, and trichloro[4-(chloromethyl)phenyl] silane were acquired from the Aldrich Chemical Co., Inc. The styrene monomer was purified by removing the inhibitor with the aid of an inhibitor-removal column. Sodium dodecyl sulfate (SDS) and hydrochloric acid were both obtained from Curtin Matheson Scientific, Inc. Potassium persulfate ($\text{K}_2\text{S}_2\text{O}_8$) and aluminum sulfate [$\text{Al}_2(\text{SO}_4)_3$] were acquired from Fisher Scientific Co., USA. N,N-Dimethyloctadecylamine (C_{20}), and 4-Vinylbenzyl chloride (4VB) were obtained from Acros Organics, USA. Trisilanolisobutyl polyhedral oligomeric silsesquioxane (POSS) was obtained from Hybrid Plastics, Inc.



2.2.2. Preparation of POSS-Cl compound.

The corner-capping reaction was employed to prepare POSS-Cl compound as shown in Scheme 2-2. Trisilanolisobutyl polyhedral oligomeric silsesquioxane (**1**, 3 g) and Et_3N (1.26 g) were added into a 100 mL two-neck round bottom flask and stirred continuously 3 h under nitrogen, then 20 mL THF was added into the flask at 0 °C for 1 h. After stirring at 0 °C under nitrogen, triethylamine and trichloro[4-(chloromethyl)phenyl]silane (**2**, 1.28 g) in THF (10 mL) were added dropwisely into the solution and stirred at 0 °C. The cooling bath was removed and stirring continuously for additional 7.5 h under nitrogen. The POSS type compound and $\text{HNEt}_3\text{-Cl}$ byproduct were separated by filtration. The clear THF solution was

dropped into a beaker of acetonitrile and rapidly stirred. The resulting product (**3**) was collected and dried in a vacuum oven for 24 h. ^1H NMR (CDCl_3), δ : 7.59 (d, 2H), 7.33 (d, 2H), 4.52 (s, 2H), 1.92-1.62 (m, 7H), 1.09-0.85 (m, 42H), 0.75-0.48 (m, 14H).

2.2.3. Preparation of C_{20} -4VB intercalated agent.

The intercalated agent of C_{20} -4VB was prepared according to the pathway shown in Scheme 2-3(a). N,N-dimethyloctadecylamine (C_{20} , 4.2 mL) and 4-vinylbenzyl chloride (4VB, 1.87 g) in acetone (10 mL) were refluxed at 60 °C under nitrogen for 5 h. After cooling, the mixture was washed with cold acetone and the volatiles were removed in vacuum oven for 24h at 65 °C. ^1H NMR (CDCl_3), δ : 7.56 (d, 2H), 7.38 (d, 2H), 6.65 (q, 1H), 5.75 (d, 1H), 5.31 (d, 1H), 4.96 (s, 2H), 3.39 (t, 2H), 3.23 (s, 6H), 1.72 (m, 2H), 1.23 (m, 30H), 0.82 (t, 3H).

2.2.4. Preparation of C_{20} -POSS intercalated agent.

The intercalated agent of C_{20} -POSS was prepared according to the pathway shown in Scheme 2-3(b). N,N-dimethyloctadecylamine (C_{20} , 1.49 g), POSS-Cl compound (5.68 g) in acetone (15 mL) was refluxed at 60 °C under nitrogen for 24 h. After cooling, the mixture was evaporated by a rotatory evaporator and then added Et_2O (20 mL). The solution was extracted with deionized water three times (150 mL \times 3). The organic phase was dried with MgSO_4 and evaporated by a rotatory evaporator to obtain the C_{20} -POSS intercalated agent. ^1H NMR (CDCl_3), δ : 7.68 (d, 2H), 7.58 (d, 2H), 5.03 (s, 2H), 3.42 (t, 2H), 3.30 (s, 6H), 1.81 (m, 7H), 1.41 (m, 2H), 1.26 (m, 30H), 0.90 (m, 42H), 0.82 (t, 3H), 0.59 (m, 14H).

2.2.5. Preparation of C_{20} -, C_{20} -4VB, and C_{20} -POSS modified clays.

Na⁺ MMT (0.3 g) was dispersed in 1L deionized water at 80°C and stirred continuously for 4 h. C₂₀ (0.18 g), C₂₀-4VB (0.22 g) or C₂₀-POSS (0.63 g) in water (5 mL) was placed into another flask, 10 % hydrochloric acid (1 mL) and ethanol (5 mL) were added and then stirred at 80 °C for 1 h. This intercalating agent solution was then poured into the clay suspension solution and stirred vigorously at 80 °C for 4h. The white precipitate was filtered to remove water and washed thoroughly with warm water until no chloride could be detected by an aqueous AgNO₃ solution, and then dried overnight in a vacuum oven at room temperature.

2.2.6. Preparation of polystyrene/clay nanocomposites.

Desired amounts of organic modified clay, KOH, SDS and styrene monomer were added in a two-neck round bottom flask equipped with a stirring bar. The mixture was heated to 80 °C and stirred under N₂, desired quantity of K₂S₂O₈ was added slowly to the mixture. Polymerization was carried out at 80 °C for 8 h and then cooled to room temperature. 2.5 % aqueous aluminum sulfate (10 mL) was added into the polymerized emulsion, followed by adding dilute hydrochloric acid (10 mL) with stirring. Finally, acetone was added to break down the emulsion completely, and the polymer product was washed several times with methanol and distilled water and then dried in a vacuum oven at 80 °C for 24h. Similar procedures were employed to prepare virgin polystyrene.

2.2.7. Instrumentations

Wide-angle X-Ray diffraction (WAXD) spectrum was recorded on powdered sample using a Rigaku D/max-2500 type X-ray diffraction instrument. The radiation source used was Ni-filtered, Cu K α radiation ($\lambda=1.54\text{\AA}$). The sample was mounted on

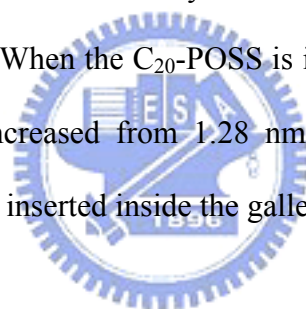
a circular sample holder, the scanning rate was $0.6^\circ/\text{min}$ from $2\theta = 1$ to 20 . A Hitachi H-7500 transmission electron microscopy (100 kV) was used to examine clay morphology and orientation. The sample was ultramicrotomed at room temperature using a diamond knife using a Leica Ultracut UCT Microtome to give 70 nm-thick sections. Thermogravimetric analysis (TGA) was performed on a TA Instruments Q50 apparatus. The sample (5-10)mg was placed in a Pt cell at a scan rate of $20^\circ\text{C}/\text{min}$ from 30 to 800°C under nitrogen. The calorimetric measurement was performed use a TA Instruments Differential Scanning Calorimeter (DSC-2010) to measure the glass transition temperature (T_g). The sample was preheated at a scan rate of $20^\circ\text{C}/\text{min}$ from 30 to 150°C . In DSC measurement of the sample was cooled to 10°C quickly from the melt of the first scan and the second scan rate was $20^\circ\text{C}/\text{min}$ from 30 to 150°C . The T_g value was taken as the midpoint of the heat capacity transition between the upper and lower points of deviation from the extrapolated liquid and glass lines. Molecular weights and molecular weight distributions were determined by gel permeation chromatography (GPC) using a Waters 510 HPLC equipped with a 410 Differential Refractometer, a refractive index (UV) detector, and three Ultrastyrigel columns (100, 500, and 10^3 \AA) connected in series in order of increasing pore size. The molecular weight calibration curve was obtained using polystyrene standards. ^1H NMR spectroscopic analyses were performed using a Varian Uniytinova-500 NMR Spectrometers at 500 MHz. All spectra were recorded using CDCl_3 as the solvent and TMS as the external standard. Coefficient of thermal expansion was obtained using a TA 2940 Thermomechanical Analyzer (TMA). The force applied was 0.005 N and it was heated at rated of $5^\circ\text{C}/\text{min}$ from 25 to 150°C .

2.3. Results and discussion

Structures of intercalated agents used to modify the clays are shown in Scheme 2-1.

2.3.1. Characterizations of C_{20} -, C_{20} -4VB, and C_{20} -POSS modified clays.

Figure 2-1 shows the XRD curves for the starting and modified clays. The d spacing indicates the interlayer spacing of the silicate layers calculated from the peak position using the Bragg equation. The original clay with an intergallery spacing of 1.28 nm ($2\theta = 6.92^\circ$), increases to 3.95 nm for C_{20} ($2\theta = 2.23^\circ$), 3.33 nm for C_{20} -4VB ($2\theta = 2.66^\circ$), and 3.80 nm for C_{20} -POSS ($2\theta = 2.33^\circ$), respectively. The results indicate that these intercalated agents are successfully intercalated into the gallery and results are summarized in Table 2-1. When the C_{20} -POSS is inserted between the galleries of the clay, the d spacing is increased from 1.28 nm for original clay to 3.80 nm, implying that the C_{20} -POSS is inserted inside the gallery of the silicate.



2.3.2. Characterizations of polystyrene/clay Nanocomposites.

Figure 2-2 shows X-ray diffraction patterns of C_{20} /clay/PS, C_{20} -4VB/clay/PS, and C_{20} -POSS/clay/PS nanocomposites. Essentially no peak can be detected for all nanocomposites from C_{20} , C_{20} -4VB, and C_{20} -POSS modified clays, implying that they all have exfoliated structure. XRD alone may lead to false result in terms of the extent of exfoliation. As a result, TEM observations are necessary to further verify the extent of delamination and exfoliation. Either intercalated or exfoliated nanocomposite can be distinguished on the bases of transmission electron microscopy (TEM). TEM images of C_{20} /clay/PS, C_{20} -4VB/clay/PS and C_{20} -POSS/clay/PS are shown in Figure 2-3. In Figure 2-3(b), C_{20} -4VB/clay/PS shows full dispersion and exfoliation of the

clay platelets within the PS matrix because the intercalated agent of C₂₀-4VB containing a vinylbenzyl group allows for styrene polymerization taking place within the clay gallery. In Figure 2-3(a), these clay platelets of the C₂₀/clay modified nanocomposite are mainly exfoliated, but in some regions they are aggregated and intercalated. In Figure 2-3(c), the image shows mainly the exfoliated structures for the C₂₀-POSS modified nanocomposite.

2.3.3. Glass transition temperatures.

Figure 2-4 and Table 2-2 show that the pure PS exhibits a heat flow change at approximately 100 °C, corresponding to the T_g of PS. All DSC thermograms display single glass transition temperature in the experimental temperature range. C₂₀/clay-, C₂₀-4VB/clay-, and C₂₀-POSS/clay- modified nanocomposites all show slightly higher T_g compared to the pure PS.



2.3.4. Molecular weights of the nanocomposites.

Table 2-3 shows the molecular weight and polydispersities of the PS and PS/silicate nanocomposites through emulsion polymerization. The sample for the molecular weights determination was filtered to remove all clay content before measurement and the results are shown in Table 2-3. From the table, M_n (or M_w) of the PS in PS/clay nanocomposites is higher, suggesting that clay may either act as a catalytic agent, resulting in a higher molecular weight of the PS with proceeding polymerization.

2.3.5 TGA analyses.

Figure 2-5 and Figure 2-6 present the thermal stabilities of the C₂₀-, C₂₀-4VB-,

and C₂₀-POSS- modified clays and corresponding nanocomposites measured under nitrogen gas. Generally, the incorporation of clay into the polymer matrix is able to enhance thermal stability by acting as a superior insulator and mass transport barrier to the volatile products generated during decomposition. Figure 2-5 shows TGA traces for these intercalated clays. The C₂₀-POSS/Clay decomposes at a higher temperature of 262 °C while C₂₀/Clay and C₂₀-4VB/Clay decompose at 189 and 243 °C, indicating the C₂₀-POSS is thermally more stable than the C₂₀ and C₂₀-4VB. Thereby, the clay intercalated with C₂₀-POSS has better thermal stability relative to those intercalated with C₂₀ and C₂₀-4VB.

All surfactant-modified nanocomposites show better thermal stability than the virgin PS as shown in Figure 2-6. The decomposition temperatures for 5% weight loss of C₂₀-, C₂₀-4VB, and C₂₀-POSS- modified nanocomposites are 15, 12, and 25 °C higher than the virgin PS. This observed enhancement in the thermal properties is due to the presence of the clay to act as barriers to minimize the permeability of volatile degradation products out from the material. The values of 5 and 50% weight loss temperatures and the corresponding char yields are summarized in Table 2-1.

2.3.6 Coefficient of thermal expansion.

Dimensional stability is critical in many applications, poor dimensional stability can cause warping or other changes in shape. Polymer/clay nanocomposites provide improvements both on thermal and dimensional stabilities. As shown in Figure 2-7 and Table 2-1, the CTE of the virgin PS is 164 μm/m °C while the CTEs for C₂₀/clay/PS, C₂₀-4VB/clay/PS, and C₂₀-POSS/clay/PS are 120, 134, and 100 μm/m °C, respectively. The maximum reduction in coefficient of thermal expansion is from the C₂₀-POSS/clay/PS, 39 % lower than the virgin PS.

The obtained lower CTE from these composites can be attributed to the particle rigidity and fine dispersion of the clay platelets in the PS matrix. The incorporation of the modified clay can reduce CTE and provides products with good dimensional stability.



2.4. Conclusions

In this paper, we have employed the novelty of the preparation of the C₂₀-POSS and C₂₀-4VB containing intercalated agents. Syntheses of exfoliated nanocomposites via emulsion polymerization of styrene in the presence of 3 wt % clay containing the C₂₀, C₂₀-4VB, and C₂₀-POSS intercalated agents, were prepared respectively. XRD results show that d spacing increases from 1.28 nm to 3.95, 3.33, and 3.80 nm after intercalation. The C₂₀-4VB containing vinyl benzyl group results in more effective in promoting fully exfoliated structure in polystyrene matrix. All modified clay nanocomposites result in higher T_g and higher thermal degradation temperature than the virgin PS, especially for the C₂₀-POSS/clay nanocomposite resulting in 25 °C increase in the thermal degradation temperature. These well distributed clay platelets tend to retard the segmental movement of PS and result in reduced CTE. The incorporation of the 3 wt% clay leads to improvements in thermal stability, slight increase in glass transition temperature, and decrease in coefficient of thermal expansion.

Acknowledgments

The authors thank the National Science Council, Taiwan, for financially supporting this research under Contract NSC-95-2221-E-009-118 and NSC-96-2120-M-009-009

References

- [1] Vaia, R. A.; Ishii, H.; Giannelis, E. P. *Chem. Mater.* **1993**, 5, 1694.
- [2] Chen, G.; Liu, S.; Chen, S.; Qi, Z. *Macromol. Chem. Phys.* **2001**, 202, 1189.
- [3] Chen, G.; Liu, S.; Zhang, S.; Qi, Z. *Macromol. Rapid Commun.* **2000**, 21, 746.
- [4] Chen, G.; Ma, Y.; Qi, Z. *J. Appl. Polym. Sci.* **2000**, 77, 2201.
- [5] Chen, G.; Qi, Z. *J. Mater. Res.* **2000**, 15, 351.
- [6] Kurian, M.; Dasgupta, A.; Galvin, M. E.; Ziegler, C. R.; Beyer, F. L. *Macromolecules* **2006**, 39, 1864.
- [7] Gilman, J. W. *Appl. Clay Sci.* **1999**, 15, 31.
- [8] Ogata, N.; Kawakage, S.; Ogihara, T. *Polymer* **1997**, 38, 5115.
- [9] Langat, J.; Bellayer, S.; Hudrlik, P.; Hudrlik, A.; Maupin, PH.; Gilman, J. W.; Raghavan, D. *Polymer* **2006**, 47, 6698.
- [10] Fina, A.; Tabuani, D.; Frache, A.; Camino, G. *Polymer* **2005**, 47, 7855.
- [11] Kawasumi, M.; Hasegawa, N.; Kato, M.; Usuki, A.; Okada, A. *Macromolecules* **1997**, 30, 6333.
- [12] Hasegawa, N.; Okamoto, H.; Kawasumi, M.; Usuki, A. *J. Appl. Polym. Sci.* **1999**, 74, 3359.
- [13] Fu, X.; Qutubuddin, S. *Polymer* **2001**, 42, 807.
- [14] Lan, T.; Kaviratna, P. D.; Pinnavaia, T. J. *J. Phys. Chem. Solids* **1996**, 57, 1005.
- [15] Lan, T.; Pinnavaia, T. J.; *Chem. Mater.* **1994**, 6, 2216.
- [16] Biswas, M.; Ray, S. S. *Adv. Polym. Sci.* **2001**, 155, 167.
- [17] Vaia, R. A.; Jandt, K. D.; Karamer, E. J.; Giannelis, E. P. *Macromolecules* **1995**, 28, 8080.
- [18] Usuki, A.; Kojima, Y.; Kawasumi, M.; Fukushima, Y.; Okada, A.; Fukushima, Y.; Kurauchi, T.; Kamigaito, O. *J. Mater. Res.* **1993**, 8, 1179.

- [19] Kojima, Y.; Usuki, A.; Kawasumi, M.; Okada, A.; Fukushima, Y.; Kurauchi, T.; Kamigaito, O. *J. Mater. Res.* **1993**, *8*, 1185.
- [20] Yano, K.; Usuki, A.; Okada, A.; Kurauchi, T.; Kamigaito, O. *J. Polym. Sci. Part A: Polym. Chem.* **1993**, *31*, 2493.
- [21] Wang, M. S.; Pinnavaia, T. J. *Chem. Mater.* **1994**, *6*, 468.
- [22] Messersmith, P. B.; Giannelis, E. P. *J. Polym. Sci. Part A: Polym. Chem.* **1995**, *33*, 1047.
- [23] Usuki, A.; Kato, M.; Okada, A.; Kurauchi, T. *J. Appl. Polym. Sci.* **1997**, *63*, 137.
- [24] Kato, M.; Usuki, A.; Okada, A. *J. Appl. Polym. Sci.* **1997**, *66*, 1781.
- [25] Kawasumi, M.; Hasegawa, N.; Kato, M.; Usuki, A.; Okada, A. *Macromolecules* **1997**, *30*, 6333.
- [26] Hasegawa, N.; Kawasumi, M.; Kato, M.; Usuki, A.; Okada, A. *J. Appl. Polym. Sci.* **1998**, *67*, 87.
- [27] Moet, A. *Mater. Lett.* **1993**, *18*, 97.
- [28] Vaia, R. A.; Ishii, H.; Giannelis, E. P. *Chem. Mater.* **1993**, *5*, 1694.
- [29] Ray, S. S.; Okamoto, M. *Prog. Polym. Sci.* **2003**, *28*, 1539.
- [30] Usuki, A.; Hasegawa, N.; Kato, M. *Adv. Polym. Sci.* **2005**, *135*, 179.
- [31] Song, X. Y.; Geng, H. P.; Li, Q. F. *Polymer* **2006**, *47*, 3049.
- [32] Liu, Y.; Zheng, S.; Nie, K. *Polymer* **2005**, *46*, 12016.
- [33] Huang, X.; Brittain, W. J. *Macromolecules* **2001**, *34*, 3255.
- [34] Beyer, F. L.; Beck Tan, N. C.; Dasgupta, A.; Galvin, M. E. *Chem. Mater.* **2002**, *14*, 2983.
- [35] Vaia, R. A.; Vasudevin, S.; Krawiec, W.; Scanlon, L. G.; Giannelis, E. P. *Adv. Mater.* **1995**, *7*, 154.
- [36] Giannelis, E. P. *Adv. Mater.* **1996**, *8*, 29.

[37] Gilman, J. W.; Morgan, A. B.; Harris, R. H.; Trulove, P. C.; DeLong, H. C.; Sutto, T. E. *Polym. Mater. Sci. Eng.* 2000, 83, 59.



Table 2-1. Basal spacing and organic fraction of the OMMT.
Sample (001) Basal spacing(nm) Organic fraction (%)^a

Clay	1.28	-
C ₂₀ /Clay	3.95	53.3
C ₂₀ -4VB/Clay	3.33	47.3
C ₂₀ -POSS/Clay	3.80	37.5

^a organic fraction was based on TGA analyses.

Table 2-2. Results of thermal and mechanical properties of polystyrene and polystyrene nanocomposites.

Sample	T _g (°C) ^a	T _{0.05} (°C) ^b	T _{0.5} (°C) ^c	Char at 600 °C ^d (%)	CTE (μm/m °C)
PS	100	390	424	0	164
C ₂₀ /Clay/PS	107	405	456	1.59/1.4	120
C ₂₀ -4VB/Clay/PS	108	402	454	1.59/1.59	134
C ₂₀ -POSS/Clay/PS	105	415	457	1.98/2.4	100

^a Glass transition temperature(T_g).

^b 5% Degradation temperature(T_{0.05}).

^c 50% Degradation temperature(T_{0.5}).

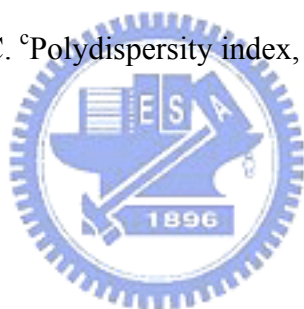
^d Char at 600(°C)% (expected %/experiment %)

Table 2-3. Molecular weights of polystyrene and polystyrene nanocomposites.

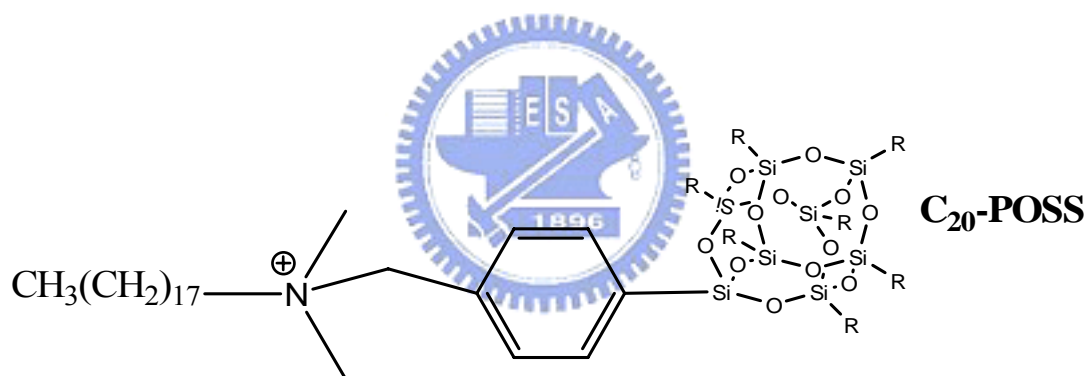
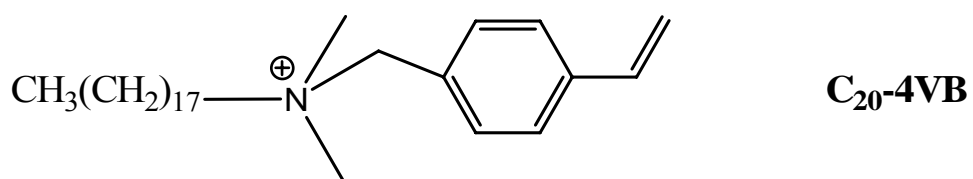
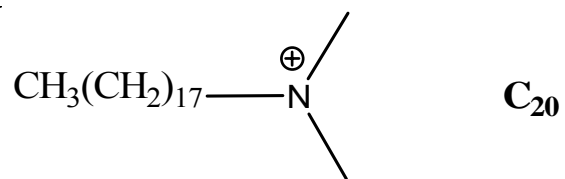
Sample	$M_n(\times 10^4)^a$	$M_w(\times 10^4)^b$	PDI(M_w/M_n) ^c
PS	34.5	53.1	1.54
C ₂₀ /Clay/PS	47.5	58.6	1.23
C ₂₀ -4VB/Clay/PS	45.2	57.4	1.27
C ₂₀ -POSS/Clay/PS	47.7	58.7	1.23

^aNumber-average molecular weights (M_n) and ^bweight-average molecular weights

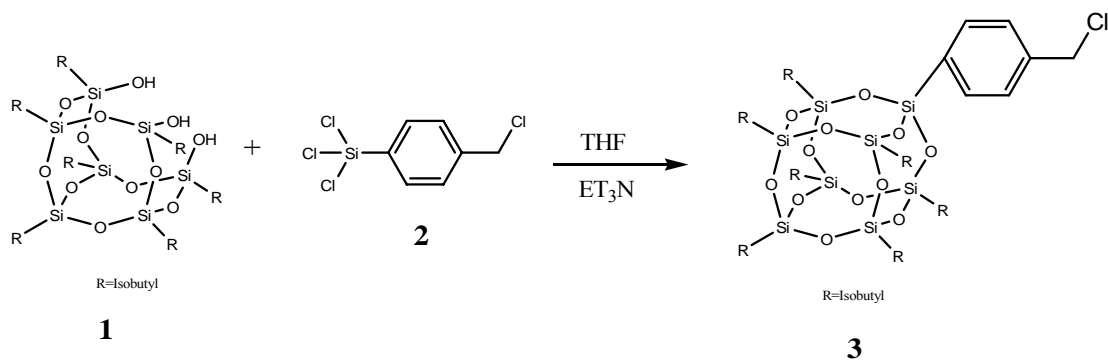
(M_w) were determined by GPC. ^cPolydispersity index, M_w/M_n .



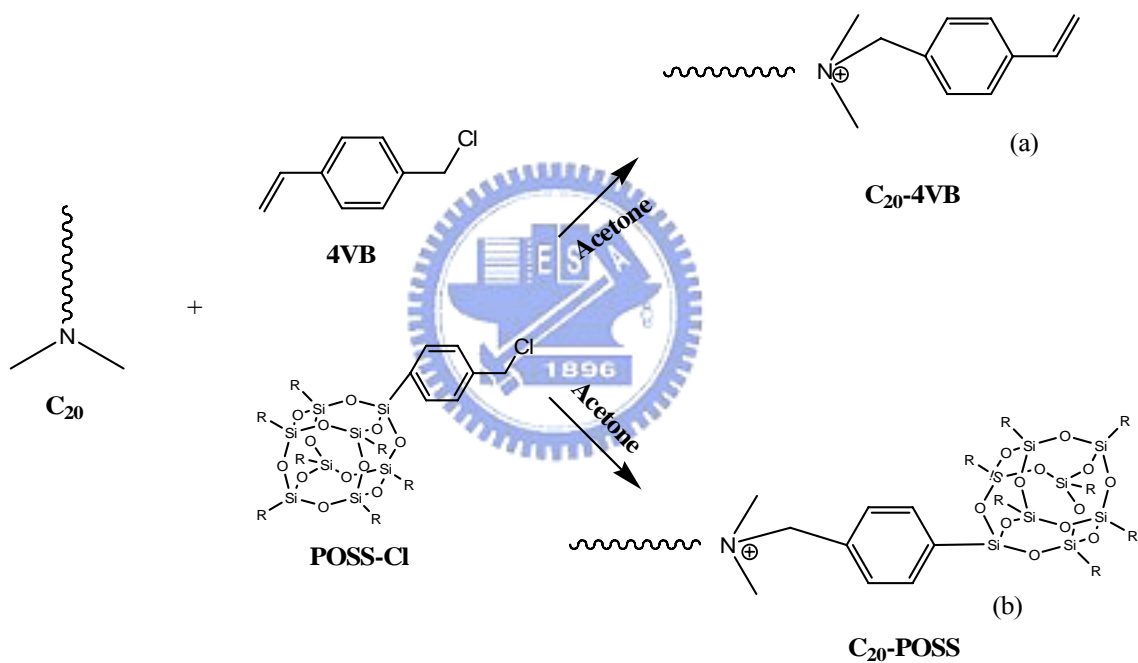
Scheme 2-1. Intercalation agents for organic modified clays preparation.



Scheme 2-2. Synthesis of the POSS -Cl compound.



Scheme 2-3. Synthesis of the C_{20} -4VB and C_{20} -POSS intercalated agents.



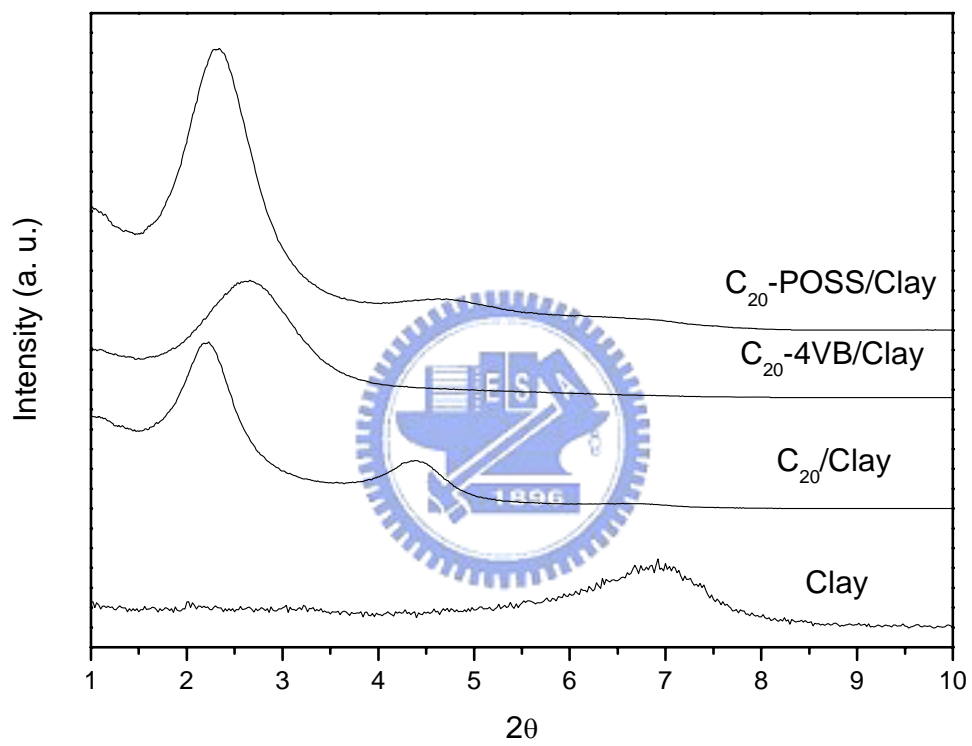


Figure 2-1. X-Ray diffraction patterns of pure clay, and intercalated clays.

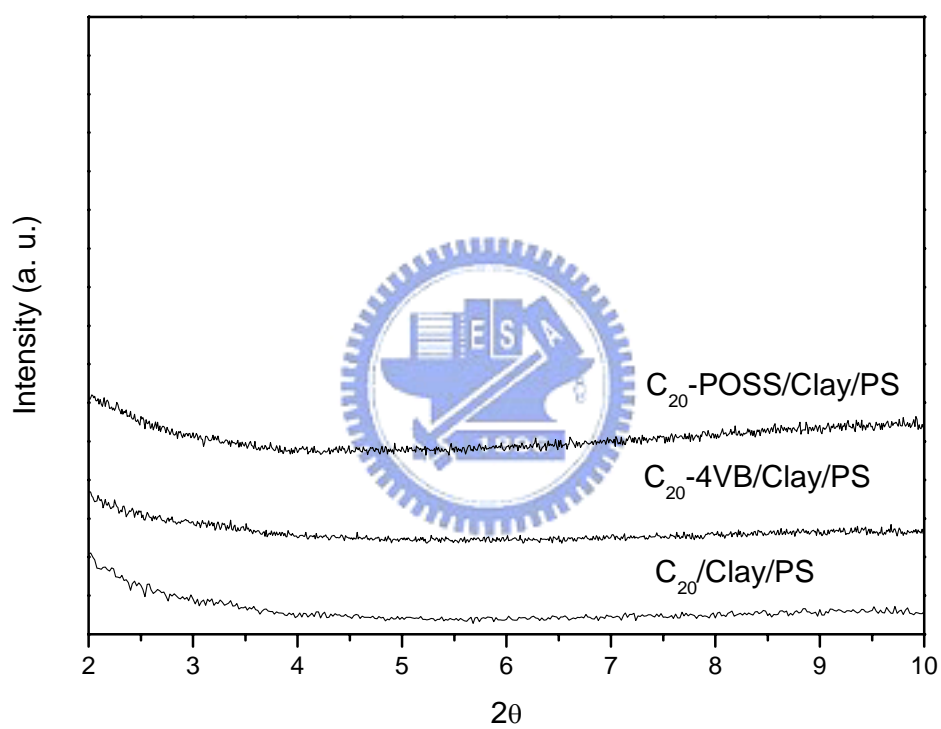


Figure 2-2. XRD spectra of the three surfactant-containing nanocomposites indicating the extent of delamination.

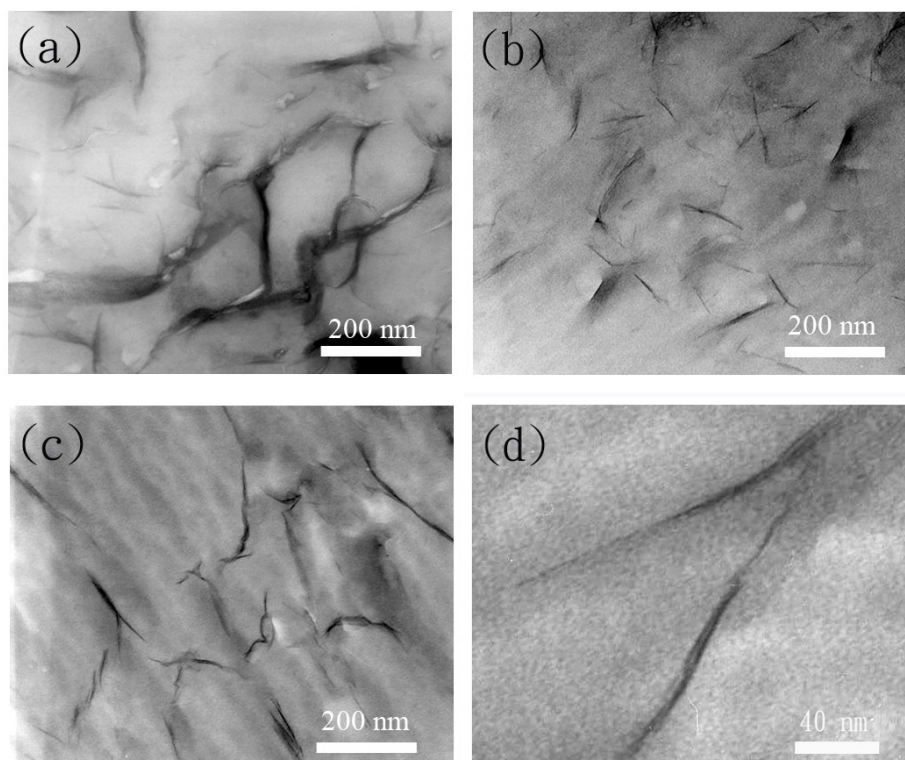


Figure 2-3. TEM images of (a) C₂₀, (b) C₂₀-4VB, (c) C₂₀-POSS (low magnification), and (d) C₂₀-POSS (high magnification)-treated nanocomposites.

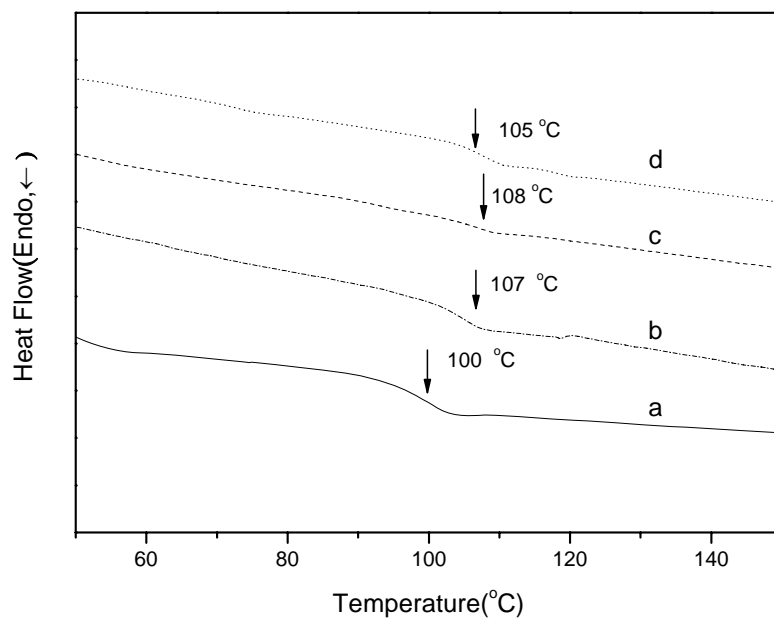


Figure 2-4. DSC curves glass transition temperature of (a) PS, (b) the nanocomposites formed used C₂₀, (c) the nanocomposites formed used C₂₀-4VB, and (d) the nanocomposites formed used C₂₀-POSS.



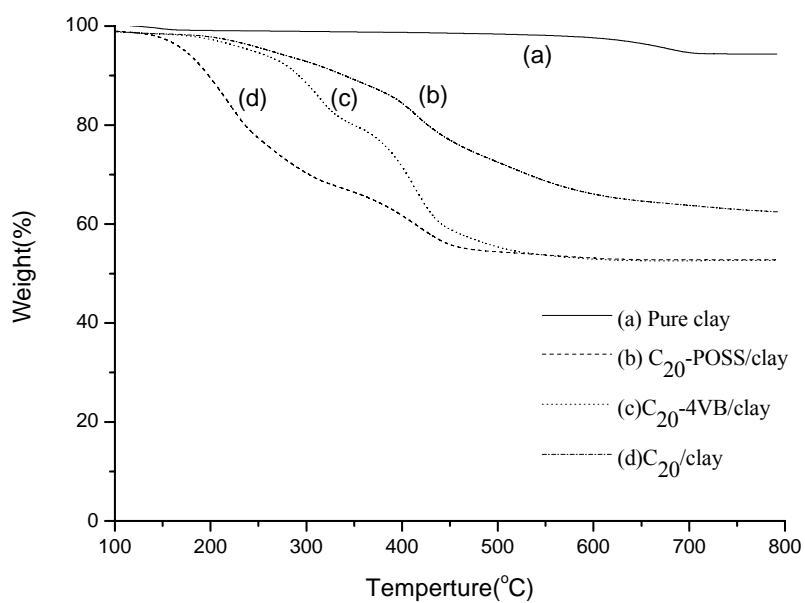


Figure 2-5. TGA curves of (a) Pure Clay, (b) C₂₀-POSS/Clay, (c) C₂₀-4VB/Clay, and

(d) C₂₀/Clay.



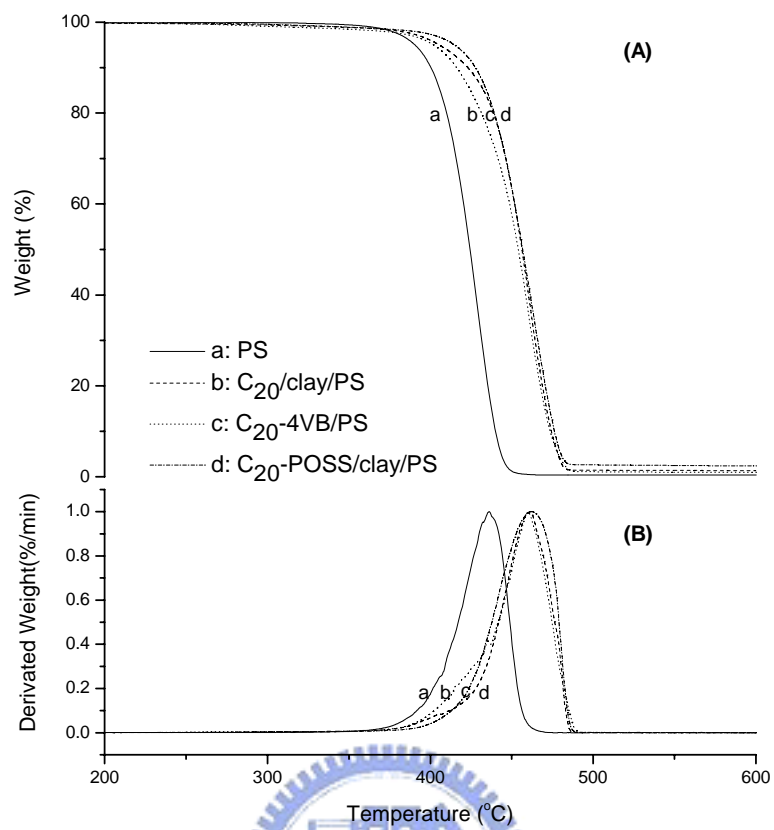


Figure 2-6. (A) TGA and (B) DTG curves of the nanocomposites under a nitrogen atmosphere: (a) pure PS, (b) the nanocomposite formed with C₂₀, (c) the nanocomposite formed with C₂₀-4VB, and (d) the nanocomposite formed with C₂₀-POSS.

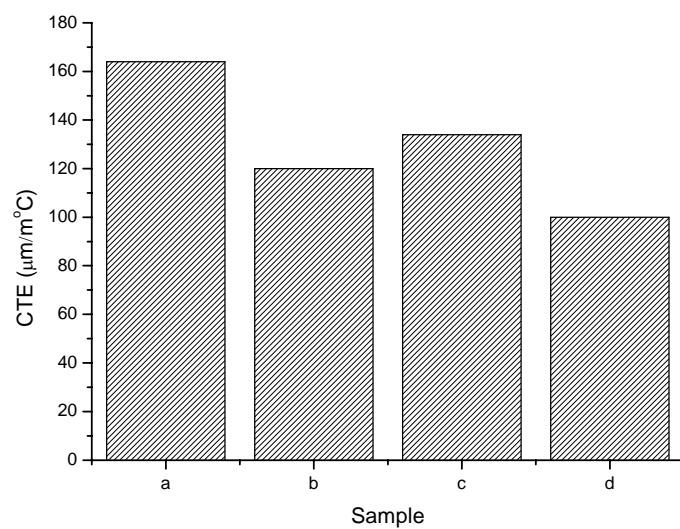


Figure 2-7. Coefficient of thermal expansion of (a) pure PS, (b) the nanocomposite formed with C_{20} , (c) the nanocomposite formed with C_{20} -4VB, and (d) the

nanocomposite formed with C_{20} -POSS.



Chapter 3

Properties Enhancement of PS Nanocomposites through the POSS surfactants

Abstract

The polyhedral oligomeric silsesquioxane (POSS)-clay hybrids of polystyrene are prepared by two organically modified clays using POSS-NH₂ and C₂₀-POSS as intercalated agents. X-ray diffraction (XRD) studies show that the formation of these POSS/clay/PS nanocomposites in all cases with the disappearance of the peaks corresponding to the basal spacing of MMT. Transmission electronic spectroscopy (TEM) was used to investigate the morphology of these nanocomposites and indicates that these nanocomposites are comprised of a random dispersion of exfoliated throughout the PS matrix. Incorporation of these exfoliated clay platelets into the PS matrix led to effectively increase in glass transition temperature (T_g), thermal decomposition temperature (T_d) and the maximum reduction in coefficient of thermal expansion (CTE) is ca. 40 % for the C₂₀-POSS/clay nanocomposite.

3.1 Introduction

Organic-inorganic hybrid materials are recognized as a new class of advanced material because they can be synthesized or processed using versatile approaches and own tunable properties [1-2]. Clays have been extensively used as reinforcement agents to prepare polymer-layered silicate nanocomposites with improved thermal and mechanical properties [3-9]. The incorporation of clay into polymer matrix imparts unique physical and chemical properties was first reported by the Toyota Research Lab for Nylon 6/organoclay nanocomposites [10]. These improvements are related to the dispersion of the layered silicate in the polymer matrix. Typically, the chemical structure of montmorillonite (MMT) consists of two fused silica tetrahedral sheets sandwiching an edge-shared octahedral sheet of either magnesium or aluminum hydroxide. Generally, the naturally occurring clays are hydrophilic character and require a modification by intercalating with amino acid, alkylammonium, or phosphonium salts to become organically compatible [11-12]. The resulting organophilic galleries of the organically modified montmorillonite (OMMT) will enhance the compatibility with polymer [13]. Several methods to make polymer clay nanocomposites have been demonstrated, including solution mixing, melt blending, and in situ polymerization [14-16]. The interaction of layered silicates with polymers leads to two classes of hybrid materials. In the first class, denoted as intercalated hybrids, one or more polymer chains are inserted between the host layers, generating ordered lamella with the distance of a few nanometers. In the second, described as delaminated hybrids, silicate layers of 1 nm thickness are exfoliated and dispersed in the polymer matrix.

Polyhedral oligimeric silsesquioxane (POSS) reagents, monomers, and polymers are emerging as new chemical feedstocks for the preparation of organic-inorganic

nanocomposites [17-21]. Silsesquioxane is the term for all structures with the formula $(\text{RSiO}_{1.5})_n$, where R is hydrogen or any alkyl, alkylene, aryl, arylene, or organic-functional derivative groups. POSS compounds with diameters of 1–3 nm can be possibly considered the smallest particles of silica, but unlike silica, silicones, or fillers, POSS molecules contain either functionalized or unfunctionalized substituents at each of the corner silicon atoms. These substituents can compatibilize POSS molecules with polymers or monomers. POSS macromonomer and POSS-containing polymers inspires to prepare the functionalized POSS cages, which can be used as the intercalating agents of layered silicates to prepare the nanocomposites combining the two types of nanoreinforcement agents and improved mechanical and thermal properties.

In this study, these nanocomposites were prepared by emulsion polymerization using the POSS-NH₂ and C₂₀-POSS-treated clays as shown in Scheme 3-1. The morphology and the extent of delamination of the nanocomposites are elucidated using the X-ray diffraction and transmission electron microscopy. The thermal properties of these nanocomposites are characterized by thermalgravimetric analysis and differential scanning calorimetry. The coefficient of thermal expansion of virgin PS and nanocomposites are measured by thermal mechanical analyzer.

3.2 Experimental

3.2.1 Materials

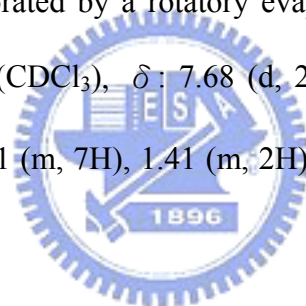
The sodium montmorillonite (Na^+ -MMT) with 1.45 mequiv/g cationic exchange capacity (CEC) was provided by Nanocor Co of USA. The majority of chemicals used in this study including, acetone, methanol, tetrahydrofuran, acetonitrile, potassium hydroxide (KOH), triethylamine, and trichloro [4-(chloromethyl)phenyl] silane were acquired from the Aldrich Chemical Co., Inc. The styrene monomer was purchased from Aldrich Chemical and purified by removing the inhibitor with the aid of an inhibitor-removal column. Sodium dodecyl sulfate (SDS) and hydrochloride acid (HCl) were both obtained from Curtin Matheson Scientific, Inc USA. Potassium persulfate ($\text{K}_2\text{S}_2\text{O}_8$) and aluminum sulfate [$\text{Al}_2(\text{SO}_4)_3$] were acquired from Fisher Scientific Co., USA. N, N-Dimethyloctadecylamine (C_{20}) was obtained from Acros Organics, USA. Trisilanolisobutyl polyhedral oligomeric silsesquioxane (T7-POSS) and aminopropylisobutyl polyhedral oligomeric silsesquioxane (POSS-NH₂) were obtained from Hybrid Plastics, Inc. All reagents, except styrene, were used as received without further purification.

3.2.2 Preparation of C_{20} -POSS intercalated agent.

The POSS-Cl compound was prepared by the method based on Scheme 3-2 [22]. Trisilanolisobutyl polyhedral oligomeric silsesquioxane (3 g) and Et_3N (1.26 g) were added into a 100 mL two-neck round bottom flask and stirred continuously 3 h under nitrogen, then 20 mL was added THF into the flask at 0 °C for 1 h. After stirring at 0 °C under nitrogen, triethylamine and trichloro[4-(chloromethyl) phenyl]silane(1.28 g) in THF (10 mL) were added dropwisely into the solution and stirred at 0 °C . The cooling bath was removed and stirred continuously for 7.5 h under nitrogen. The

POSS-Cl compound and HNEt₃-Cl byproduct were separated by filtration. The clear THF solution was dropped into a beaker of acetonitrile and rapidly stirred. The resulting product was collected and dried in a vacuum oven for 24 h. ¹H NMR (CDCl₃), δ : 7.59 (d, 2H), 7.33 (d, 2H), 4.52 (s, 2H), 1.92-1.62 (m, 7H), 1.09-0.85 (m, 42H), 0.75-0.48 (m, 14H).

The intercalated agent of C₂₀-POSS was prepared as shown in Scheme 3-2. N, N-dimethyloctadecylamine (C₂₀, 1.49 g) and POSS-Cl compound (5.68 g) in acetone (15 mL) were refluxed at 80 °C under nitrogen for 24 h. After cooling, the mixture was evaporated by a rotatory evaporator and then added Et₂O (20 mL). The solution was extracted with deionized water three times (150 mL × 3). The organic phase was dried with MgSO₄ and evaporated by a rotatory evaporator to obtain the C₂₀-POSS intercalated agent. ¹H NMR (CDCl₃), δ : 7.68 (d, 2H), 7.58 (d, 2H), 5.03 (s, 2H), 3.42 (t, 2H), 3.30 (s, 6H), 1.81 (m, 7H), 1.41 (m, 2H), 1.26 (m, 30H), 0.90 (m, 42H), 0.82 (t, 3H), 0.59 (m, 14H).



3.2.3 Preparation of POSS-NH₂ and C₂₀-POSS modified clays.

Na⁺ MMT (0.3 g) in deionized water (50 mL) was stirred continuously at 80°C for 4 h. The POSS-NH₂ (0.38 g) or C₂₀-POSS (0.63 g) in water (5 mL) was placed into another flask and then 10 % hydrochloric acid (1 mL) and ethanol (5 mL) were added and stirred at 80 °C for 1 h. This intercalated solution was poured slowly into the clay suspension solution and stirred vigorously at 80 °C for 4h. The resulting white precipitate was separated by filtration and then washed thoroughly with warm deionized water. The final product was dried in a vacuum oven at room temperature overnight.

3.2.4 Preparation of polystyrene/clay nanocomposites.

Na⁺-MMT (0.3 g) was dispersed in 40 mL of deionized water and stirred at 80 °C for 4 h. Based on the CEC value (145mequiv/100g) of the Na⁺-MMT and the Mw of the intercalated agent, the calculated weight (the weight of the intercalated agent needed to fully replace the Na⁺ of the clay) of the intercalated agent was added and stirred for 4 h. KOH (0.02 g), SDS (0.4 g), K₂S₂O₈ (0.05g) and styrene monomer (10 g) were added into the solution. After emulsification, the dispersion was flushed with nitrogen for 30 min while the temperature was raised to 80 °C under nitrogen protection. Polymerization was carried out at 80 °C for 8 h. After cooling, 10 mL of the 2.5 % aqueous aluminum sulfate was added into the polymerized emulsion, followed by dilute hydrochloric acid (10 mL) with stirring. Finally, acetone was added to break down the emulsion completely and then the polymer product was washed several times with methanol and deionized water. The white powder was filtered and dried in a vacuum oven at 80 °C for 24h. Similar procedures were employed to prepare the virgin polystyrene.

3.2.5 Instrumentations

3.2.5.1 Measurement the molecular weights characterization.

Molecular weight (M_w), number-average (M_n) molecular weight and polydispersity index (M_w/M_n) were measured using a Waters 410 gel permeation chromatography (GPC) system equipped with RI and UV detectors and a series of styragel columns (100, 500, and 10³ Å). The system was calibrated using polystyrene standards. These polymer chains were extracted from the clay surface using a reverse ion exchange reaction with LiCl/DMF to determine the molecular weight and molecular weight distribution.

3.2.5.2 Structure analysis characterization.

¹H NMR spectra were recorded in CDCl₃ on a Bruker AM 500 (500 MHz) Spectrometer using the solvent signal as an internal standard. FT-IR spectra were recorded using a Nicolet Avatar 320 FT-IR Spectrometer; 32 scans were collected at a spectral resolution of 1 cm⁻¹. The modified clay was mixed with KBr pellets to press into the small flakes and dried at 70 °C for 24h. The holder was placed in the sample chamber and spectrum was recorded under N₂ purge to maintain the test of the sample dryness.

Transmission electron microscopy (TEM) images were obtained on a Hitachi H-7500 operating at 100 kV. The sample was thin-section to ~70 nm by a Leica Ultracut UCT microtome. Wide-angle X-Ray diffraction (WAXD) experiments were carried on a Rigaku D/max-2500 type X-ray diffraction instrument with Cu K α radiation ($\lambda=1.54\text{\AA}$) using a Ni-filter. Data were recorded in the range of $2\theta= 1$ to 20 at the scanning rate of $0.6^\circ/\text{min}$.

3.2.5.3 Thermal and mechanical analysis characterization.

Thermal stability of nanocomposite was investigated by a TA Instruments Q50 apparatus. The sample ~5 mg was placed in a Pt cell with scan rate of 20 °C /min from 30 to 800 °C under a 40 mL/min flow of nitrogen gas. Thermal analysis through differential scanning calorimetry (DSC) was performed using a Du-Pont (DSC-2010) to measure the glass transition temperature (T_g) of the nanocomposite. The sample was preheated at a scan rate of 20 °C /min from 30 to 150 °C under a nitrogen atmosphere. A small sample (ca. 5-10 mg) was weighted and sealed in an aluminum pan. The sample was quickly cooled to 10 °C from the first scan and then scanned

between 30 and 150 °C at the scan rate of 20 °C /min. The glass transition temperatures are taken as the midpoint of the heat capacity transition between the upper and lower points of deviation from the extrapolated glass and liquid lines. The coefficient of thermal expansion (CTE) was measured using a thermomechanical analyzer (TMA TA 2940) by recording the change in dimension of the specimen with temperature. The specimen was heated from 25 to 150 °C at a heating rate of 5 °C/min.



3.3 Results and discussion

3.3.1 Morphologies of modified clays and nanocomposites.

Microstructures of polymer-layered silicate nanocomposites were characterized by XRD and TEM. Figure 3-1 shows the X-ray diffraction curves of the pristine clay and modified clays in the 2θ region of $2-10^\circ$. For the pristine clay, the Bragg diffraction peak at $2\theta=6.92^\circ$ corresponds to d -spacing of 1.28 nm. For the POSS-NH₂/clay and C₂₀-POSS/clay, the 2θ value shifts from 6.92° (1.28 nm) to 5.51° (1.61 nm) and 2.33° (3.80 nm) after ion exchange, indicating that the basal spacing is expanded as the sodium cations in the interlayer galleries are replaced by intercalated agents of POSS-NH₂ and C₂₀-POSS. The increase of the basal spacing indicates that the clay can be efficiently intercalated by POSS-NH₂ and C₂₀-POSS. The d -spacing of the C₂₀-POSS-modified clay is substantially greater than the POSS-NH₂-modified clay. Larger interlayer spacing favors the penetration of styrene monomer and the formation of exfoliated nanocomposite by providing more hydrophobic environment. The pure POSS-NH₂ has characteristic diffraction peaks arising from the aggregation of the POSS [23]. Figure 3-2 shows XRD patterns of the unmodified clay and the C₂₀-POSS modified clay. The pure C₂₀-POSS has a broad peak in the region of $5-12^\circ$ arising from the C₂₀ long aliphatic chain. When the C₂₀-POSS is inserted between the galleries of the clay, the d spacing is increased from 1.28 nm for original clay to 3.80 nm, implying that the organic modifier is incorporated between and pushing the clay layers. Both nanocomposites do not show XRD diffraction peak as shown in Figure 3-3, indicating the silicate layers are exfoliated in the polymer matrix. TEM images for POSS-NH₂/clay and C₂₀-POSS/clay nanocomposites at 3% inorganic clay loading are shown in Figures 3-4(a) and 3-4(b), indicating that the exfoliated clay platelets are distributed in the matrix homogeneously and randomly.

3.3.2 Fourier transfer infrared analyses.

The representative FT-IR spectra of the organophilic clay, POSS-NH₂-modified and C₂₀-POSS modified clays are given in Figure 3-5. After ion exchange, FT-IR spectroscopy can provide important information regarding the difference between intercalated agents and modified clays. In Figure 3-5(a), characteristic vibration bands of the pure clay are 1030 cm⁻¹ (Si-O), 520 cm⁻¹ (Al-O), and 470 cm⁻¹ (Mg-O) [24-26]. In Figure 3-5(b), the absorption peaks in the region of 2950-2800 is assigned to the stretching vibration of aliphatic C-H. The symmetrical Si-O-Si band in the silsequioxane cage is characterized by the stretching band at 1109 cm⁻¹. In Figure 5(d), C₂₀-POSS contains both alkyl chain and POSS moiety where the POSS moiety exhibits characteristic absorption peaks at 2950–2800 cm⁻¹ (C–H bonds), 1230 cm⁻¹ (Si–C bonds), 1109 cm⁻¹ (Si–O–Si bonds of the cage structure). The characteristics of the vibration band of alkyl chain appear at 2920, 2850, and 1475 cm⁻¹ (–CH₂– vibration bands). Figures 3-5(c) and 3-5(e) show the features of combination of characteristic bands of pure clay, POSS-NH₂, and C₂₀-POSS. IR analysis further confirms the existence of these intercalated agents in these intercalated clay samples, implying that these intercalation of the intercalated agents are indeed present within the gallery gap. These observations support the explanation in the earlier observation from XRD.

3.3.3 Thermal properties.

Figure 3-6 presents DSC traces of these nanocomposites with different intercalated agents. All DSC thermograms display single glass transition temperatures in the experimental temperature range. The glass transition temperature of PS occurs

at 100 °C. With the addition of the POSS and C₂₀-POSS modified MMT to the polymer matrix, the glass transition temperatures (T_g s) of the POSS-NH₂/clay/PS and C₂₀-POSS/clay/PS are 108, and 105 °C, respectively. From the DSC results that the incorporation of the organoclay resulted in an increase in the T_g relative to virgin PS, as summarized in Table 3-1. The addition of clay results in T_g increase which can be attributed to the retardation of PS chain movement.

Figure 3-7 presents the thermal stabilities of POSS-NH₂- and C₂₀-POSS-modified clays and nanocomposites investigated by TGA. Both nanocomposites show improved thermal stabilities than the virgin PS. The improvement in the degradation temperature is mainly due to the homogeneous dispersion of silicate nanoplatelets in the PS matrix [27-30]. In Figure 3-7, the C₂₀-POSS/clay decomposes at 262 °C while the POSS-NH₂/clay decomposes at higher temperature of 386°C. The POSS-NH₂-modified clay is relatively more stable than the C₂₀-POSS-modified clay. Essentially all nanocomposites give higher decomposition temperatures than the pristine PS and the improved thermal stability can be attributed to the diffusion hindrance of the decomposed volatiles. The values of 5% and 50% weight loss temperatures and the char yields are summarized in Table 1.

3.3.4 Molecular weights of the nanocomposites.

Molecular weight and molecular weight distribution (PDI) by GPC analyses of polymer samples recovered after excluding all clay content are listed in Table 3-2. From the Table 3-2, molecular weight (M_w or M_n) of the PS in the PS/clay nanocomposites is higher than the pure PS, suggesting that clay may act as a catalytic agent responsible for the observed higher molecular weight of the PS with the

proceeding emulsion polymerization.

3.3.5 Coefficient of thermal coefficient.

Thermal mechanical analyzer (TMA) was used to determine the coefficient of thermal expansion of the POSS/clay nanocomposites. The thermal expansion coefficient is an important issue for polymers in engineering applications. The CTE was measured from the initial linear slope of the thermal strain-temperature plot. A low thermal expansion coefficient is often desirable to achieve dimensional stability and can be achieved by incorporation of a rigid and low CTE filler material. From the data in Table 3-1, the CTE of the virgin PS is $164 \mu\text{m}/\text{m } ^\circ\text{C}$ and the addition 3 wt % organically modified clays reduces the CTE values to 98 and $100 \mu\text{m}/\text{m } ^\circ\text{C}$ for POSS/clay/PS and C₂₀-POSS/clay/PS approximately 40 % reduction relative to the virgin PS.

In general, the extent of CTE reduction depends on the particle rigidity and fine dispersion of the clay platelets in the PS matrix and also duo to efficient stress transfer to clay layers. The retardation of PS chain segmental movement through incorporation of organically modified clays also leads to decrease in the coefficient of thermal expansion (CTE). The incorporation of the organically modified clays results in significant improvement in dimensional stability of the PS matrix.

3.4 Conclusions.

The POSS-clay hybrids of polystyrene are prepared via emulsion polymerization using two organically modified clays, POSS-NH₂ and C₂₀-POSS, as intercalated agents. X-ray diffraction (XRD) results indicate that the clay is successfully intercalated by POSS-NH₂ and C₂₀-POSS. The random dispersion of these exfoliated silicate layers in these nanocomposites are identified by XRD and TEM. These well dispersed clay platelets in PS matrix result in improved thermal properties in terms of thermal decomposition temperature (T_d) and glass transition temperature (T_g). In addition, the incorporation of these organoclay results in significant reduction in coefficient of thermal expansion of virgin PS.

Acknowledgments

The authors thank the National Science Council, Taiwan, for financially supporting this research under Contract NSC-95-2221-E-009-118.



References

- [1] Klok, H. A.; Lecommandoux, S. *Adv. Mater.* **2001**, 13, 1217.
- [2] Sanchez, C.; Soler-Illia, G. J.; Ribot, F.; Lalot, T. Mayer, C. R.; Cabuil, V. *Chem. Mater.* **2001**, 13, 3061.
- [3] Park, C.; Smith, Jr. J. G.; Connell, J. W.; Lowther, S. E.; Working, D. C. Siochi, E. *J. Polymer* **2005**, 46, 9694.
- [4] Yei, D. R.; Kuo, S. W. Fu, H. K.; Chang, F. C. *Polymer* **2005**, 46, 741.
- [5] Xie, W.; Hwu, J. M.; Jiang, G. J. *Polymer Engineering and Science* **2003**, 43, 214.
- [6] Yei, D. R.; Kuo, S. W.; Su, Y. C.; Chang, F. C. *Polymer* **2004**, 45, 2633.
- [7] Tseng, C. R.; Wu, J. Y.; Lee, H. Y.; Chang, F. C. *J. Appl. Polym. Sci.* **2002**, 85, 1370.
- [8] Su, S.; Wilkie, C. A. *J. of Polym. Sci. Part A: Polym. Chem.* **2003**, 41, 1124.
- [9] Kim, M. H.; Park, C. I.; Choi, W. M.; Lee, J. W.; Lim, J. G. Park, O. O. *J. Appl. Polym. Sci.* **2004**, 92, 2144.
- [10] Okado, A.; Kawasumi, T.; Kamigato, O. *Polymer Preprint* **1987**, 28, 447.
- [11] Kong, D.; Park, C. E. *Chem. Mater.* **2003**, 15, 419,.
- [12] Xu, W. B.; Bao, S. P.; He, P. S. *J. Appl. Polym. Sci.* **2002**, 84, 842.
- [13] Akelah ,A.; Prasad, P. N.; Mark, J. E.; Tung, J. F. *Polymers and others advanced materials: emerging technologies and business opportunities*. New York: Plenum, **1995**.
- [14] Raia, R. A.; Vasudevin, S.; Krawiec, W.; Scanlon, L. G.; Giannelis, E. P. *Adv. Mater.* **1995**, 7, 154.
- [15] Giannelis, E. P. *Adv. Mater.* **1996**, 8, 29.
- [16] Gilman, J. W.; Morgan, A. B.; Harris, R. H.; Trulove, P. C.; Delong, H. C.; Sutto, T. E. *Polymer Science and Engineering* **2000**, 83, 59.

- [17] Lichtenhan, J. D.; Vu, N. Q.; Carter, J. A.; Gilman, J. W.; Feher, F. J. *Macromolecules* **1993**, 26, 2141.
- [18] Lichtenhan, J. D.; Otonari, Y. A.; Carr, M. J. *Macromolecules* **1995**, 28, 8435.
- [19] Haddad, T. S.; Lichtenhan, J. D. *Journal of Inorganic Organometallic Polymer* **1995**, 33, 237.
- [20] Mantz, R. A.; Jones, P. J.; Chaffee, K. P.; Lichtenhan, J. D.; Gilman, J. W.; Ismail, I. M. K.; Burmeister, M. J. *Chem. Mater.* **1996**, 8, 1250.
- [21] Haddad, T. S.; Lichtenhan, J. D. *Macromolecules* **1996**, 29, 7302.
- [22] Huang, C. F.; Kuo, S. W.; Lin, F. J.; Huang, W. J.; Wang, C. F.; Chen, W. Y.; Chang, F. C. *Macromolecules* **2006**, 39, 300.
- [23] Zhang, H.; Wang, C.; Li, M.; Ji, X.; Zhang, J.; Yang, B. *Chem. Mater.* **2005**, 17, 4783.
- [24] Yeh, J. M.; Liou, S. J.; Lai, C. Y.; Wu, P. C. *Chem. Mater.* **2001**, 13, 1131.
- [25] Yeh, J. M.; Liou, S. J.; Lin, C. Y.; Cheng, C. Y.; Chang, Y. W.; Lee, K. R. *Chem. Mater.* **2002**, 14, 154.
- [26] Yeh, J. M.; Chen, C. L.; Chen, Y. C.; Ma, C. Y.; Lee, K. R.; Wei, Y. Li, S. *Polymer* **2002**, 43, 2729.
- [27] Uthirakumar, P.; Nahm, K. S.; Hahn, Y. B. Lee, Y. S. *European Polymer Journal* **2004**, 40, 2437.
- [28] Chen, T. K.; Tien, Y. I.; Wei, K. H. *J. Polym. Sci. Part A: Polym. Chem.* **1999**, 37, 2225.
- [29] Doh, J. G.; Cho, I. *Polymer Bulletin* **1998**, 41, 511.
- [30] Fu, X.; Qutubiddin, S. *Polymer* **2001**, 42, 807.

Table 3-1. Results of Thermal and Mechanical properties of Polystyrene and

Polystyrene Nanocomposites.

Sample	$T_g, (^{\circ}\text{C})^a$	$T_{0.05}, (^{\circ}\text{C})^b$	$T_{0.5}, (^{\circ}\text{C})^c$	Char at 600 $^{\circ}\text{C}$ (%)	CTE ($\mu\text{m}/\text{m } ^{\circ}\text{C}$)
PS	100 \pm 0.5	390 \pm 1.7	424 \pm 0.8	0	164 \pm 2
POSS/Clay/PS	108 \pm 0.6	411 \pm 1.3	446 \pm 1.2	2.9	98 \pm 1
C20-POSS/Clay/PS	105 \pm 0.3	415 \pm 1.1	457 \pm 0.9	2.4	100 \pm 3

^a Glass transition temperature(T_g).

^b 5% Degradation temperature($T_{0.05}$).

^c 50% Degradation temperature($T_{0.5}$).

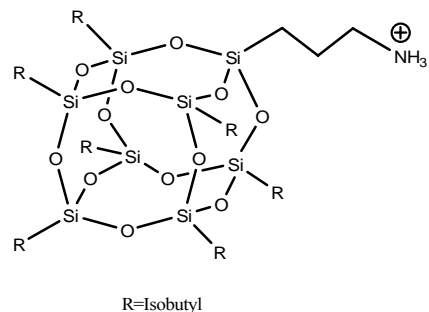


Table 3-2. Molecular Weights of Polystyrene and Polystyrene Nanocomposites

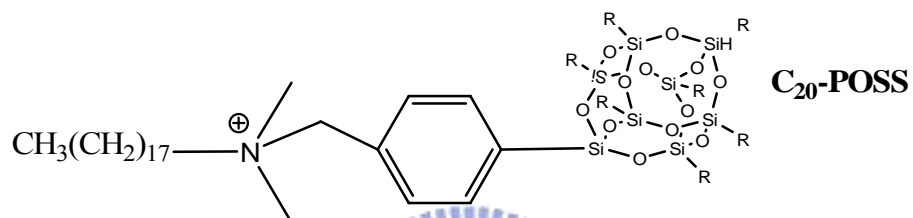
Sample	$M_n(\times 10^4)^a$	$M_w(\times 10^4)^b$	$PDI(M_w/M_n)^c$
PS	34.5	53.1	1.54
POSS-NH ₂ /Clay/PS	40.9	54.0	1.32
C20-POSS/Clay/PS	47.7	58.7	1.23

^aNumber-average molecular weights (M_n) and ^bweight-average molecular weights (M_w) were determined by GPC. ^cPolydispersity index, M_w/M_n .



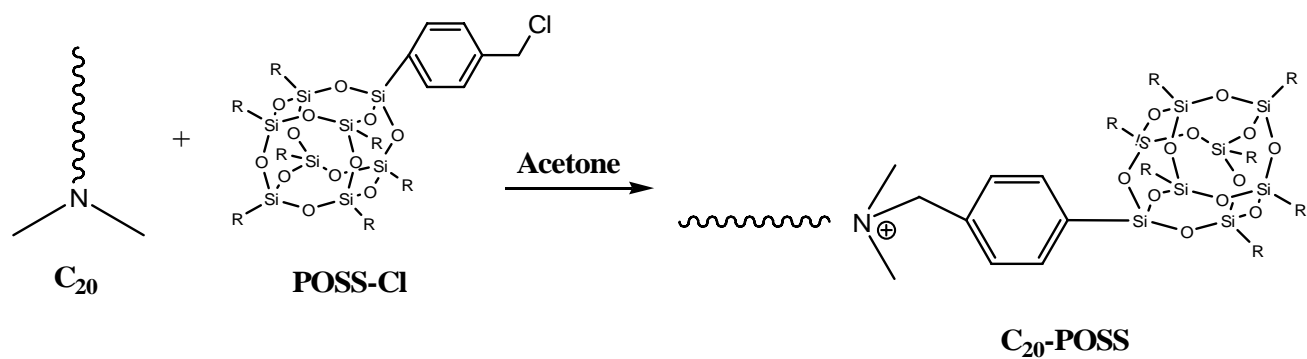


POSS-NH₂

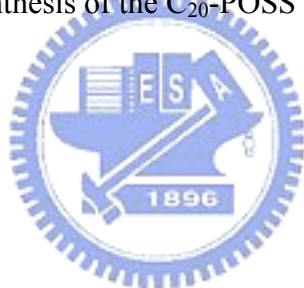


C₂₀-POSS

Scheme 3-1. Chemical structures of the intercalated agents used to prepare the modified clays.



Scheme 3-3. Synthesis of the C_{20} -POSS intercalated agent.



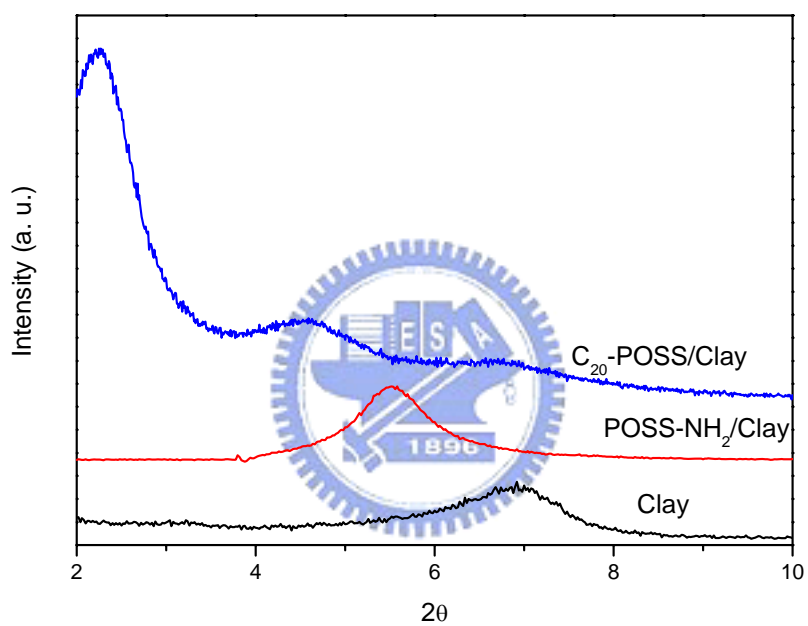


Figure 3-1. X-Ray diffraction patterns of pure clay, and intercalated clay.

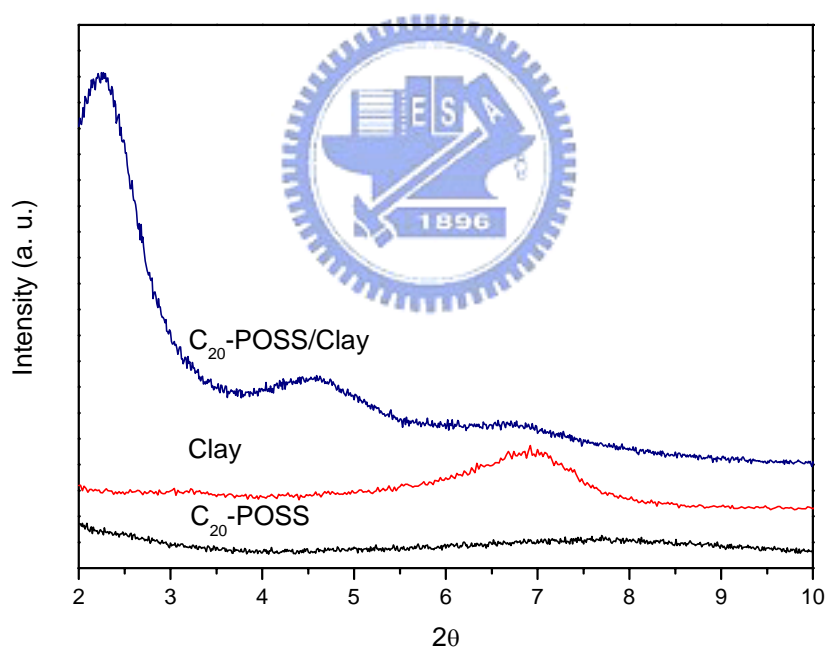


Figure 3-2. XRD spectra of C₂₀-POSS, pure clay, and C₂₀-POSS/Clay.

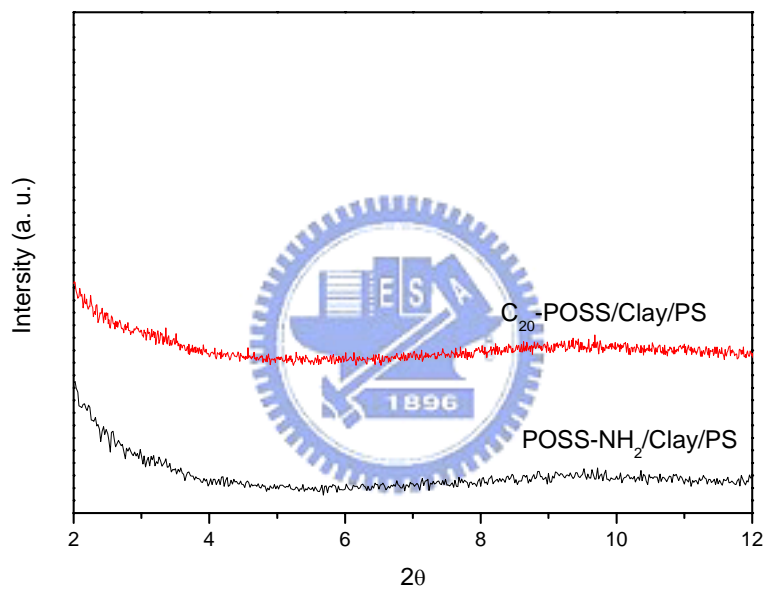


Figure 3-3. XRD spectra of the two surfactant-containing nanocomposites indicating the extent of delamination.

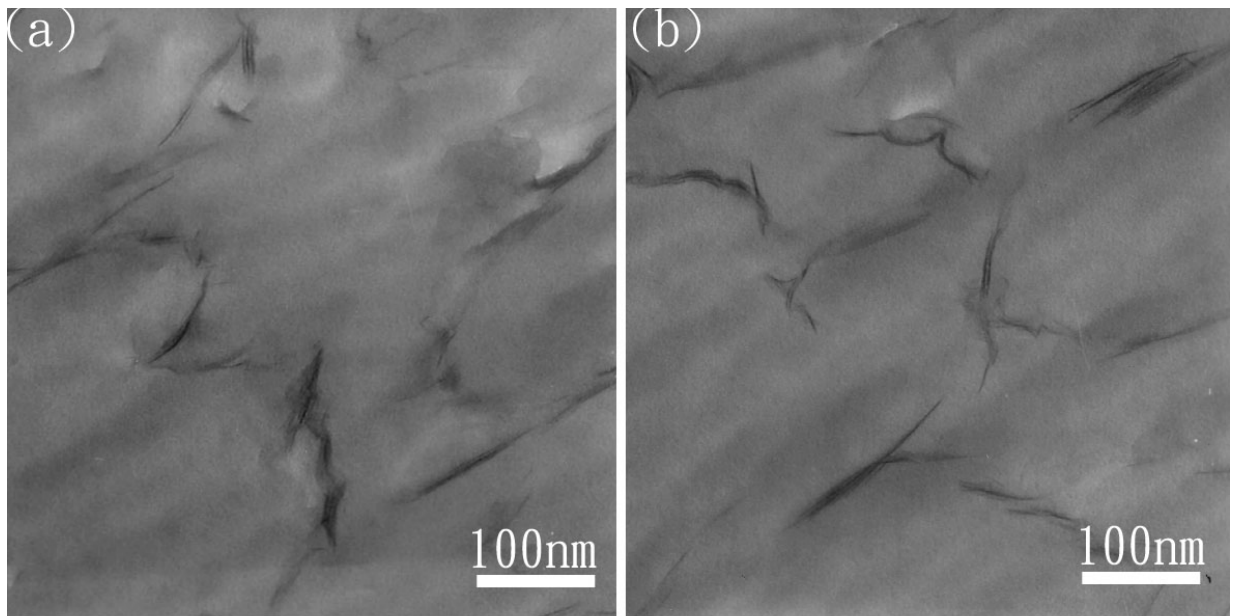


Figure 3-4. TEM images of (a) POSS-NH₂ and (b) C₂₀-POSS-treated nanocomposites.

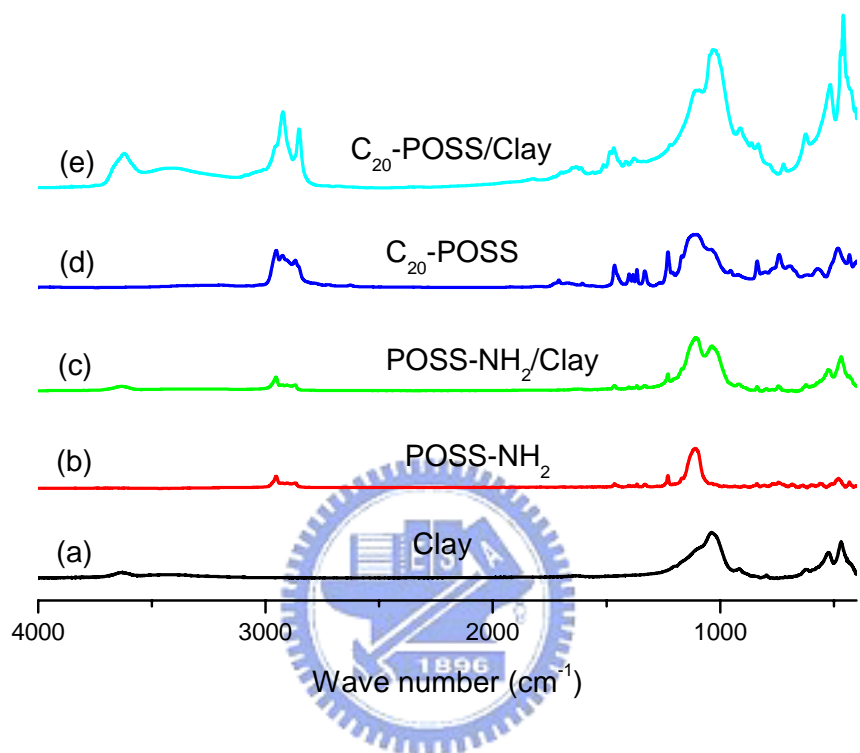


Figure 3-5. IR spectra of the two intercalated agent, intercalated clay, and pure clay.

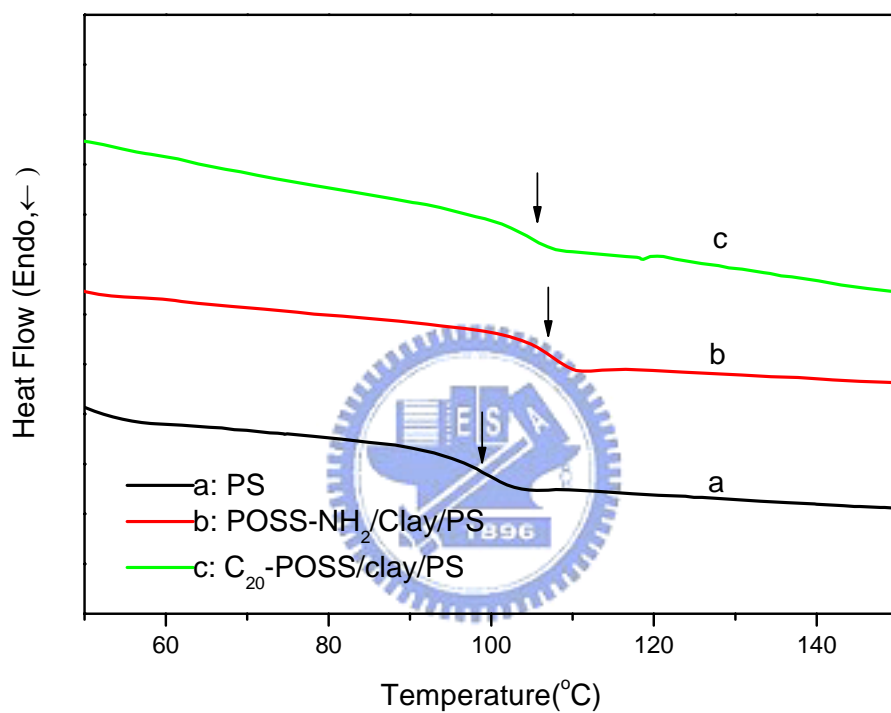


Figure 3-6. DSC curves glass transition temperature of (a) PS, (b) the nanocomposites formed used POSS-NH₂, and (c) the nanocomposites formed used C₂₀-POSS.

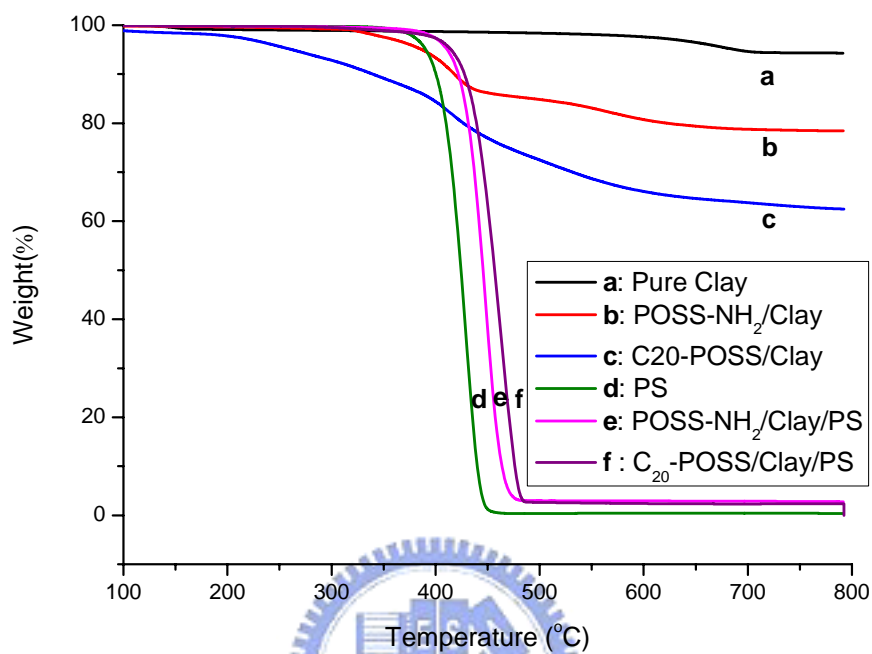


Figure 3-7. TGA curves of (a) pure Clay, (b) POSS-NH₂/Clay, (c) C₂₀-POSS/Clay, (d) pure PS, (e) the nanocomposite formed with POSS-NH₂, and (f) the nanocomposite formed with C₂₀-POSS.

Chapter 4

Effect of the organically modified Nanoclay on Low-Surface-Energy Materials of Polybenzoxazine

Abstract

Novel low surface free energy materials of polybenzoxazine/organically modified silicate nanocomposites have been prepared and characterized. The CPC (cetylpyridinium chloride)/clay10%/Poly(3-phenyl-3,4-dihydro-2H-1,3-benzoxazine) (PP-a) possesses an extremely low surface free energy (12.7 mJ/m^2) after 4 hrs curing at $200 \text{ }^\circ\text{C}$, even lower than that of poly(tetrafluoroethylene) (22.0 mJ/m^2) calculated on the basis of the three-liquid geometric method. X-ray photoelectron spectroscopy (XPS) shows higher silicon content on the surface of nanocomposites than average composition, implying that the clay is more preferentially enriched on the outermost layer. In addition, the glass transition temperature (T_g) of the polybenzoxazine (PP-a) in the nanocomposite is $22.6 \text{ }^\circ\text{C}$ higher and its thermal decomposition temperature is also $31.5 \text{ }^\circ\text{C}$ higher than the pure PP-a. This finding provides a simple way to prepare lower surface energy and high thermal stability material.

4.1 Introduction

Materials with low surface energy have attracted considerable attention recently because of numerous practical applications. Both poly(tetrafluoroethylene) (PTFE) and poly(dimethylsiloxane) (PDMS) are well-known materials possessing low surface free energies [1-4]. PTFE may be regarded as the benchmark lower surface free energy material, displaying water repellency [5] in combination with other desirable properties [6]. However, PTFE and many fluorinated polymers have some applications limitations such as high cost and poor processibility.

Hybrid organic-inorganic materials have shown superior physical properties compared to conventional materials [7-9]. Montmorillonite (MMT) clay consists two fused silica tetrahedral sheets sandwiching an edge-shared octahedral sheet of either magnesium or aluminum hydroxide. The clay can be functionalized by various organic cations through ion exchange where the metal ions are replaced by organic cations intercalated the silicate layers to make the clay organophilic and compatible with polymers [10,11].

Polybenzoxazines have been developed as a new type of phenolic resin and have attracted great interest from academia and industry because of their fascinating characteristic, such as low water absorption, high moduli, [12] high glass-transition temperature [13] and low surface free energy. [14]. In this study, the CPC modified clay is employed to prepare polybenzoxazine/clay nanocomposites. The detail morphologies, intermolecular and intramolecular interactions, thermal and surface properties of polybenzoxazine/clay nanocomposites are investigated in this study.

4.2 Experimental

4.2.1 Preparation of CPC-modified clays

Na⁺ Montmorillonite (0.3 g) was dispersed in 1L deionized water and stirred continuously at 80 °C for 4 h. The CPC (0.156 g) was placed into another flask, 10 % hydrochloric acid (1 mL) and ethanol (5 mL) were added and then stirred at 80 °C for 1 h. The intercalating agent solution was then poured into the clay suspension solution and stirred vigorously at 80 °C for 4 h. The resulting white precipitate was separated by filtration and then washed several times with warm deionized water. The final product was dried in a vacuum oven at 65 °C overnight.

4.2.2. Preparation of CPC/clay/PP-a nanocomposites by solvent method

The organically modified montmorillonite (3g) was dispersed homogeneously in THF (10mL) and stirred at room temperature for 2h. The P-a monomer was added into the organically modified clay suspension and vigorously stirred at room temperature for 48 h. The solution was spin-coated onto a glass slide (100 × 100 × 1 mm³) operating at 300 rpm for 45 s. The sample was left to dry at 65 °C and then cured in an oven at 200 °C for 4 h.

4.2.3. Characterizations

Thermal analyses were performed using a Du-Pont (DSC-2010). The sample was preheated at a scan rate of 20 °C /min from 30 to 150 °C under a nitrogen atmosphere. The sample was quickly cooled to 10 °C from the first scan and then scanned between 30 and 250 °C at the scan rate of 20 °C /min. Thermal stabilities of the cured nanocomposites were investigated using a TA Instruments Q50 apparatus at a heating

rate of 20 °C /min from 30 to 800 °C. Wide-angle X-Ray diffraction (WAXD) experiments were carried on a Rigaku D/max-2500 type X-ray diffraction instrument with Cu K α radiation ($\lambda=1.54\text{\AA}$) using a Ni-filter. Data were recorded in the range of $2\theta= 1$ to 20 at the scanning rate of 0.6°/min. Transmission electron microscopy (TEM) images were obtained on a Hitachi H-7500 operating at 100 kV using sample with thin-section ~ 70 nm. For contact angle measurements, deionized water, ethylene glycol, and diiodomthane were used as standards to measure the surface free energies. The advancing contact angle measurement of a sample was determined at 25 °C after injection of a liquid drop (5 μ L) onto the surface and a Krüss GH-100 goniometry interfaced to image-capture software was employed to perform the measurement. X-ray photoelectron spectroscopy (XPS) characterization was performed using a VG Microlab 310F Spectrometer equipped with an Al K α X-ray source (1486.6 eV). Surface roughness profiles and phase imaging of film structure were acquired using a digital Instruments DI5000 scanning probe microscope in the tapping mode with a typical radius of curvature < 7 nm.

4.2.4 Surface energy determination

When a liquid drop comes into contact with an ideally smooth and homogeneous solid, it exhibits an equilibrium contact angle that can be expressed using Young's equation: [15, 16]

$$\gamma_{LV} \cos \theta = \gamma_{SV} - \gamma_{SL} \quad (4-1)$$

where γ_{LV} is the surface tension of the liquid in equilibrium with its own vapor, γ_{SL} is the interfacial tension between the liquid and solid, and γ_{SV} is the surface tension of the solid in equilibrium with the saturated liquid vapor, and θ is the contact angle.

In terms of γ_s (the surface tension of the solid), Young's equation is rewritten as

$$\gamma_{LV} \cos \theta = \gamma_s - \gamma_{SL} - \pi_e \quad (4-2)$$

where $\pi_e \equiv (\gamma_s - \gamma_{SV})$ is the equilibrium pressure. It is generally believed that if the contact angle is greater than zero, π_e is negligible. Therefore, eq. 1 can be rewritten as:

$$\gamma_{LV} \cos \theta = \gamma_s - \gamma_{SL} \quad (4-3)$$

Two-Liquid Geometric Method

Owens and Wendt, and Kaelble, extended Fowkes' hypothesis [15, 16] and gave the following equation to express γ_{SL} :

$$\gamma_{SL} = \gamma_s + \gamma_{LV} - 2(\gamma_s^d \gamma_{LV}^d)^{1/2} - 2(\gamma_s^p \gamma_{LV}^p)^{1/2} \quad (4-4)$$

Combining eqs. 2 and 3 yields:

$$\gamma_{LV} (1 + \cos \theta) = 2(\gamma_s^d \gamma_{LV}^d)^{1/2} + 2(\gamma_s^p \gamma_{LV}^p)^{1/2} \quad (4-5)$$

where the superscript d refers to the dispersion (nonpolar) component and the superscript p refers to the polar (nondispersion) component including all of the interactions established between the solid and liquid, such as dipole–dipole, dipole-induced dipole, and hydrogen bonding interactions.

Because γ_s is the sum of the surface tension components contributed from the dispersion and polar components, eqs. 4 and 5 provide a method to estimate the surface tension of solids.

$$\gamma_s = \gamma_s^d + \gamma_s^p \quad (4-6)$$

Using two liquids having known values of γ_L^d and γ_L^p for contact angle measurements, γ_s^d and γ_s^p can be readily determined by solving the following two

equations:

$$\gamma_{LV1}(1 + \cos \theta_1) = 2(\gamma_S^d \gamma_{LV1}^d)^{1/2} + 2(\gamma_S^p \gamma_{LV1}^p)^{1/2} \quad (4-7)$$

$$\gamma_{LV2}(1 + \cos \theta_2) = 2(\gamma_S^d \gamma_{LV2}^d)^{1/2} + 2(\gamma_S^p \gamma_{LV2}^p)^{1/2} \quad (4-8)$$

The values of γ_L^d and γ_L^p of the reference liquids have been provided by Kaelble.

[17]

4.3 Results and discussion

Figure 4-1 shows the XRD plots for the (a) pristine clay, the (b) CPC-modified clay and (c,d, and e) polybenzoxazine/clay nanocomposites with various CPC-modified clay contents. The original clay has an intergallery spacing of 1.28 nm. The CPC-modified clay shows the d spacing of 2.56 nm, corresponding to an increase of 1.28 nm, providing the evidence that the clay galleries were expanded after CPC insertion. The modification of the hydrophilic silicate layer rendered the hydrophobic and consequently more compatible with the P-a monomer. In these polybenzoxazine/clay nanocomposites, the (001) diffraction peak $2\theta = 2.78^\circ$ for all clay contents corresponding to a basal spacing of 3.17 nm. When the polybenzoxazines are inserted within the galleries of the MMT, the d spacing is increased from 1.28 for the pristine MMT to 3.17 nm for CPC/clay/polybenzoxazine (PP-a) nanocomposites. Since the angle of detection limitation of XRD, it is impossible to detect diffraction angle below 1° . Thus, it is necessary to observe the true structure and distributions of these silica platelets by using the TEM. TEM images for CPC/clay/polybenzoxazine (PP-a) nanocomposite at 3 % inorganic clay loading are shown in Figure 4-2, indicating the partial aggregation of these clay platelets configuration. From XRD and TEM results, these nanocomposites all possess intercalated structures.

Table 4-1 present the thermal stabilities of the CPC/clay/polybenzoxazine (PP-a) nanocomposites investigated by DSC and TGA analyses. The glass transition temperature of the nanocomposite increases with the increase of clay loading, indicating that the motion of the polybenzoxazine is retarded by the silicate layers. In addition, thermal stability of the nanocomposites also is improved, both thermal degradation temperature (T_d) and char yield of these nanocomposites are increased with the increase of the clay loading. When increasing the clay loading to 10 %, the thermal degradation temperature is 357.1 °C, an increase of 35.4 °C than virgin polybenzoxazines (PP-a). Due to the nature of the inorganic clay, the char yield of the nanocomposites increases with the increase of clay content as would be expected.

Surface free energies of polybenzoxazines (PP-a)/clay nanocomposites with various clay contents are summarized in Table 4-1 based on van Oss and Good's three-liquid method [20, 21]. The surface roughness of all specimens are less than 50 nm, therefore, the influence of topography on the surface free energy is considered insignificant [22, 23]. It is clear that the increase of clay content resulting in significant decrease in surface free energy (from 21.4 to 12.7 mJ/m²). Compared with the surface free energy of PTFE (22 mJ/m²) by using the same testing liquids and calculated method [24], all polybenzoxazine/clay nanocomposites give lower surface energy than PTFE. Kadar [25] studied the surface free energy of the neat and organophilized clays, the uncoated layered silicates is extremely high at 257 mJ/m², while the CPC modified clay is drastically reduced at 32 mJ/m². The compatibility between the intercalated agent and polymer matrix (PP-a) is very important. Phairat et al. [26] studied the immiscibility of polybenzoxazine/clay nanocomposite and indicated that delamination of the silicate layers is strongly dependent on the compatibility between the intercalated agent and the monomer (P-a). Hence the

incorporation of CPC-modified layered silicates into the polybenzoxazine is able to help its dispersion within in the polymer matrix (PP-a).

As a result, the low surface energy must come from the incorporation of the modified long alkyl organic clay leading to chemical and topographical modification of the nanocomposites surface and enhance the hydrophobic surface property. [27]

Figure 4-3(a) and 4-3(b) present the topography and phase image of the CPC/clay10%/ polybenzoxazines (PP-a) nanocomposites, investigated by AFM. These results indicated the CPC-modified clays preferably reside on the surface and the effect of the surface roughness is present but considered to be less important.

Scheme 4-1 displays the schematic plots showing the intercalated agent of the inserting into the silicate layers via ion exchange, preparation spin coating of the CPC/clay/PP-a blending solution, and thermal treatment. Table 4-1 shows the atomic fraction of silicon by XPS analyses, indicating that the CPC-modified clays preferably reside on the surface. The surface chemical structure and composition both have significant influence on measured contact angle and resulted surface free energy of the nanocomposite. Combining our analyses of the XPS, and contact angle measurement, we speculate that the decrease the surface free energy in the present case is due to the CPC-modified clays and surface roughness.

4.4 Conclusions

A series of CPC-clay hybrids of polybenzoxazine (PP-a) have been prepared and their thermal properties and surface free energy have been characterized. The surface free energy of the CPC/clay/PP-a nanocomposites through a simple thermal treatment is significantly reduced. The lowest surface free energy obtained of the CPC/clay10%/polybenzoxazines (PP-a) is 12.6 mJ/m^2 , even lower than that of PTFE

(22.0 mJ/m²). In addition to the decrease the surface free energy of the nanocomposites and improve the thermal properties after the incorporation of 10 % organoically modified montmorillonite.



References

- [1] Coulson, S. R.; Woodward, I.; Badyal, J. P. S.; Brewer, S. A.; Willis, C. J. *Phys. Chem. B* **2000**, 104, 8836.
- [2] Jin, M.; Feng, X.; Xi, J.; Zhai, J.; Cho, K.; Feng, L.; Jiang, L. *Macromol. Rapid Commun.* **2005**, 26, 1805.
- [3] Feng, L.; Zhang, Z.; Mai, Z.; Ma, Y.; Liu, B.; Jiang, L.; Zhu, D. *Angew. Chem., Int. Ed.* **2004**, 43, 2012.
- [4] Hillborg, H.; Tomczak, N.; Olah, A.; Schonherr, H.; GVancso, G. J. *Langmuir* **2004**, 20, 785.
- [5] Wu, S. *Polymer Interface and adhesion*; Marcel Dekker: New York, **1982**.
- [6] Feiring, A. E.; Imbalzano, J. F.; Kerbow, D. L. *Adv. Fluoroplast. Plast. Eng.* **1994**, 27.
- [7] Kojima, Y.; Usuki, A.; Kawasumi, M.; Okada, A.; Kurauchi, T.; Kamigaito, O. J. *Polym. Sci. Part A: Polym. Chem.* **1993**, 31, 1755.
- [8] Pastorini, M. T.; Nunes, R. C. R. *J. Appl. Polym. Sci.* **1999**, 74, 1361.
- [9] Fu, X.; Qutubuddin, S. *Polymer* **2001**, 42, 807.
- [10] Huang, X.; Brittain, W. J. *Macromolecules* **2001**, 34, 3255.
- [11] Beyer, F. L.; Tan, N. C. B.; Dasgupta, A.; Galvin, M. E. *Chem. Mater.* **2002**, 14, 2983.
- [12] Ishida, H.; Allen, D. J. *J. Polym. Sci. Part B: Polym. Phys.* **1996**, 34, 1019.
- [13] Ishida, H.; Rodriguez, Y. *Polymer* **1995**, 36, 3151.
- [14] Wang, C. F.; Su, Y. C.; Kuo, S. W.; Huang, C. F.; Sheen, Y. C. *Chang, F. C. Angew. Chem., Int. Ed.* **2006**, 45, 2248.
- [15] Kaelble, D. H.; *Physical Chemistry of Adhesion*; Wiley Interscience: New York, **1970**.

- [16] Good, R. J.; van Oss, C. J. In *Modern Approaches to Wettability*; Schrader, M. E., Loeb, G. I., Eds.; Plenum Press: New York, **1992**; p 1.
- [17] Fowkes, F. W. In *Contact Angle, Wettability and Adhesion, Advances in Chemistry, Series No. 43*; Gould, R. F., Ed.; American Chemical Society: Washington, DC, **1964**; p 99.
- [18] Fowkes, F. W. In *Adhesion and Adsorption of Polymers, Polymer Science and Technology*; Lee, L. H., Ed.; Plenum Press: New York, **1980**; Vol. 12A, p 43.
- [19] Kaelble, D. H. *Physical Chemistry of Adhesion*; Wiley Interscience: New York, **1970**.
- [20] van Oss, C. J.; Ju, L.; Chaudhury, M. K.; Good, R. J. *J. Colloid Interface Sci.* **1989**, 128, 313.
- [21] van Oss, C. J.; Ju, L.; Chaudhury, M. K.; Good, R. J. *Chem. Rev.* **1988**, 88, 927.
- [22] Drelich, J.; Miller, J. D.; Good, R. J. *J. Colloid Interface Sci.* **1996**, 179, 37.
- [23] Good, R. J.; van Oss, C. J. *Modern Approaches to Wettability: Theory and Applications*; (Eds.: Schrader, M. E.; Loeb, G.), Plenum Press: New York, **1992**, p 1-27
- [24] Yoshimasa, U.; Takashi, N. *Langumir* **2005**, 21, 2614.
- [25] Kadar, F.; Szazdi, L.; Fekete, E.; Pukanszky, B. *Langumir* **2006**, 22, 7848.
- [26] Phiriyawirut, P.; Magaraphan, R.; Ishida, H. *Mat. Res. Innivat.* **2001**, 4, 187.
- [27] Lin, J. J.; Chu, C. C.; Chiang, L. M.; Tsia, W. C. *Adv. Mater.* **2006**, 18, 3248.

Table 4-1. Advancing contact angles, surface free energies, roughness, XPS analysis and thermal properties of polybenzoxazine/clay nanocomposites.

Sample	Contact angle (deg)			γ (mJ/m ²)	Roughness (nm)	XPS ^a (mol %)	T _g (°C)	T _d (°C)	Char Yield (600°C, %)
	H ₂ O	DIM	EG						
PPa	113.1	72.7	85.4	21.4	2.6	0	126.1	321.7	40.1
PP-a/3%Clay	110.7	84.6	85.6	15.7	20.1	6.8	134.2	325.6	44.7
PP-a/5%Clay	112.2	89.3	86.8	13.6	34.6	7.6	142.8	335.5	47.4
PP-a/10%Clay	116.4	91.4	86.2	12.7	45.1	10.9	148.7	353.2	48.1

a Silicon content (mol %).

b the decomposition temperature (T_d) of the 5 % weight loss.

Scheme 4-1. Representation of the intercalated agent was inserted into the silicate layers via ion exchange and preparation of polybenzoxazine nanocomposites by thermal treatment.

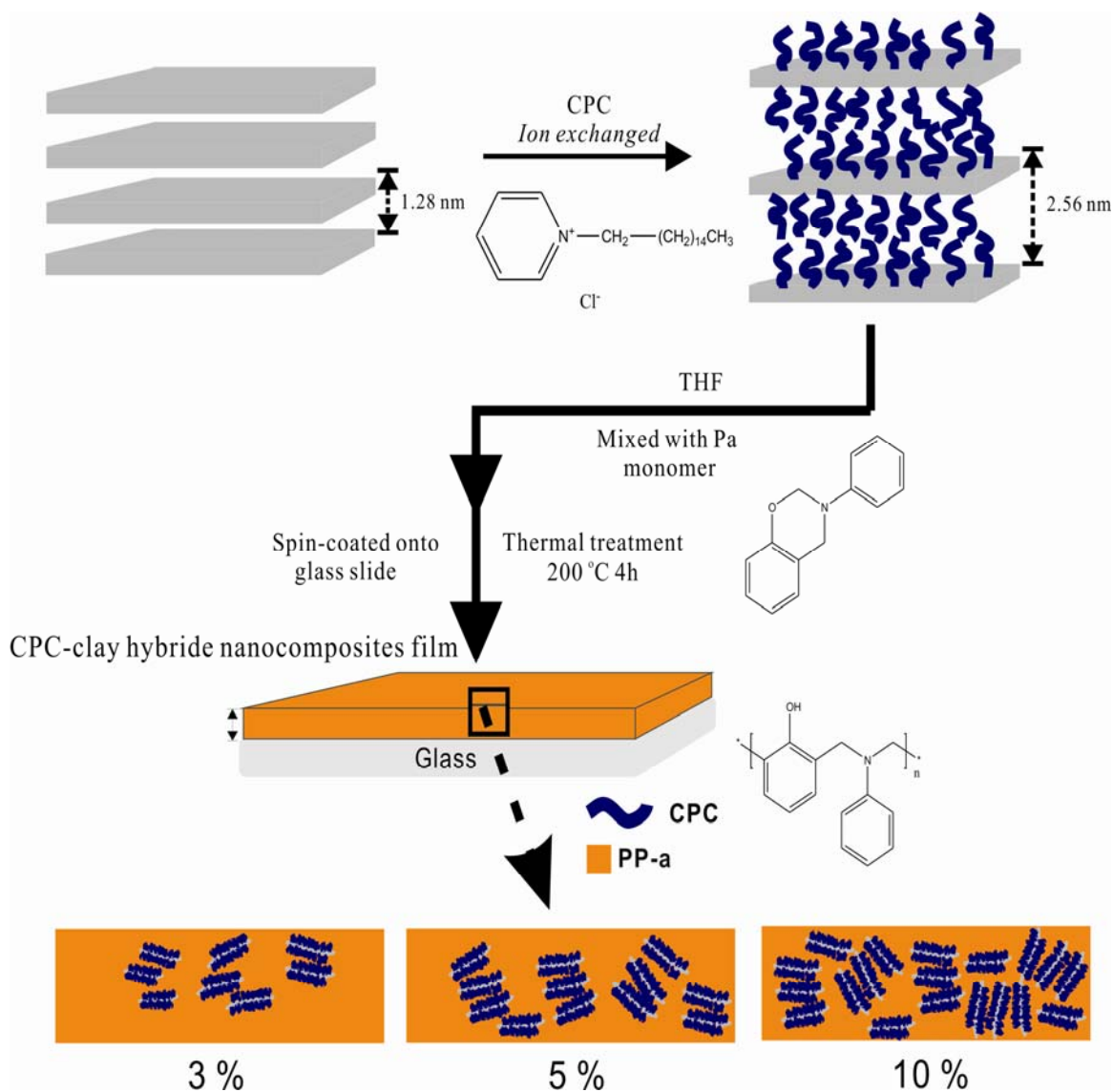


Figure 4-1. X-ray diffraction patterns of (a) pure clay, and (b) CPC/clay, (c) PP-a/Clay 3 wt%, (d) 5 wt%, (e) 10 wt%.

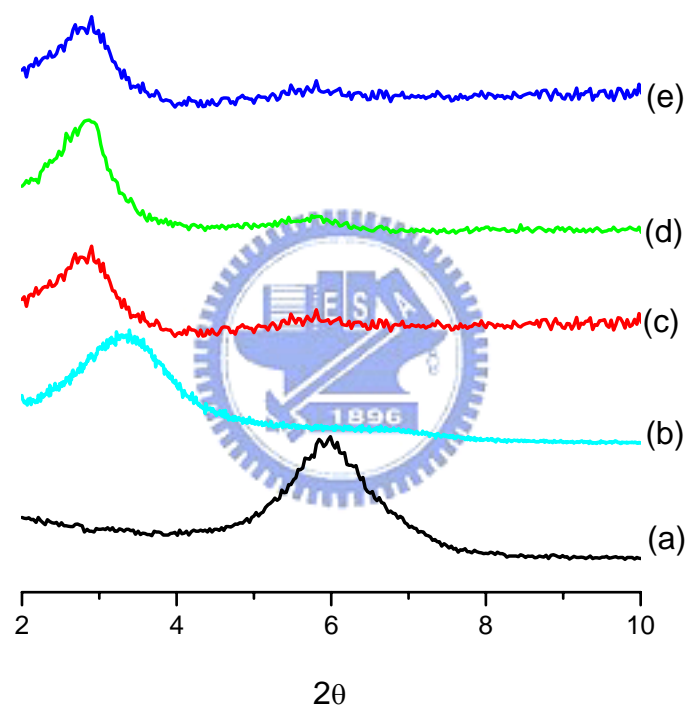


Figure 4-2. TEM micrographs of the polybenzoxazines (PP-a) nanocomposites containing 3 wt % clay: (left) low magnification, and (right) high magnification.

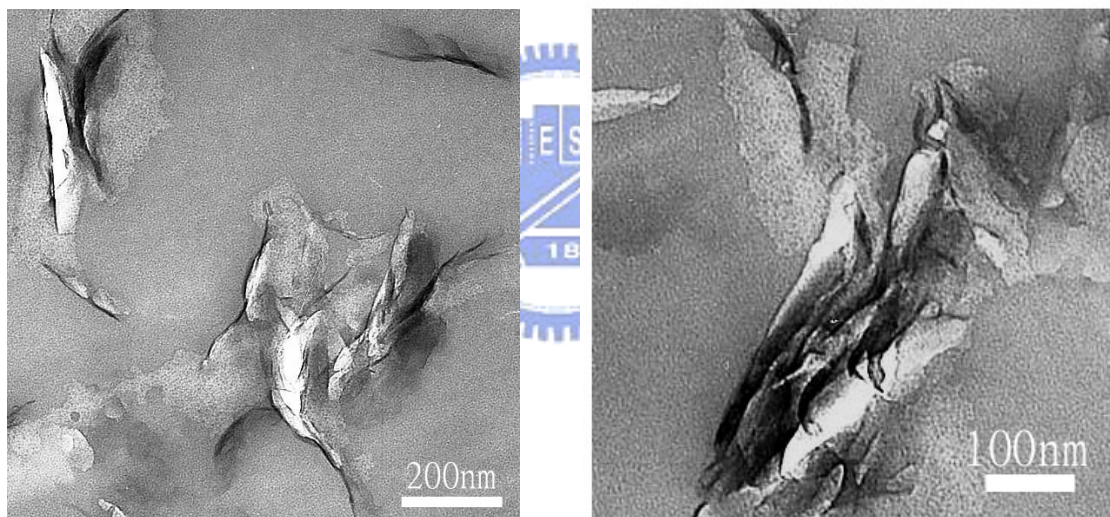
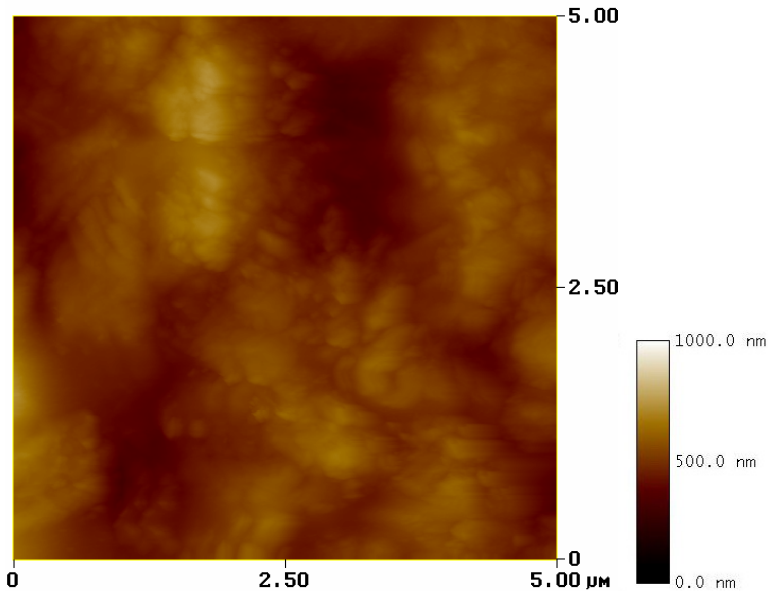
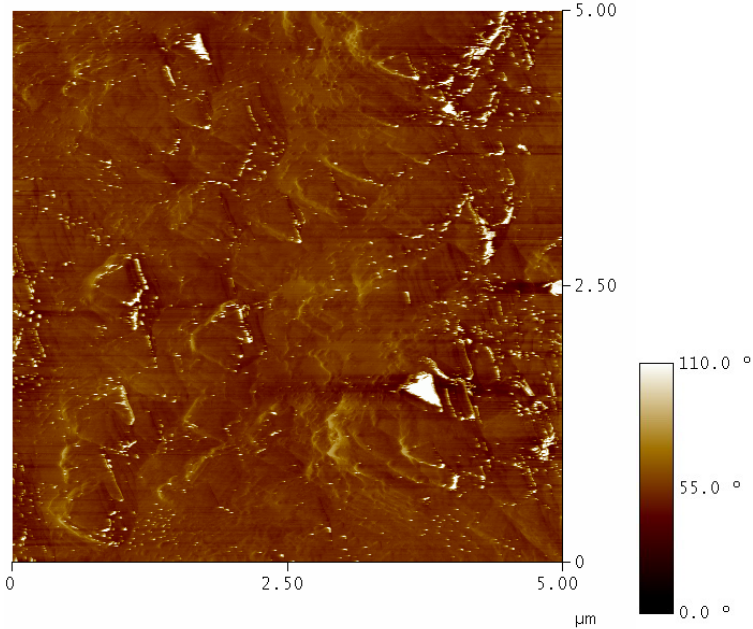


Figure 4-3. AFM images of CPC/ Clay 10% /PP-a: (a) Topography image, and (b)

Phase image.



(a)



(b)

Chapter 5

Preparation of the Stimuli-Responsive ZnS/PNIPAM

Hollow Spheres

Abstract

Novel quantum dots ZnS/poly(N-isopropylacrylamide) (PNIPAM) hybrid hollow spheres were obtained by localizing free radical polymerization of NIPAM and crosslinker (MBA) at the peripheral of PCL nanoparticles, followed by biodegradation of PCL with an enzyme of the Lipase PS. The formation of ZnS/PNIPAM hollow spherical structures and the thermo-sensitive reversible properties was systematically investigated by transmission electron microscopy (TEM) and dynamic light scattering (DLS), respectively. The ZnS/PNIPAM hollow spheres possess the photoluminescence properties and a swelling and de-swelling at about 32 °C, which agrees well with the slight red-shift in photoluminescence spectra.

5.1 Introduction

Novel materials based on colloidal semiconductor nanocrystals (quantum dots, QDs) have attracted considerable attention in recent years for their special electronic and optical properties coming from quantum confinement effect [1–12]. Most synthetic procedures involved for colloids or capped free-standing powders yield crystallites with a relatively larger size distribution. As a result, a capping agent such as mercaptoethanol has been used to covalently bond on the surface atoms of the nanocrystallites, making them stable under normal atmospheric condition [13–14]. Zinc sulfide (ZnS), a II-VI group semiconductor, is particularly suitable for use as host material for large variety of dopants because of its 3.7 eV band gap [15], and is widely used in flat panel displays, infrared windows, sensors, etc. Nanostructured doped ZnS materials have many applications because of their superior luminescence characteristics compared to their bulk counterparts [8, 16–18]. Embedding QDs nanocrystals into polymer matrices is an effective method of enhancing the optical properties of these materials [19]. Zhang [20–21] and Bai et al. [22] have reported the syntheses of polymer composites containing QDs from different polymer matrices.

In addition, stimuli-responsive polymers have attracted great interest for their physical or chemical changes in response to external changes in environmental conditions such as temperature, pH, ionic strength, and electromagnetic radiation [23]. Poly(N-isopropyl acrylamide) (PNIPAM) is a well-known example which undergoes a sharp coil–globule transition in water at 32 °C, changing from a hydrophilic state below this temperature and a hydrophobic state above it [24]. Temperature at the lower critical solution temperature (LCST) corresponds to the region in the phase diagram where the enthalpic contribution of water hydrogen-bonded to the polymer chain becomes less than the entropic gain of the system as a whole and thus is largely

dependent on the hydrogen-bonding capabilities of the constituent monomer units.

Furthermore, biocompatible, biodegradable and non-toxic synthetic aliphatic polyesters, such as poly(ϵ -caprolactone) (PCL), are very useful in biomedical applications, especially as drug delivery devices [25], because they are completely biodegradable inside the body after its interaction with body fluid, enzyme and cells. Lipase pseudomonas is able to accelerate the biodegradation of PCL, and completed after 6 h in a buffer solution containing the enzyme. Jiang et al [26]. reported that the PCL/PNIPAM core-shell particles were obtained by localizing the polymerization around the PCL nanoparticles then followed by degrading the PCL core with enzyme. The hollow spheres are thermosensitive and display a reversible swelling and de-swelling behavior at 32 °C.

In our previous study [27], we reported a simple route to hierarchical ZnS nanoparticle/polymer nanofiber structures through self-assembly of zinc dimethacrylate ($\text{Zn}(\text{MA})_2$) in water/ethanol solution by combined use of γ -irradiation polymerization and gas/solid reaction. In this study, we would like to combine the ZnS QDs with PCL/PNIPAM core-shell particles through the AIBN initiated free radical polymerization and then followed by biodegradation of the PCL cores using a commercially enzyme to form hollow spheres. The photoluminescence properties of the ZnS/PNIPAM hollow spherical materials of the thermal sensitive polymer can be mediated by temperature changes.

5.2 Experimental

5.2.1 Materials

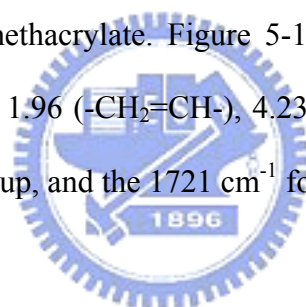
N-isopropylacrylamide (NIPAM) and methacryloyl chloride (stabilized with MEHQ) were obtained from the Tokyo Chemical Industrial CO., Ltd. *N*-isopropylacrylamide monomer (NIPAm) was recrystallized from hexanes and dried in vacuum prior to use. Most chemicals used in this study, including 2-mercaptoethanol, amano Lipase PS from *Pseudomonas cepacia*, phosphate buffer solution 0.1 M, *N,N'*-Methylenebis(acrylamide) (MBA), sodium sulfide nonahydrate ($\text{Na}_2\text{S} \cdot 9\text{H}_2\text{O}$) were acquired from the Aldrich Chemical Co., Inc. 4-Dimethylaminopyridine (DMAP), and zinc acetate dehydrate ($\text{C}_4\text{H}_6\text{O}_4\text{Zn} \cdot 2\text{H}_2\text{O}$) were obtained from Acros Organics, USA. 2,2'-Azobis-isobutyronitrile (AIBN), and NaHCO_3 were purchased from Showa, Toyko. *N,N*-Dimethylformamide (DMF), tetrahydrofuran(THF), and methanol were purchased from the TEDIA Company. The THF was distilled from finely ground CaH_2 before use.

5.2.2 Preparation of the prepolymers of poly(ϵ -caprolactone)

Tempo-OH (0.0728 g, 2.5×10^{-4} mol) in toluene (5 mL) and 0.2 mL of a toluene solution of triethylaluminum (0.1 mol/L) were mixed under an argon atmosphere. The reaction mixture was stirred at room temperature for 30 min and then allowed to evaporate to remove the byproduct 2-propanol. After repeating this procedure several times, 25 ml dry toluene and 5 ml caprolactone (0.044 mol) were added to the reaction mixture in ice bath. The polymerization was carried out at 25 °C for 24 h under argon and was terminated by adding excess acetic acid (0.2 mL acetic acid/0.8 ml toluene). Two-thirds of the initial solvent was evaporated, and the residue was precipitated into methanol. The product was dried to constant weight under vacuum.

5.2.3 Synthesis of the capping agent 2-mercaptoethyl methacrylate

The capping agent was synthesized through the reaction of 2-mercaptoethanol and methacryloyl chloride using DMAP as catalyst, as shown in Scheme 5-1. The solution of 2-mercaptoethanol (0.1 mol), methacryloyl chloride (0.12 mol), and DMAP (0.12 mol) in tetrahydrofuran (300 mL) was stirred at room temperature until the reaction was completed. The solid by-products were removed by filtration. The solvent was removed in a rotary evaporator at room temperature and the resulted crude product was purified by dissolving in ether and washed several times with NaHCO₃ solution and distilled water. The purified product in ether solvent was dried with anhydrous sodium sulfate, followed by evaporation of the ether under vacuum to afford the 2-mercaptoethyl methacrylate. Figure 5-1 shows the ¹H NMR spectrum (CDCl₃, δ= ppm): 6.09, 5.56, 1.96 (-CH₂=CH-), 4.23, 3.21 (-O-CH₂-CH₂-), 1.1(-SH). FT-IR: 1668 cm⁻¹ for C=C group, and the 1721 cm⁻¹ for C=O group.



5.2.4 Preparation of ZnS nanoparticle peripherally with methacrylate

The thio-capped ZnS nanoparticles were prepared through the reaction of zinc acetate dihydrate (0.01 mol) and 2-mercaptoethyl methacrylate (0.003 mol) in 150 mL of methanol. Na₂S dissolved in a mixture of 40 mL of water and 40 mL of methanol was added and the resulting suspension was stirred for 1 day under nitrogen. The white precipitate was separated by centrifugation (15000 rpm, 20 min) and the powder sample was dried under vacuum at room temperature.

5.2.5 Synthesis of QDs hollow spheres

The preparation of QDs hollow spheres procedure is shown in Scheme 5-2. The initiator (AIBN, 0.011 g) and PCL (Mw ~ 37890 g/mol, 0.1 g) were dissolved in DMF

(10 mL) and then the solution was added dropwise into deionized water (80 mL). The solution was stirred continually for 1 h then the NIPAM monomer (0.5 g), ZnS nanoparticle (0.1 g) and MBA crosslinker (0.068 g) were added into the suspension solution. The reaction was carried out for 4 h at 80 °C under nitrogen. The ZnS/PNIPAM hollow spheres were prepared by using lipase PS to degrade PCL core. The Lipase PS was purified by dissolving it in a 0.1 M phosphate buffer solution. The solution was stirred at 50 °C for 6 h and then the hollow spheres were separated by centrifugation (15000 rpm, 10 min), washed by deionized water for several times.



5.3 Characterizations

Wide-angle X-Ray diffraction (WAXD) spectrum was recorded on powdered sample using a Rigaku D/max-2500 type X-ray diffraction instrument. The radiation source used was Ni-filtered, Cu K α radiation ($\lambda=1.54\text{\AA}$). The sample was mounted on a circular sample holder, the scanning rate was $0.6^\circ/\text{min}$ from $2\theta= 3$ to 20 . Transmission electron microscopy (TEM) images were obtained using a Hitachi H-7500 instrument with an accelerating voltage of 100 kV. The TEM samples were deposited from the ZnS/PNIPAM hollow spheres onto the carbon-coated copper grids. Molecular weights and molecular weight distributions were determined by gel permeation chromatography (GPC) using a Waters 510 HPLC equipped with a 410 Differential Refractometer, a refractive index (UV) detector, and three Ultrastyrigel columns (100, 500, and 10^3 Å) connected in series in order of increasing pore size. The molecular weight calibration curve was obtained using polystyrene standards. ^1H NMR spectroscopic analyses were performed using a Varian Uniytinova-500 NMR Spectrometers at 500 MHz. All spectra were recorded using CDCl_3 as the solvent and TMS as the external standard. Fourier transformation infrared (FT-IR) spectra were recorded at 25°C using a Nicolet AVATAR 320 FT-IR spectrometer; the sample was cast onto KBr pellets from CHCl_3 solution. All FT-IR spectra were obtained within the range $4000\text{-}400\text{ cm}^{-1}$; 32 scans were collected at a resolution of 1 cm^{-1} while samples were purged with nitrogen to ensure that the films remained. Dynamic Light Scattering (DLS) measurements were performed on a Brookhaven 90 plus model equipment (Brookhaven Instruments Corporation, USA) with a He-Ne laser with a power of 35 mW at 632.8 nm. The temperature was controlled by heating and cooling process, and the measurements were done at an angle of 90° . Photoluminescence (PL) excitation and emission spectra were collected at room temperature using a

monochromatized Xe light source.

5.4 Results and discussion

Figure 5-2 (a) shows infrared spectroscopy of pure PCL prepared by TEMPO polymerization, where the absorption peaks of carbonyl group of pure PCL are at 1724 cm^{-1} and 1734 cm^{-1} corresponding to crystalline and amorphous phases, respectively. A new absorption of the ZnS/PCL/PNIPAM at 1655 cm^{-1} is attributed to the carbonyl amide group of PNIPAM, indicating the formation of PCL/PNIPAM core-shell spheres. The enzyme of Lipase PS is known to be the degradation enzyme for PCL [28], and it was used as the biocatalyst to degrade the PCL cores in this study. Apparently, the absorption peak of the carbonyl group at 1724 cm^{-1} of PCL was totally disappeared, indicating that the PCL cores were biodegraded completely by using the enzyme of Lipase PS while the absorption at 1655 cm^{-1} of PNIPAM was still remained as shown in Figure 5-2 (c), showing the formation of the hollow spheres with QDs.

Figure 5-3 shows X-ray diffraction patterns of the ZnS nanocrystallites (a) and ZnS/PNIPAM hollow spheres (b). The three broadened peak positions appeared at 2θ value 29.5° , 48.9° , and 55.1° correspond to the (110), (220), and (311) planes of the cubic crystalline ZnS as shown in Figure 5-3 (a). An average crystallite size was estimated as ca. 2.7 nm, according to the line width analysis of the (110) diffraction peak based on Debye-Scherrer formula [29], given by $L = \frac{0.9\lambda}{B \cos \theta}$. L is the coherence length related to particle diameter $D=3/4 L$, B is the full width at the half maximum (FWHM) of the peak (110), λ is the wavelength of the X-ray radiation, and θ is the angle of diffraction. In addition, the ZnS/PNIPAM hollow spheres show the similar diffraction pattern as the pure ZnS nanocrystallites except showing strong

PNIPAM amorphous halo around 20° , indicating the successful introducing the ZnS QDs within the PNIPAM hollow sphere matrix.

Figure 5-4 shows TEM images of the PNIPAM and ZnS/PNIPAM hollow spheres. In Figure 5-4 (a), the image of PNIPAM hollow spheres shows no internal structure, indicating the degradation of PCL core, which is consistent with previous study by Jiang et al [26]. The TEM image of the ZnS/PNIPAM hollow spheres in Figure 5-4 (b) reveals that dense ZnS nanoparticles having diameters of ca. 3–4 nm are well dispersed within the PNIPAM hollow shells. The selective-area electron diffraction (SAED) pattern (inset to Figure 5-4 (b)) corresponds to the (111), (220), and (311) planes of crystalline ZnS, indicating that these ZnS nanoparticles in the PNIPAM hollow shells possessing zinc blende crystal structure as the results of X-ray diffraction patterns [Figure 6-3].

Dynamic light scattering (DLS) was employed to determine the hydrodynamic diameters ($\langle D_h \rangle$) of the ZnS/PNIPAM hollow spheres and their temperature-responsive swelling and de-swelling behavior. As shown in Figure 5-5, as the temperature increased from 20 to 50 °C, the average hydrodynamic diameter of the ZnS/PNIPAM hollow spheres decreased from 544 to 317 nm, corresponding to the “swelling” and “de-swelling” states of the crosslinked PNIPAM shell, respectively. These ZnS/PNIPAM hollow spheres clearly display dimensional change with temperature, implying that volumes of these PNIPAM hollow shells can shrink or swell with temperature changes. Most importantly, the reversibility of the size dependence of the hollow shells in the heating process coincides with that in the cooling process. Furthermore, after a cycle of the temperature increase and decrease, the hollow sphere size returns to its starting value.

In addition, PLE results indicate that excitation spectrum of the 0.3-ZnS and

0.6-ZnS nanoparticles are 317 and 326 nm. The number of the 0.3 indicates the mole ratio of the ZnS and capping agent. Figure 5-6 showing a slight red shift compared with higher capping agent content. The emission peak for the 0.3-ZnS and 0.6-ZnS are 426 and 425 nm, respectively. PL maximum peak was slightly blue shifted (about 14 nm) relative to that of bulk ZnS (440 nm) and thus exhibiting quantum size effect [30-31].

Poly(N-isopropylacrylamide) (PNIPAM) is a well-known thermoresponsive polymer exhibiting a coil-globule transition in aqueous at a lower critical solution temperature (LCST) of around 32 °C [32-33]. Yubai [22] et al. reported that photoluminescence intensities of the PNIPAM/CdTe gels decrease with the increase of temperature. It can be seen the PL intensities of the hollow spheres decreases with the increase of temperature. In the polymer phase transition regime, hydrogen bonds between side groups and water molecules are broken, and PNIPAM undergoes changes in conformation on increasing temperature. At higher temperature above LCST, the PL intensity of 0.3-ZnS/PNIPAM hollow spheres is lower because of the QDs in the PNIPAM hollow spheres shrink due to the increase of hydrophobicity at temperatures above LCST. As a result, these ZnS nanoparticles become closer and closer or even contact each others. Below the LCST, the PL intensity of ZnS/PNIPAM hollow spheres is higher, indicating that these ZnS QDs are well dispersed and separated in the PNIPAM matrix. From the PL results, the peak position of the ZnS/PNIPAM hollow spheres shows slight red shift with the increase of temperature, as shown in Figure 5-7. Similar results have been reported that the PL peaks of the CdTe nanocrystals shift to longer wavelengths with larger particles [34].

5.5 Conclusions

The novel inorganic/organic nano-spheres, (ZnS/PCL/PNIPAM), were successfully prepared by a simple free radical polymerization method. After locking the sphere structure by the cross-linking with the MBA, the core was degraded with Lipase PS, and the ZnS/PNIPAM hollow spheres can be obtained. The ZnS/PNIPAM hollow sphere possesses reversible thermo-sensitive properties and its hydrodynamic diameter ($\langle D_h \rangle$) is sensitive to the temperature stimuli response. Furthermore, slight red-shift of maximum PL wavelengths was observed. The hollow spheres of the ZnS/PNIPAM have the potential applications in QDs-based biosensors and devices.

Acknowledgments

The authors thank the National Science Council, Taiwan, for financially supporting this research under Contract NSC-96-2120-M-009-009.



References

- (1) Tagaya, A.; Ohkita, H.; Mukoh, M.; Sakaguchi, R.; Koike, Y. *Science* **2003**, 301, 812.
- (2) Kasai, H.; Nalwa, H. S.; Oikawa, H.; Okada, S.; Matsuda, H.; Minami, N.; Kakuta, A.; Ono, K.; Mukoh, A.; Nakanishi, H. *Jpn. J. Appl. Phys. Part 1* **1992**, 31, L1132.
- (3) Fujita, S.; Kasai, H.; Okada, S.; Oikawa, H.; Fukuda, T.; Matsuda, H.; Tripathy, S. K.; Nakanishi, H. *Jpn. J. Appl. Phys. Part 1* **1999**, 3, L659.
- (4) Okada, S.; Matsuda, H.; Nakanishi, H.; Kato, M.; Muramatsu, S. *Jpn Patent Application* **1982**, 61-192 404.
- (5) Okada, S.; Matsuda, H.; Nakanishi, H.; Kato, M.; Muramatsu, R. *Jpn Patent* 716 929, **1992**.
- (6) Nakanishi, H.; Matsuda, H.; Okada, S.; Kato, M. *Mater. Res. Soc. Int. Mtg. Adv. Mater.* **1989**, 1, 97.
- (7) Marder, S. R.; Perry, J. W.; Schaefer, W. P. *Science* **1989**, 245, 626.
- (8) Bhargava, R. N.; Gallagher, D.; Hong, X.; Nurmikko, A. *Phys. Rev. Lett.* **1994**, 72, 416.
- (9) Schmidt, T.; Muller, G.; Spanhel, L.; Kerkel, K.; Forchel, A. *Chem. Mater.* **1998**, 10, 65.
- (10) Sapra, S.; Prakash, A.; Ghangrekar, A.; Periasamy, N.; Sarma, D. D. *J. Phys. Chem. B* **2005**, 109, 1663.
- (11) Chen, W.; Malm, J. O.; Zwiller, V.; Wallenberg, R.; Bovin, J. O. *J. Appl. Phys.* **2001**, 89, 2671.
- (12) Hines, M. A.; Sionnest, P. G. *J. Phys. Chem.* **1996**, 100, 468.
- (13) Huang, F.; Zhang, H.; Banfield, J. F. *J. Phys. Chem. B* **2003**, 107, 10470.
- (14) Vogel, W.; Borse, P. H.; Deshmukh, N.; Kulkarni, S. K. *Langmuir* **2000**, 16,

2032.

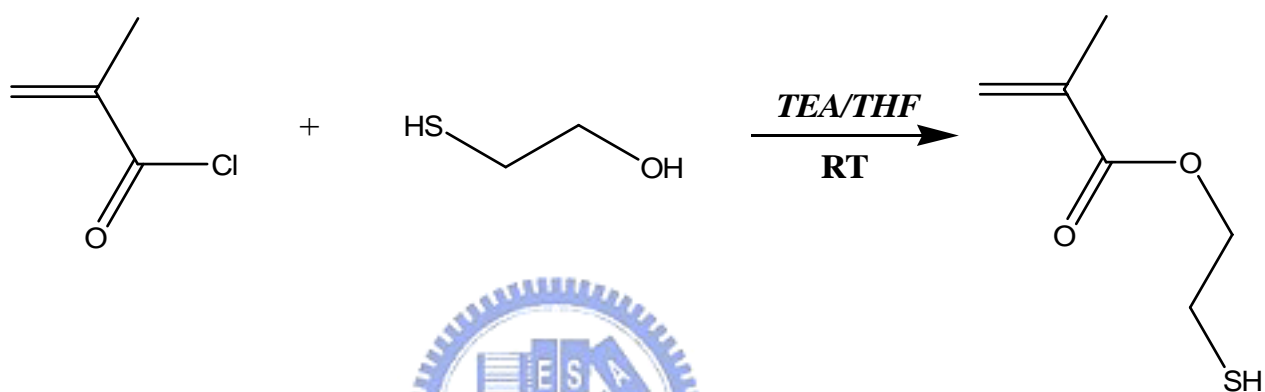
- (15) Ding, J. X.; Zapien, J. A.; Chen, W. W.; Lifshitz, Y.; Lee, S. T.; Meng, X. M. *Appl. Phys. Lett.* **2004**, 85, 2361.
- (16) Sooklal, K.; Cullum, B. S.; Angel, S. M.; Murphy, C. J. *J. Phys. Chem.* **1996**, 100, 4551.
- (17) Suyver, J. F.; Wuister, S. F.; Kelly, J. J.; Meijerink, A. *Nano. Lett.* **2001**, 1, 429.
- (18) Dinsmore, A. D.; Hsu, D. S.; Gray, H. F.; Qadri, S. B. Tian, Y.; Ratna, B. R. *Appl. Phys. Lett.* **1999**, 75, 802.
- (19) Xu, S.; Zhang, J.; Paquet, C.; Lin, Y.; Kumacheva, E. *Adv. Funct. Mater.* **2003**, 13, 468.
- (20) Ye, J.; Hou, Y.; Gui, Z.; Zhang, G. *Langmuir* **2008**, 24, 2727.
- (21) Hou, Y.; Ye, J.; Gui, Z.; Zhang, G. *Langmuir* **2008**, 24, 9682.
- (22) Li, J.; Hong, X.; Liu, Y.; Li, D.; Wang, Y.; Li, J.; Bai, Y.; Li, T. *Adv. Mater.* **2005**, 17, 163.
- (23) Gil, E. S.; Hudson, S. M. *Prog. Polym. Sci.* **2004**, 29, 1173.
- (24) Schild, H. G. *Prog. Polym. Sci.* **1992**, 17, 163.
- (25) Wang, Y.; Tang, L.; Sun, T.; Li, C.; Xiong, M.; Wang, J. *Biomacromolecules* **2008**, 9, 388.
- (26) Zhang, Y.; Jiang, M.; Zhao, J.; Ren, X.; Chen, D.; Zhang, G. *Adv. Funct. Mater.* **2005**, 15, 695.
- (27) Kuo, S. W.; Chang, F. C. *J. Phys. Chem. C* **2008**, 112, 16470.
- (28) Nie, T.; Zhao, Y.; Xie, Z.; Wu, C. *Macromolecules* **2003**, 36, 8825.
- (29) Guinier, A. *X-ray Diffraction*; Free man: San Francisco, CA, **1963**.
- (30) Yin, X. J.; Yan, J.; Zhi, L. Z.; Xu, S. H. *J. Cryst. Growth* **1998**, 191, 692.
- (31) Ghosh, G.; Naskar, M. K.; Patra, A.; Chatterjee, M. *Opt. Mater.* **2006**, 26, 1047.

(32) Otake, K.; Inomata, H.; Konno, M.; Saito, S. *Macromolecules* **1990**, 23, 283.

(33) Kubota, K.; Fujishige, S.; Ando, I. *J. Phys. Chem.* **1990**, 94, 5154.

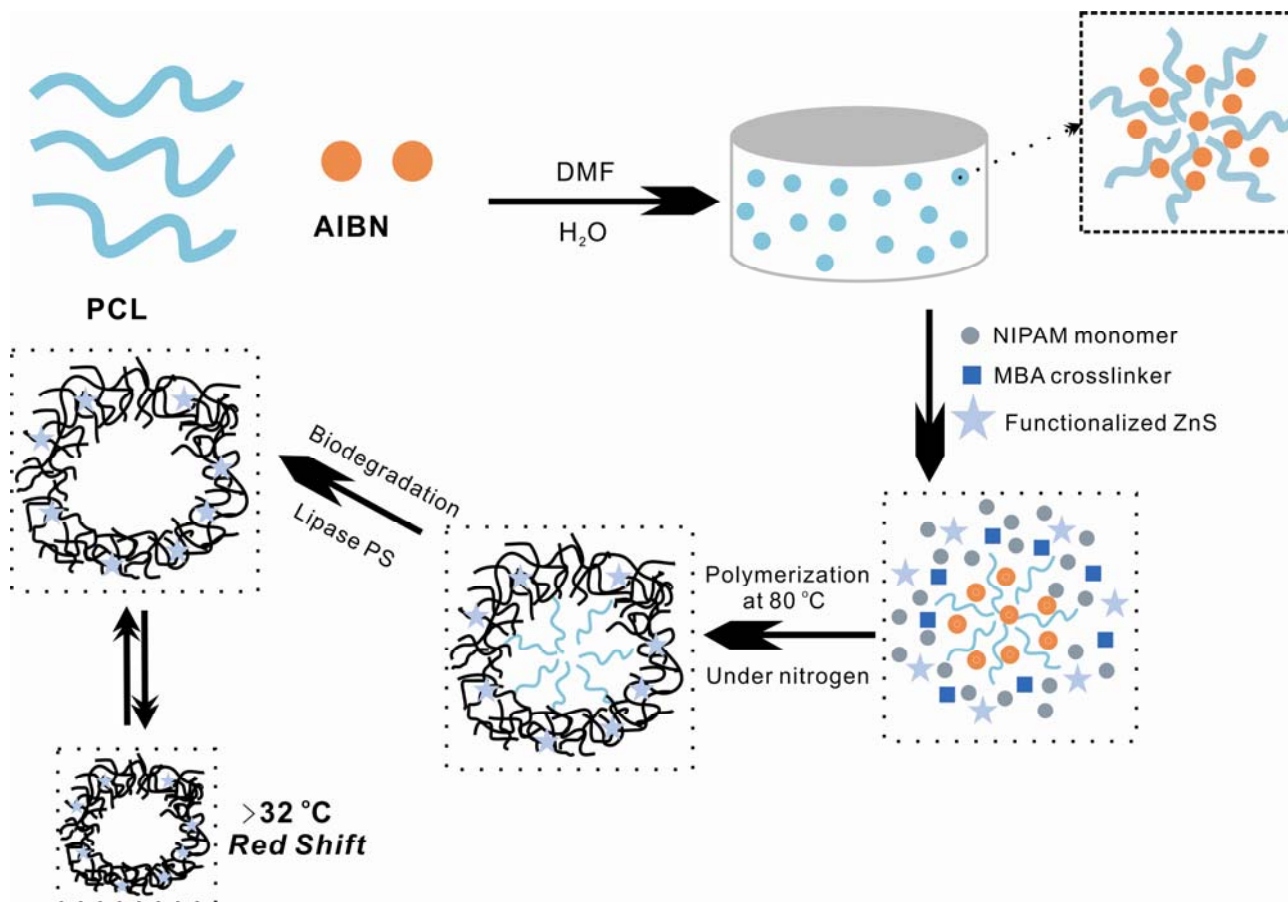
(34) Peng, Z. A.; Peng, X. G. *J. Am. Chem. Soc.* **2001**, 123, 1389.





Scheme 5-1. Synthesis of the capping agent of 2-mercaptoethyl methacrylate.

Scheme 5-2. Representation of the photoluminescence hollow sphere preparation and temperature responsive.



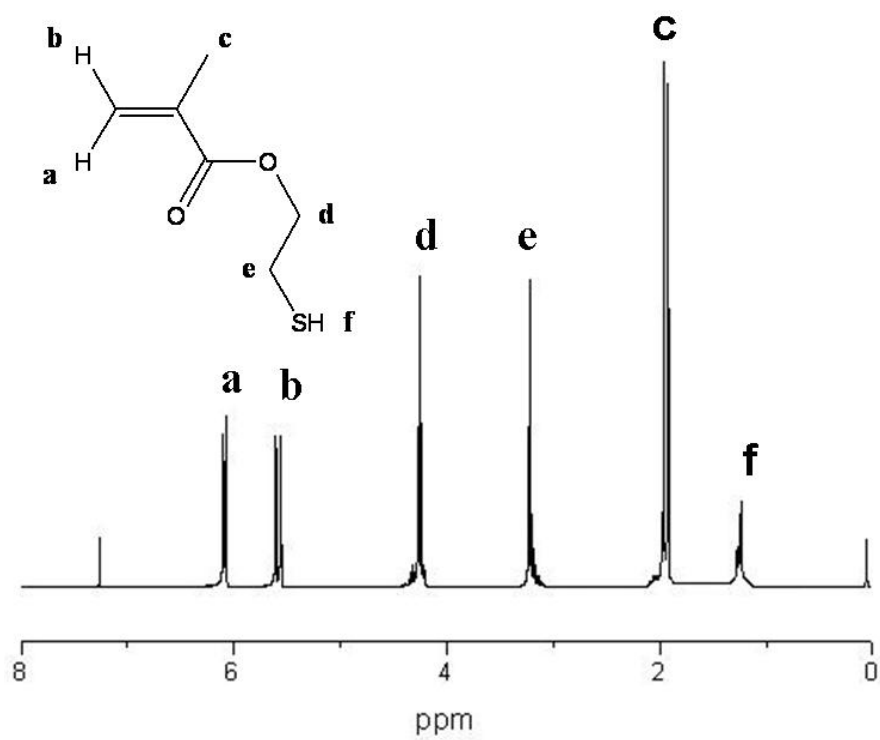


Figure 5-1. The ¹H NMR spectrum for 2-mercaptoethyl methacrylate.

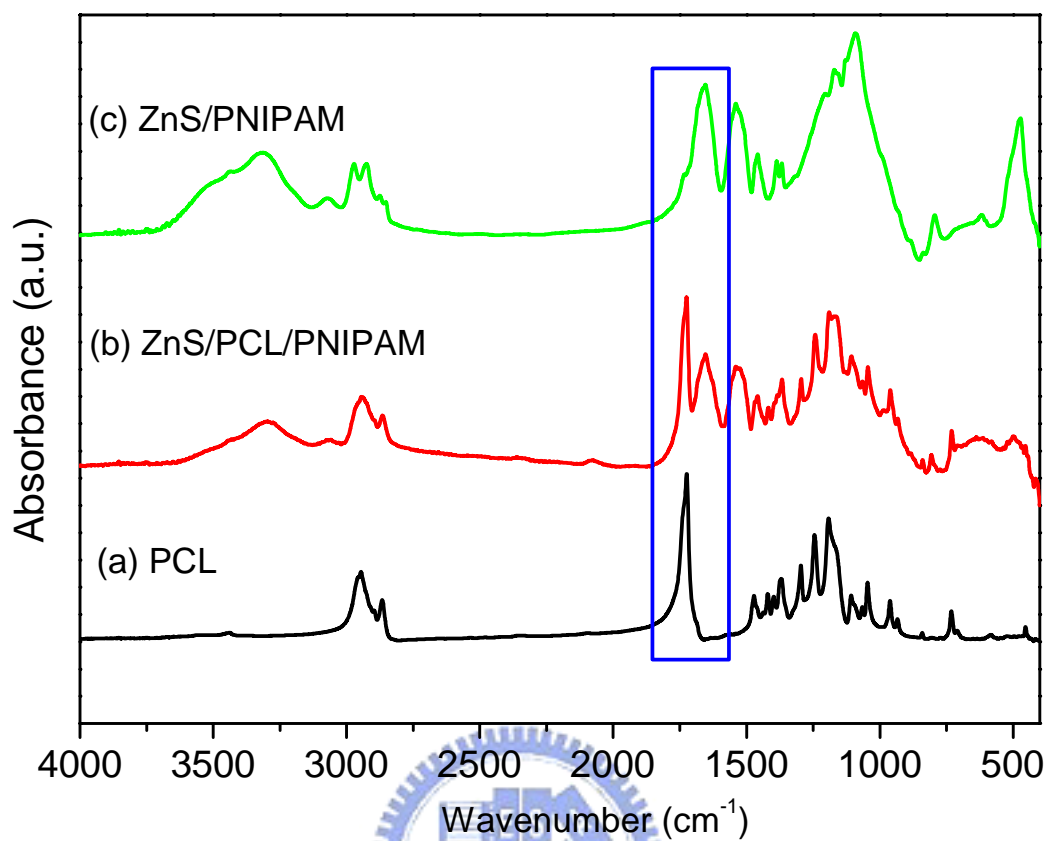


Figure 5-2. FT-IR spectra of the (a) PCL, (b) ZnS/PCL/PNIPAM spheres, and (c) ZnS/PNIPAM hollow spheres.

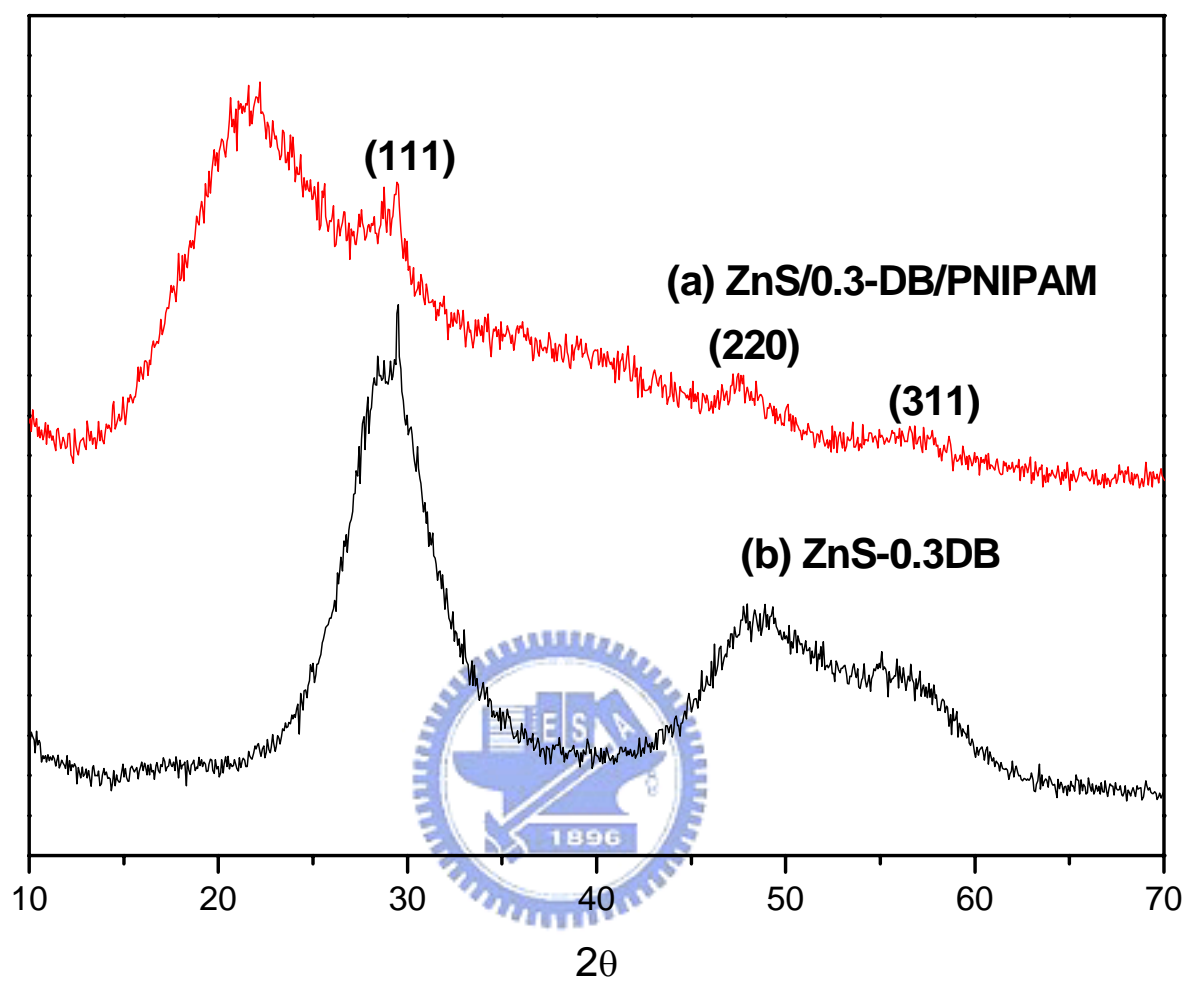


Figure 5-3. X-ray diffraction patterns of the (a) ZnS nanoparticle and (b) ZnS/PNIPAM hollow spheres.

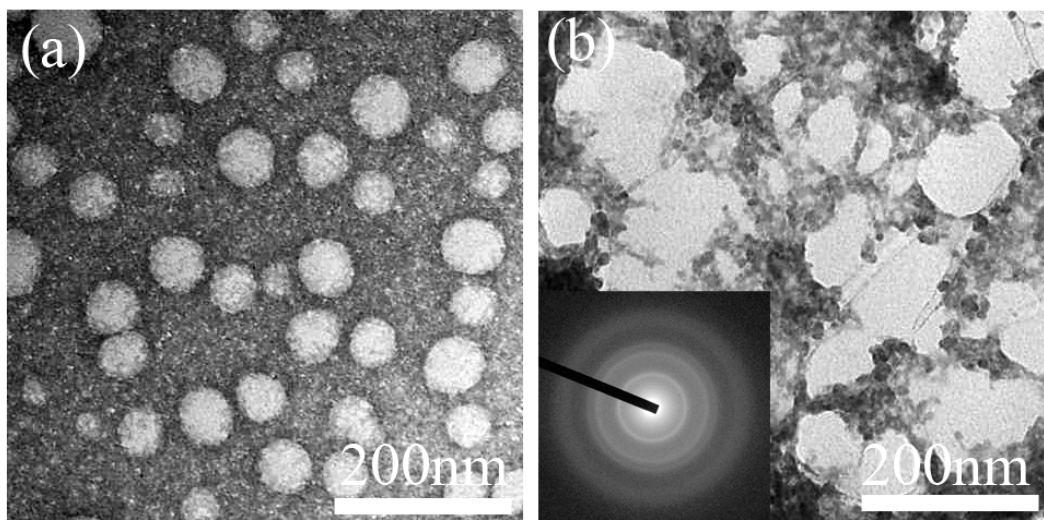


Figure 5-4. TEM image and electron diffraction pattern of the (a) PNIPAM hollow spheres, (b) ZnS/PNIPAM hollow spheres.

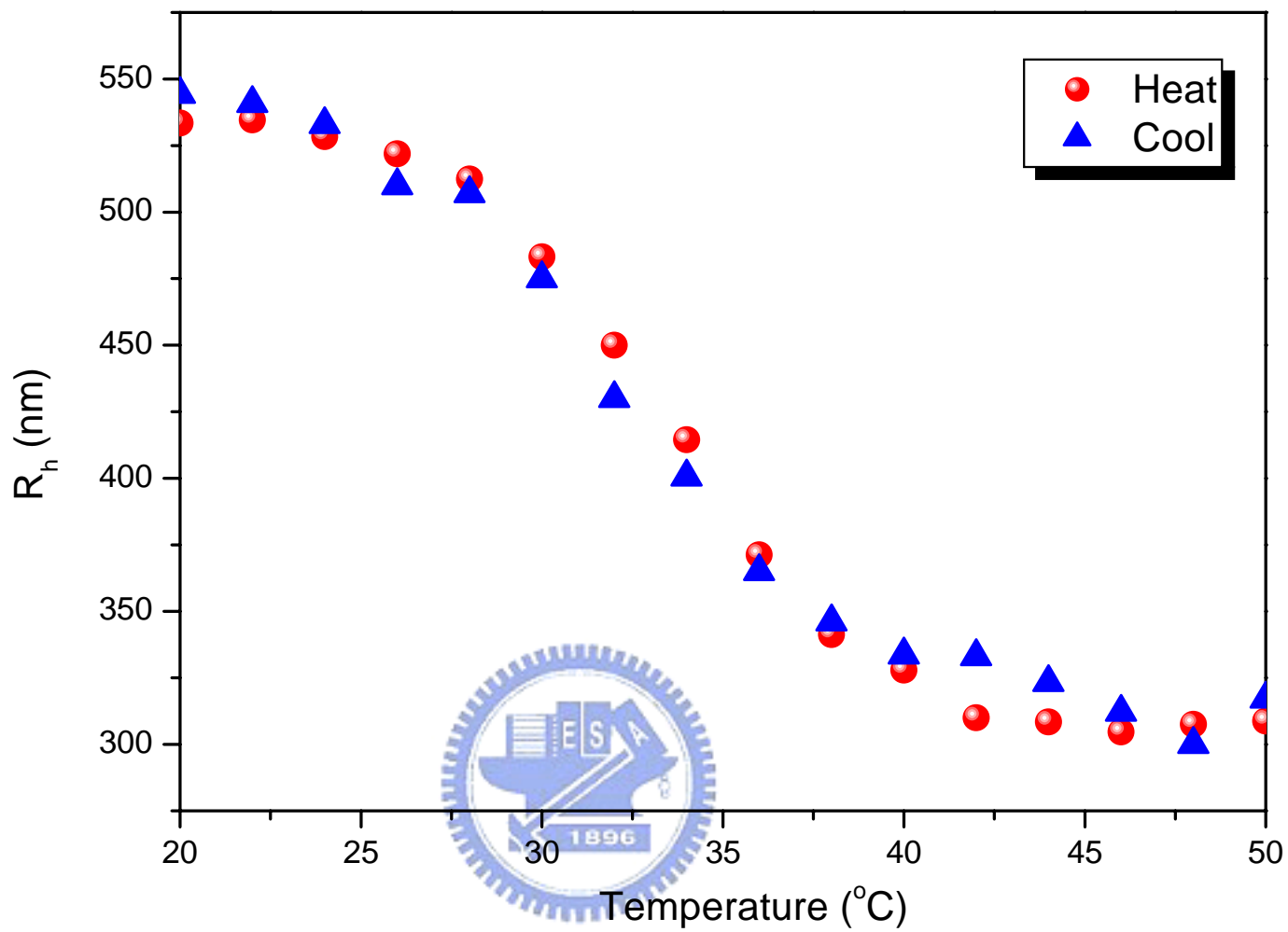


Figure 5-5. Variation of average hydrodynamic diameters (D_h) vs. temperature of the ZnS/PNIPAM hollow spheres.

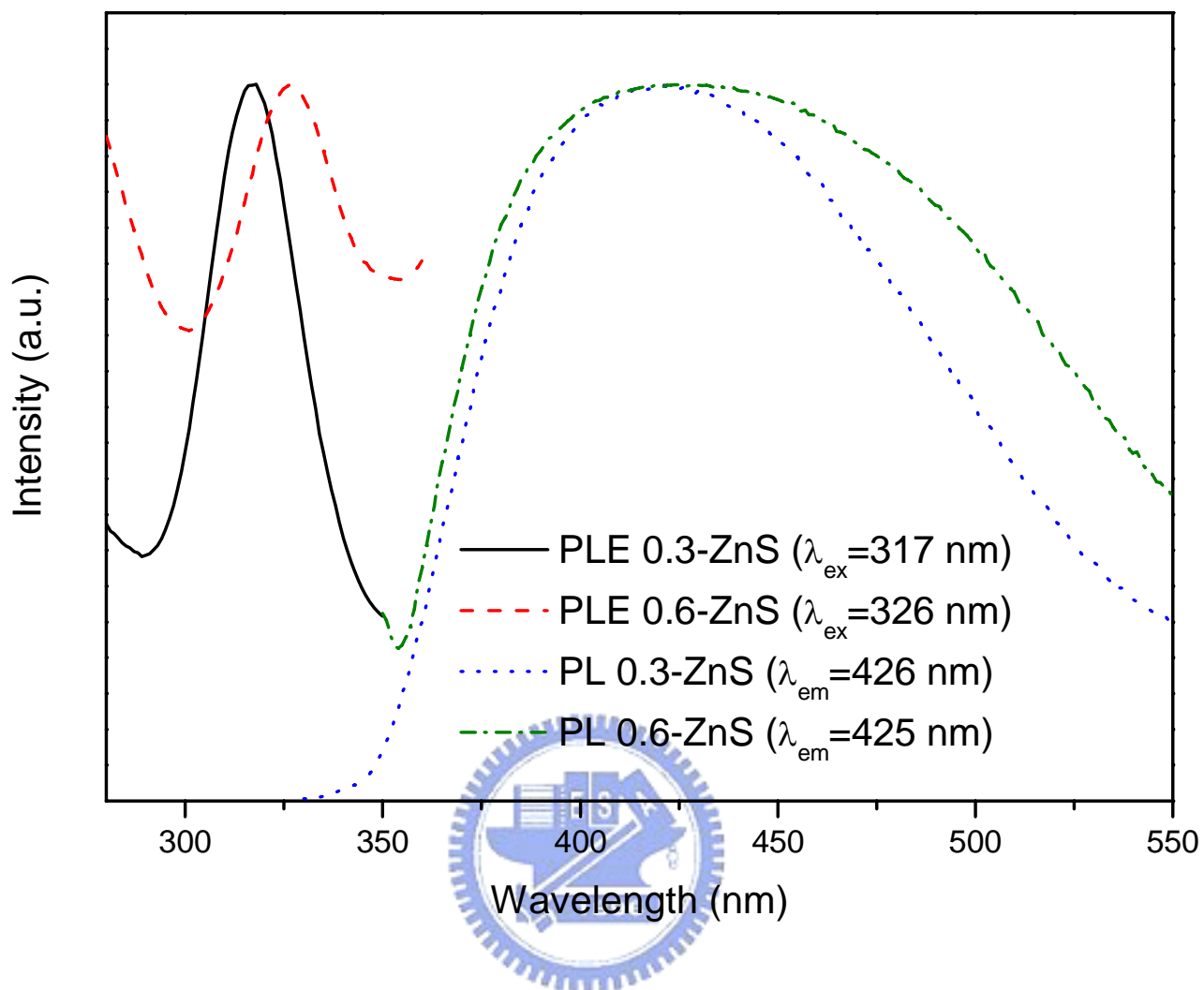


Figure 5-6. PLE and PL spectrum of the 0.3-ZnS and 0.6-ZnS nanoparticles.

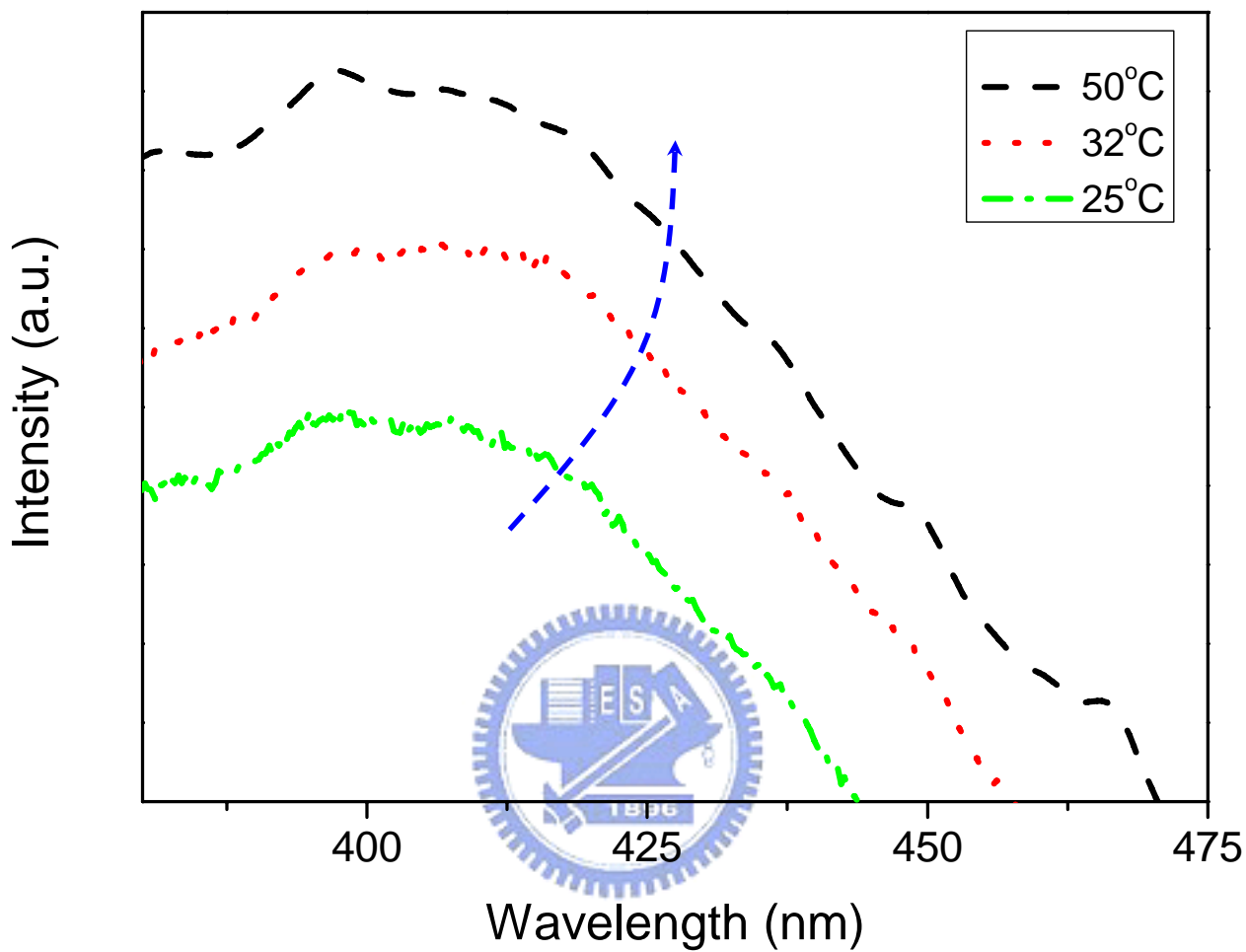


Figure 5-7. Normalized photoluminescence spectra of the 0.3-ZnS/PNIPAM hollow sphere at different temperature.

Chapter 7

Conclusions

We have employed the novelty of the preparation of the C₂₀-POSS and C₂₀-4VB containing intercalated agents. Syntheses of exfoliated nanocomposites via emulsion polymerization of styrene in the presence of 3 wt % clay containing the C₂₀, C₂₀-4VB, and C₂₀-POSS intercalated agents, were prepared respectively. XRD results show that d spacing increases from 1.28 nm to 3.95, 3.33, and 3.80 nm after intercalation. The C₂₀-4VB containing vinyl benzyl group results in more effective in promoting fully exfoliated structure in polystyrene matrix. All modified clay nanocomposites result in higher T_g and higher thermal degradation temperature than the virgin PS, especially for the C₂₀-POSS/clay nanocomposite resulting in 25 °C increase in the thermal degradation temperature. These well distributed clay platelets tend to retard the segmental movement of PS and result in reduced CTE. The incorporation of the 3 wt% clay leads to improvements in thermal stability, slight increase in glass transition temperature, and decrease in coefficient of thermal expansion.

The POSS-clay hybrids of polystyrene are prepared via emulsion polymerization using two organically modified clays, POSS-NH₂ and C₂₀-POSS, as intercalated agents. X-ray diffraction (XRD) results indicate that the clay is successfully intercalated by POSS-NH₂ and C₂₀-POSS. The random dispersion of these exfoliated

silicate layers in these nanocomposites are identified by XRD and TEM. These well dispersed clay platelets in PS matrix result in improved thermal properties in terms of thermal decomposition temperature (T_d) and glass transition temperature (T_g). In addition, the incorporation of these organoclay results in significant reduction in coefficient of thermal expansion of virgin PS.

A series of CPC-clay hybrids of polybenzoxazine (PP-a) have been prepared and their thermal properties and surface free energy have been characterized. The surface free energy of the CPC/clay/PP-a nanocomposites through a simple thermal treatment is significantly reduced. The lowest surface free energy obtained of the CPC/clay10%/polybenzoxazines (PP-a) is 12.6 mJ/m^2 , even lower than that of PTFE (22.0 mJ/m^2). In addition to the decrease the surface free energy of the nanocomposites and improve the thermal properties after the incorporation of 10 % organoically modified montmorillonite.

The novel inorganic/organic nano-spheres, (ZnS/PCL/PNIPAM), were successfully prepared by a simple free radical polymerization method. After locking the sphere structure by the cross-linking with the MBA, the core was degraded with Lipase PS, and the ZnS/PNIPAM hollow spheres can be obtained. The ZnS/PNIPAM hollow sphere possesses reversible thermo-sensitive properties and its hydrodynamic diameter ($\langle D_h \rangle$) is sensitive to the temperature stimuli response. Furthermore, slight

red-shift of maximum PL wavelengths was observed. The hollow spheres of the ZnS/PNIPAM have the potential applications in QDs-based biosensors and devices.



LIST OF PUBLICATIONS

(A) Journal

1. **Huei-Kuan Fu**, Huang, Chih-Feng, Jieh-Ming Huang, Feng-Chih Chang*
"Studies on thermal properties of PS nanocomposites for the effect of intercalated agent with side groups". Polymer, 2008, 49, 1305-1311.
2. **Huei-Kuan Fu**, Shiao-Wei Kuo, Ding-Ru Yei, Feng-Chih Chang* **"Properties Enhancement of PS Nanocomposites through the POSS Surfactants".**
Journal of Nanomaterials Volume 2008, Article ID 739613, 7 pages.
3. **Huei-Kuan Fu**, Chih-Feng Huang, Shiao-Wei Kuo, Han-Ching Lin, Ding-Ru Yei, Feng-Chih Chang* **"Effect of an Organically Modified Nanoclay on Low-Surface-Energy Materials of Polybenzoxazine"** *Macromol. Rapid Commun.* 2008, 29, 1216–1220.
4. **Huei-Kuan Fu**, Chih-Feng Huang, Shiao-Wei Kuo, Feng-Chih Chang* **"Preparation of the Stimuli-Responsive ZnS/PNIPAM Hollow Spheres"** polymer in press.

5. Ding-Ru Yei, Shiao-Wei Kuo, **Huei-Kuan Fu**, Feng-Chih Chang* "*Enhanced Thermal Properties of PS Nanocomposites formed from Montmorillonite Treated with a Surfactant/Cyclodextrin Inclusion Complex*". *Polymer* **2005**, 46, 741 – 750.
6. Ding-Ru Yei, **Huei-Kuan Fu**, Feng-Chih Chang, "*Polymer nanocomposites Part I Polystyrene/clay nanocomposites*" Woodhead Publishing, Chapter 5, **2005**.
7. Ding-Ru Yei, **Huei-Kuan Fu**, Wen-Yi Chen, Feng-Chih Chang* "*Synthesis of a novel benzoxazine monomer-intercalated montmorillonite and the curing kinetics of polybenzoxazine/clay hybrid nanocomposites*". *Journal of Polymer Science Part B: Polymer Physics*, **2006**, 44, 347-358.
8. Ding-Ru Yei, **Huei-Kuan Fu**, Yu-Hsin Chang, Shiao-Wei Kuo, Jieh-Ming Huang, Feng-Chih Chang* "*Thermal Properties of Polystyrene Nanocomposites Formed from Rigid Intercalation Agent-Treated Montmorillonite*". *Journal of Polymer Science: Part B: Polymer Physics*, **2007**, 45, 1781–1787.

(B) Conference

1. 傅懷廣、業定儒、郭紹偉、張豐志 “*Thermal Properties of Polystyrene Nanocomposites formed from Rigid Intercalated Agents-Treated Montmorillonite*” 第 30 屆高分子年會 (Oral).
2. Huei-Kuan Fu, Chih-Feng Huang, Shiao-Wei Kuo, Feng-Chih Chang* "*Effect of an Organically Modified Nanoclay on Low-Surface-Energy Materials of Polybenzoxazine*" The 42th IUPAC World Polymer Congress (MACRO 2008), Taipei (Post)
3. Huei-Kuan Fu, Chih-Feng Huang, Shiao-Wei Kuo, Feng-Chih Chang* "*Preparation of the Stimuli-Responsive ZnS/PNIPAM Hollow Spheres*" The 236th ACS National Meeting & Exposition, 2008 Philadelphia, PA, USA (Post).
4. Huei-Kuan Fu, Chih-Feng Huang, Shiao-Wei Kuo, Feng-Chih Chang* "*Preparation of the Stimuli-Responsive ZnS/PNIPAM Hollow Spheres*" The 16th Annual International Conference on Composites/Nanoengineering (ICCE - 16) Kunming China, July 2008 (Oral).



Introduction to Author

English name: Huai-Kuang Fu

Chinese name: 傅懷廣

Birthday: 1981, 10, 10

Address: 420 台中縣豐原市瑞興路 44 巷 9 號



Education:

- 2000.09~2004.06 **B.S.**, Department of Chemical Engineering and
Biotechnology & Institute of Chemical Engineering,
National Taipei University of Technology, Taipei, Taiwan.
- 2004.09~2006.02 **M.S.**, Institute of Applied Chemistry, National Chiao Tung
University, Hsinchu, Taiwan.
- 2006.03~2009.02 **Ph.D.**, Institute of Applied Chemistry, National Chiao Tung
University, Hsinchu, Taiwan.

